Reconciling Geodetic Strain and Seismicity Rate with the Frequency-Magnitude Relation of the Largest Earthquakes

Thesis by
Victoria L. Stevens

In Partial Fulfillment of the Requirements for the
degree of
Doctor of Philosophy

CALIFORNIA INSTITUTE OF TECHNOLOGY
Pasadena, California

2016
Defended May 18, 2016

Victoria L. Stevens
ORCID: 0000-0003-3174-9949

ACKNOWLEDGEMENTS

It is very hard to write these acknowledgements, as I do not want to leave anyone out. I would like to thank everyone in the Pit - Luca, Ted, Frank, Renata, Jenn, Sophie, Adam, Kirsten, Jason, Kristel, and my various office mates - Frank, the most longstanding, who will finish at the same time as me, and who always tells good jokes, and Ryan and Mortaza, as well as my former office mates. I would like to especially thank Luca, who has always been there for me and given me huge encouragement along the way, and my family, who have enjoyed holidaying on the West Coast, though perhaps have missed me whilst I have been away. My advisor Jean-Philippe, I would like to thank a lot, for being a great advisor, providing guidance, support and suggestions. I thank my housemates from second year - Steve, Krzysztof, Tristan, Vipul and Robb, and friends who were always keen for adventures - Tom, Becky, Belinda, Bailey, Thibault and all the others too numerous to mention. I would also like to thank members of my thesis committee for their helpful comments and for reading this manuscript.

ABSTRACT

The aim of this thesis is to study how moment buildup rate on faults can be reconciled with moment release rate. We concentrate first on the Himalaya region and go on to look at faults worldwide. We first justify the extrapolation of GPS data in the Himalayan region over the approximate timescale of an earthquake cycle. To do this we show that GPS strain rates correlate with seismicity rates, and that the principal directions of strain found from GPS data are similar to those from earthquake moment tensors, showing that GPS data has been consistent at the timescale of earthquake strain-rate build-up, roughly 100-1000 years.

We next use geodetic data to show that the Main Himalayan Thrust (MHT) is locked from the surface to roughly 100 km north along its entire length, with no creeping patches. We also find the long-term slip rate on the fault, and these values agree with values from geomorphic studies, showing that here the tectonic regime has been stable with time, and most of the deformation is elastic. However, we also find a correspondence between the pattern of uplift rate predicted from the model and the topography, suggesting that a small amount of permanent deformation (<10%) may occur, and again suggesting that the pattern of coupling has been stable with time.

We find the moment build-up rate on the MHT to be $15.1 \pm 1.0 \times 10^{19}$ Nm/yr and compare this rate with the rate of moment release estimated from large earthquakes that have occurred on this fault in the past 1000 years. We use the conservation of moment principle to model the most likely maximum magnitude earthquake that needs to occur to balance the moment budget, and find that we need an earthquake of magnitude 9 or more with a recurrence time of roughly 800 years.

We extend this analysis to faults with no GPS data, and no long record of large earthquakes, by developing a method to find the expected maximum magnitude earthquake on faults assuming conservation of moment, and that the earthquakes follow the Gutenberg-Richter law. Our results compare well with historical catalogs where they are available.

PUBLISHED CONTENT

Chapter 2 is published as Stevens, V. L. and J. P. Avouac (2015). “Interseismic coupling on the main Himalayan thrust". In: *Geophysical Research Letters* 42.14 2015GL064845, pp. 5828-5837. DOI: 10.1002/2015GL064845.
URL: http://dx/doi/org/10.1002/2015GL064845.

Chapter 3 is published as Stevens, V. L. and J. P. Avouac (2016). “Millenary M_w >9.0 earthquakes required by geodetic strain in the Himalaya". In: *Geophysical Research Letters* 43.3 2015GL067336, pp. 1118-1123. DOI: 10.1002/2015GL067336.
URL: http://dx.doi.org/10.1002/2015GL067336.

TABLE OF CONTENTS

Acknowledgements . . . iii
Abstract . . . iv
Table of Contents . . . vi
List of Illustrations . . . vii
List of Tables . . . xviii
Introduction . . . 1
Chapter I: Consistent Seismicity and Strain Rates in the India-Asia Collision Zone . . . 12
Abstract . . . 13
1.1 Introduction . . . 14
1.2 Geodetic strain rates . . . 15
1.3 Comparison with seismicity rate . . . 17
1.4 Comparison with seismic moment tensors . . . 19
1.5 Discussion-Conclusion . . . 21
Chapter II: Interseismic Coupling on the Main Himalayan Thrust . . . 25
Abstract . . . 26
2.1 Introduction . . . 27
2.2 Data . . . 28
2.3 Methods . . . 29
2.4 Results and Discussion . . . 32
2.5 Conclusions . . . 39
Chapter III: Millenary $M_w > 9.0$ earthquakes required by geodetic strain in the Himalaya . . . 46
Abstract . . . 47
3.1 Introduction . . . 48
3.2 Method and Data . . . 50
3.3 Results and Discussion . . . 53
3.4 Conclusion . . . 55
Chapter IV: Determination of the maximum plausible earthquake M_{max} from background seismicity and the moment budget balance . . . 66
Abstract . . . 67
4.1 Introduction . . . 68
4.2 Model . . . 73
4.3 Results . . . 78
4.4 Discussion . . . 89
4.5 Conclusion . . . 91

LIST OF ILLUSTRATIONS

Number *Page*

0.1 GPS velocities in the region taken from the literature, in the fixed-Eurasian reference frame. 2

0.2 Comparison of GPS-derived strain rate map from 2012 (left), and from 2016 (right). 3

0.3 Active faults in the area from Styron, Taylor, and Okoronkwo (2010), with faults mentioned in the text highlighted in red. Faint blue lines show the country outlines. 3

0.4 Comparison of directions of principal horizontal strain rates. Red lines show direction of maximum compression and blue arrows show direction of maximum extension. a) Moment tensor solutions. b) GPS strain rate map. c) Probability density function (PDF) of normalized misfit of the Frobenius norm between the moment tensor and GPS strain rates, which includes the 3D component and the relative magnitudes. d) Frobenius norm distribution. 5

0.5 Coupling model and fit to the horizontal GPS data. The interseismic coupling is shown as shades of red. A coupling value of 1 means the area is fully locked, while a value of 0 means fully creeping. The green and black arrows and ellipses show the continuous and campaign GPS velocities (in the fixed-Indian reference frame of Ader et al. (2012)), with their error bars, respectively. The blue arrows are the modeled velocities, which fit with the coupling shown. The large red arrows show the long-term velocities in each region. The dashed black lines show the boundaries of the regions, within which the long-term velocity for that region is calculated, as shown by the large red arrows. The solid black lines, labeled at 10 km intervals, show the depth contours of the fault plane. 6

0.6 Interseismic coupling and moment build-up on the Main Himalayan Thrust. The pattern of coupling (Stevens and Avouac, 2015) is shown in red, overlain by the rough locations of earthquakes M_w7.5-8 for the past 200 years and ≥8 for the past 500 years (Kumar et al., 2010; Galetzka et al., 2015), which are used in calculating the rate of seismic moment release (light blue bars). The approximate extent of surface ruptures of two potential major earthquakes, dated to ~1400AD and ~1100AD from paleoseismic studies, are also shown. The probability distribution function (pdf) in the inset shows the seismic moment build-up calculated from the coupling model, and the yellow bars show its distribution along the arc. 7

0.7 a) Blue line shows the frequency of the largest earthquake that would have to occur if it were to be M_{max}. Red lines show theoretical earthquake catalogs which follow the GR law, and intersect the moment line at 7, 8, and 9. b) Here the blue line is the same as in a, but now we have real data from the MHT. Green and red triangles show instrumental data, while pink dots shown historical and paleoseismic data with error bars. c) Result of combining the different earthquake catalogs and rates of different large earthquakes. This shows the probable size of the M_{max} needed to balance the seismic moment build-up. The red curve shows the final result, showing that we need roughly a magnitude 9 earthquake to balance the budget. d) Zoom in of b. Colored contour lines show the 2-D pdf of the magnitude and frequency of the maximum earthquake. Grey shaded cumulative density functions along the x and y-axes represent, respectively, the marginal cumulative probability of the largest earthquake exceeding a given magnitude, and the cumulative marginal probability of its frequency being lower than a given value. 8

0.8 GR plot for a) the San Andreas Fault and b) the Boconó fault. The dark blue lines show the moment build-up line. The light blue lines show the instrumental data for the past 20 years. The green straight lines show the modeled complete earthquake catalog. The green triangles show the historic data. The colored ovals indicate the probability that the maximum magnitude earthquake would fall within them. 10

1.1 a) GPS data used in the strain rate calculation. Black lines show faults from Styron, Taylor, and Okoronkwo (2010) and red lines highlight faults mentioned in the text. b) Second invariant of the strain rate tensor for region of interest calculated from GPS data. For the method and GPS data references see the Methods section. . . 16

1.2 a) Gutenberg-Richter plot of declustered catalog within areas of different strain, normalized per area. See Figure S2 for areas of different strain rate. b) Comparison of normalized earthquake rate and strain rate from GPS. Colored dots correspond to discrete regions of different strain rate levels. Grey lines show 100,000 realizations of randomized distributions of earthquakes. These show greater dispersion as strain rate increases because the areas in which these strain rate levels occur decreases. The solid black line shows the linear best fit, and the two dashed lines show the 2-sigma errors on the line, assuming that earthquakes are a Poisson process. c) Strain rate versus normalized cumulative area (blue) and normalized cumulative earthquake count (red). 18

1.3 Comparison of directions of principal horizontal strains. Red lines show direction of maximum compression and blue arrows show direction of maximum extension. a) Moment tensor solutions. b) GPS strain rate map. c) Misfit of the Frobenius norm between the moment tensor and GPS strain rates, which includes the 3D component and the relative magnitudes. d) Frobenius norm distribution. 20

1.S1 Gutenberg-Richter plot showing the entire declustered catalog as blue circles. The b value calculated from the maximum likelihood method (Aki, 1965) is 0.94±0.01, and the mean is shown as the red line. . . . 23

1.S2 Plot showing boundaries of areas of different strain rate from GPS data, and the locations of earthquakes within them, both color-coded by different strain rate. 24

1.S3 Probability density functions (PDFs) of Frobenius norm misfit of strain rate tensor to GPS strain rate tensor. a) Modeled strain that is perfect GPS strain plus a standard deviation of 0.13±0.075. b) Real data from earthquake strain. c) Modeled completely random strain. The median misfit is 0.16, 0.31, and 0.51 respectively. 24

2.1 Coupling model and fit to the horizontal GPS data. The interseismic coupling is shown as shades of red. A coupling value of 1 means the area is fully locked, while a value of 0 means fully creeping. The green and black arrows and ellipses show the continuous and campaign GPS velocities (in the fixed-Indian reference frame of Ader et al. (2012)), with their error bars, respectively. The blue arrows are the modeled velocities, which fit with the coupling shown. The large red arrows show the long-term velocities in each region. The dashed black lines show the separation of the regions, within which the long-term velocity for that region is calculated, as shown by the large red arrows. The solid black lines, labeled at 10 km intervals, show the depth contours of the fault plane. The labels INDIA, SHILLONG and ASSAM refer to three blocks which are assumed to be rigid. The residuals to the horizontal GPS, the InSAR and leveling data are shown in Figure 2.S5. Electronic data of the coupling pattern are included in an SI file. 33

2.2 (a) The same coupling model as in Figure 2.1, with the location of seismicity used to regulate the Laplacian smoothing. Seismicity within Nepal is from an NSC catalog (Ader et al., 2012; Rajaure et al., 2013) seismicity between roughly 77°E and 81°E is from Mahesh et al. (2013) and the remainder is from NEIC. The modeled fault is outlined in black. (b) Shear stress accumulation rate on the fault plane, calculated from the coupling pattern, overlain by the same microseismicity as in Figure 2.2a, here shown as white dots. Electronic data of the stress rate pattern are included in an SI file. (c) Probability distribution function of the total moment build-up rate per year. Dashed lines show one standard deviation. 34

2.3 Shortening rate across the Himalayas from the results of this study (red) and geomorphic studies (blue). Geomorphic data from west to east are from (Thakur et al., 2014; Wesnousky et al., 1999; Parkash et al., 2011; Mugnier et al., 2003; Lavé and Avouac, 2000; Bollinger et al., 2014; Berthet et al., 2014; Burgess et al., 2012). Inset shows the probability that the average modeled long-term GPS velocities exceed the average velocities from geomorphic studies by different amounts. 36

2.4 Focal mechanisms from the CMT catalog. Blue arrows show the direction of the slip vectors i.e. the movement of the hanging wall. Red arrows show the direction of the long-term velocity vectors calculated in this study (in the fixed-Indian reference frame of Ader et al. (2012)). The dashed black lines show the boundaries between the different regions for which long-term velocities were calculated for. The thick black line shows the surface trace of the MHT and the grey lines show country borders. 37

2.5 Comparison of topography with uplift rate. (a) Topography. Black lines show location of topographic and uplift rate profiles shown in Figure 2.S7. (b) Uplift rates calculated from the coupling pattern. (c) Correlation of topography with uplift rate, R value 0.78. Each dot represents an uplift rate from each patch used to model the fault (roughly 15x17 km) and the topography averaged over the same region. 38

2.S1 Location of data used in the inversion. Arrows show velocities relative to India (as defined by Ader et al. (2012)) determined from continuous (green) and campaign (black) GPS data. Ellipses show the uncertainties at the 67% confidence level. The blue circles are InSAR data. The magenta circles are leveling data. The thick red line is the simplified geometry of the MHT used in the model. Country borders are marked in grey. 42

2.S2 The model setup. The red line shows the simplified surface trace of the fault, and the grid shows the discretization used in this model. The dashed black lines are the boundaries between different regions of uniform long term slip rate. The blue lines show the edges of the two blocks for which rotation poles are found. The red dashed lines show the rough location of major grabens. KC = Kaurik Changdu rift (Kundu et al., 2014). TH = Thakkola graben (Colchen, 1999). DS = Dingjie-Sehnza fault zone (Gan et al., 2007). YG = Yadong-Gulu rift (Gan et al., 2007). Thinner red/brown lines show faults from Styron, Taylor, and Okoronkwo (2010). 43

2.S3 Same as Figure 2.2, except with the poles of Vernant et al. (2014) imposed and not solved for. 43

2.S4 Same as Figure 2.1a, except with uniform weighting of the Laplacian. The coupling model is thus not regulated by the seismicity. . . 44

2.S5 Residuals to the GPS data, with uncertainy ellipses. Campaign measurements are in red, and continuous measurements in green. The inset shows the residuals of the InSAR and leveling data. 44

2.S6 Resolution on each patch of the fault. The resolution here is the characteristic size of the smallest inhomogeneities of coupling which could in principle be resolved, given the spatial distribution and uncertainties of the measurements. The figure is saturated at a resolution of 80 km, as above this value we assume there is no resolution on the corresponding patch, and so slip on this patch is just determined by slip on the neighbouring patches. See Ader et al. (2012) for details of the calculation. The location of data points used to find the resolution are also shown. 45

2.S7 Smoothed elevation (red) compared with modelled uplift rates (blue) at different longitudes. Profile locations are shown in Figure 2.5 of the main text. 45

3.1 Interseismic coupling and moment build-up on the Main Himalayan Thrust. a) The pattern of coupling (Stevens and Avouac, 2015) is shown in red, overlain by the rough locations of earthquakes M_w7.5-8 for the past 200 years and ≥ 8 for the past 500 years (Kumar et al., 2010; Galetzka et al., 2015), which are used in calculating the rate of seismic moment release (light blue bars). The approximate extent of surface ruptures of two potential major earthquakes, dated to ~1400AD and ~1100AD from paleoseismic studies, are also shown. The probability distribution function (pdf) in the inset shows the seismic moment build-up calculated from the coupling model, and the yellow bars show its distribution along the strike of the arc. b) Same coupling pattern, now with the surface trace of the Main Himalayan-Thrust (Styron, Taylor, and Okoronkwo, 2010) in dark blue and the 3500 m elevation contour line in light blue. The 3500 m contour seems to mark the downdip extent of the locked fault zone. The MHT appears locked from the surface, where is emerges along the front of the sub-Himalaya, following the trace of the Main Himalayan Thrust to beneath the front of the high Himalaya. Red arrows show convergence across the range in mm/yr. Black dots show seismicity from the NSC and NEIC catalogs (Ader et al., 2012; Stevens and Avouac, 2015). The grey bars show the distribution of the number of earthquakes above 4.9 (the magnitude of completeness) of the declustered NEIC catalog (see Supplementary Information for details). 49

3.2 Comparison of interseismic moment build-up and seismic moment released by known earthquakes. a) Plot showing moment release rates for different sized earthquakes. Blue line shows the moment build-up rate calculated from the coupling pattern - the width of the line shows the errors. The curves showing the moment released by earthquakes are cumulative (all earthquake with magnitude less than the abscissa value are added). The catalog of historical and palesoseismic events is listed in Table 3.S1. The plot assumes one M_w9 event in the past 1000 years. With these assumptions, seismicity does not balance locking of the MHT in the interseismic period and to do so it would need to extend up to a magnitude more than M_w9. b) Gutenberg-Richter plot with the same assumptions. The blue line shows the magnitude-recurrence time relationship of earthquakes that would take up the seismic moment. The black dashed lines show (top to bottom) where the seismicity should lie given an earthquake with maximum magnitude 8, 9, or 10 respectively, assuming it follows the GR law with a b-value of 1.1. The pink markers show the estimated long-term average seismicity rates, and associated uncertainties (error bars show one sigma errors), by grouping magnitudes into bins of 0.5-magnitude unit range (Table 3.S2). This allows for a better estimation of uncertainties. c) Gutenberg-Richter plot of historical earthquakes (Table 3.S1) compared with the frequency-magnitude of the largest event needed to balance the slip budget. 54

3.3 Probability distribution functions of the frequency-magnitude of the largest earthquake need to balance the slip budget. a) Method 1. Colored contour lines show the 2-D pdf of the magnitude and frequency of the maximum earthquake. Grey shaded cumulative density functions along the x and y-axes represent, respectively, the marginal cumulative probability of the largest earthquake exceeding a given magnitude, and the cumulative marginal probability of its frequency being lower than a given value. Pink markers show the binned magnitudes as in Figure 3.2B. b) Method 2. As in A, the shaded curves show the probability an earthquake of that magnitude, or recurrence time, could occur and take up the needed seismic-moment. The probability drops after each of the magnitudes of the large earthquakes because above that magnitude we have seen fewer earthquakes and they are short of balancing interseismic moment deficit. The drop after magnitude 9 is smaller because the recurrence time needed for a magnitude 9 to close the slip budget is closer to the observation period, 1000 years, so it is much more likely that we could have missed an earthquake with this recurrence time. Blue markers showed the unbinned magnitudes, as in Figure 3.2C. 55

3.S1 All data sets used separately to predict the maximum moment. . . . 62

3.S2 Data sets combined. Grey line shows the case with zero afterslip. . . 62

3.S3 The red line shows 50% afterslip and this is used in the main text. The green line assumes zero afterslip. The purple line shows the probabilities if we assume the largest earthquake releases all the moment, with 50% afterslip. The blue line shows 50% afterslip and a 50% decrease in moment build-up due to distributed deformation. . . 64

3.S4 Same as Figure 3.3 in the main text, but now assuming anelastic shortening of the Himalayan wedge takes up all the shortening across the Himalaya. The underlying MHT is still assumed seismic but long-term slip rate tapers linearly to zero at the surface. The rate of seismic moment build-up is halved. 65

3.S5 Seismic moment released from major earthquakes along the Himlayan Front compared to moment accumulation since 1000 AD. Blue lines show moment build-up calculated from the coupling model of Stevens and Avouac (2015). The solid line shows the mean, the two dashed lines show the one-sigma errors. The dotted line shows the mean reduced by 50% - used in most of the calculations. The black lines show moment release. The solid line shows the preferred model, whilst the dashed lines show the highest and lowest reasonable magnitudes for past earthquakes. 65

4.1 Demonstrating steps of the method. Straight blue line is moment build-up rate line, which shows the frequency of the maximum magnitude earthquake that would need to occur to take up all the moment build-up. The lower wiggly blue line is the instrumental catalog, here from the San Andreas Fault. The black dashed lines are demonstrative to show the GR law with b of 1, so where the earthquake catalog should lie to intersect maximum magnitudes of 7, 8, and 9. a) The original setup. b) Orange lines show the first round of adding on missing earthquakes from magnitude 9 down to the cutoff magnitude, here 4.4. c) Orange lines are the same as for b, but now yellow and green lines show two more rounds of adding on missing earthquakes. The number needed to be added on decreases with each round, which is why the lines get closer and closer together. d) Same as c but now showing a trial maximum magnitude of 8.1, which is the maximum magnitude that is predicted. 79

4.2 Comparing instrumental data of the light blue line with 100 realizations of 20 years of data with the same statistics as the mainshocks in the final average catalog test shown in gray. These different realizations have varying maximum sized earthquakes, from 5.3 to 8.2 in the cases shown here. 80

4.3 Results of the model. Here the yellow, orange, and red lines show the probability of being within the ovals, taking into account the uncertainties on the b-value, the moment build-up rate and the value of the largest aftershock. Here the straight green lines show the final averaged modeled catalog. Light blue lines show the instrumental catalog and the dark blue line is the moment conservation line. The left-hand panels show the fault in red with earthquakes as black dots, and earthquakes selected to use in the model as blue dots. a) The San Andreas Fault. Here green triangles show the historic data. b) The North Anatolian Fault. Green triangles show the historic data averaged over the past 100 years, whereas blue triangles are averaged over the past 2300 years. c) The Main Himalayan Thrust with pink dots and error bars showing the historical data. d) The Japan Trench, with green triangles showing the historic data. 82

4.4 Results of the model for areas without long historic data catalogs. a) Boconó Fault. c) Altyn Tagh Fault. b) Dead Sea Transform. d) Kunlun Fault. 87

4.S1 Comparing the aftershock model (straight lines) with observations . . 93

LIST OF TABLES

Number *Page*

2.S1 Long term slip rates from geomorphic studies and modelled here . . . 42

2.S2 Rotation Poles with respect to India for the Sikkim/Shillong and Bhutan/Assam Blocks of this study, and the Shillong and Assam Blocks in the study of Vernant et al. (2014). 42

3.S1 Earthquakes above magnitude 7.5 for the past 1000 years from paleoseismic, historical and instrumental catalogs. 59

3.S2 Proposed rate of large earthquakes estimated based on the data of Table 3.S1. Range of number of earthquakes at the 1-σ confidence level. For magnitude 7.5, we use the past 200 years of data, and scale up to 1000 years. 59

Reconciling Geodetic Strain and Seismicity Rate with the Frequency-Magnitude Relation of the Largest Earthquakes

INTRODUCTION

Understanding the frequency-magnitude relation of large earthquakes is important for seismic hazard mitigation. We would like to know how often different sized earthquakes might occur. It is useful to know the largest sized earthquake that could ever occur, but also the probabilities of different sized earthquakes happening in particular time frames. These probabilities are often used by engineers to design buildings that have a very small chance of falling down during their expected lifetime. If it is unclear what size the largest earthquake would be, it is hard to prepare for. Before the large Japanese earthquake of 2011, it was thought that earthquakes as large as $M_w 9$ would not occur in that region. This meant that when the $M_w 9$ earthquake did happen, the size of the resulting tsunami was much larger than had been planned for, and this miscalculation led to enormous damage. In many developing countries the hazard is less well understood, and on top of that it is hard to communicate the probabilities of earthquake occurrence to non-scientists, especially in places where there has not been a large earthquake in a long time, and where they have many more obvious problems to concentrate on. It is also hard to prepare for earthquakes when the faults are unknown. One option would be to assume that there could be very large earthquakes anywhere, but this would be a waste of resources.

During my PhD I moved forward on some of these issues: I developed a model to find the maximum expected earthquake in the Himalayan region and its recurrence time, and then extended this model to large faults across the world.

The Himalayan Region has a high seismic risk, and an increasing population density. We now have 4094 GPS[1] measurements in the region (see Figure 0.1) and this number is continuously increasing. I used the GPS data to create a strain rate map of the region (following the method of Tape et al. (2009)). The difference between

[1] Global Positioning System

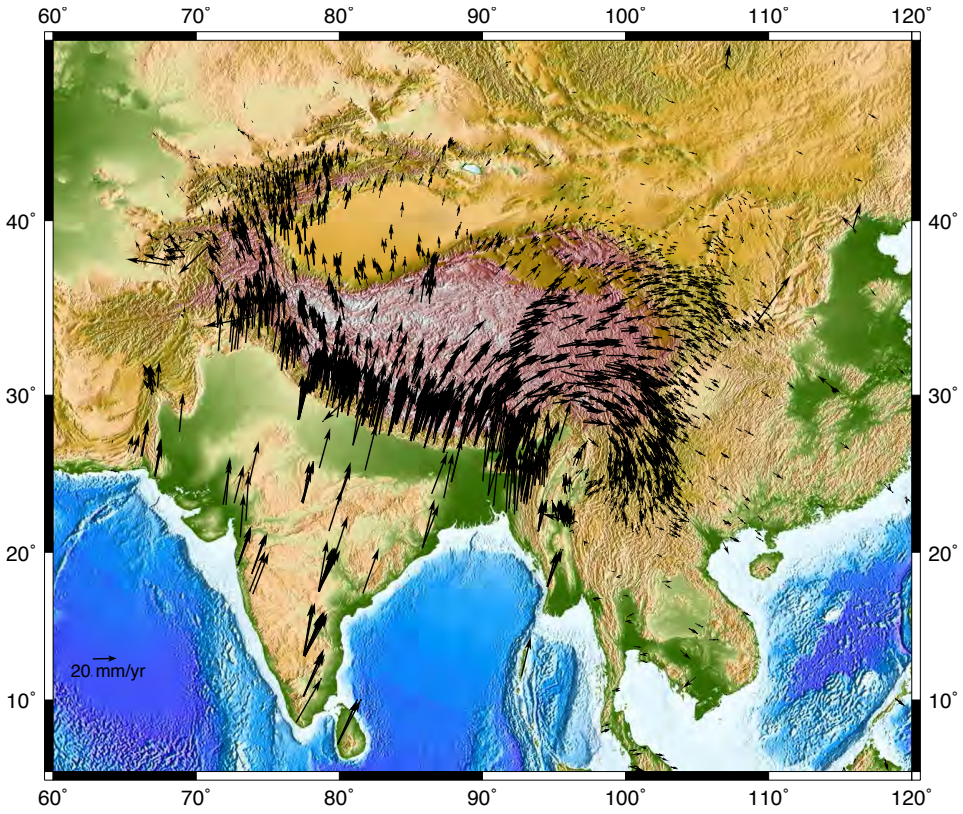

Figure 0.1: GPS velocities in the region taken from the literature, in the fixed-Eurasian reference frame.

a strain rate map of the region I made in my first year (2012), and one I made in my final year (2016) can be seen in Figure 0.2. The difference is due to the 1436 GPS measurements that were published in the intervening period. From this map of strain-rate, it can be seen that the Main Himalayan Thrust, or MHT, (see Figure 0.3 for a map of fault names and locations) is the most obvious feature — the area where the strain-rate is the highest over the largest region. The fault is absorbing about half of the regional convergence rate, so slip rates across it are around 20 mm/yr, which is greater than any other fault in the region. I concentrated first on finding the seismic hazard associated with this fault, the MHT.

GPS data are critical in finding the rate of strain buildup on the fault, but GPS has been recording ground motion of only the most recent 20 years or less. To find the seismic hazard and to be able to compare with historical records of earthquakes, we need to know if the GPS rates are constant through time, and so representative of the past few thousand years, or if they are variable and so biased towards present values.

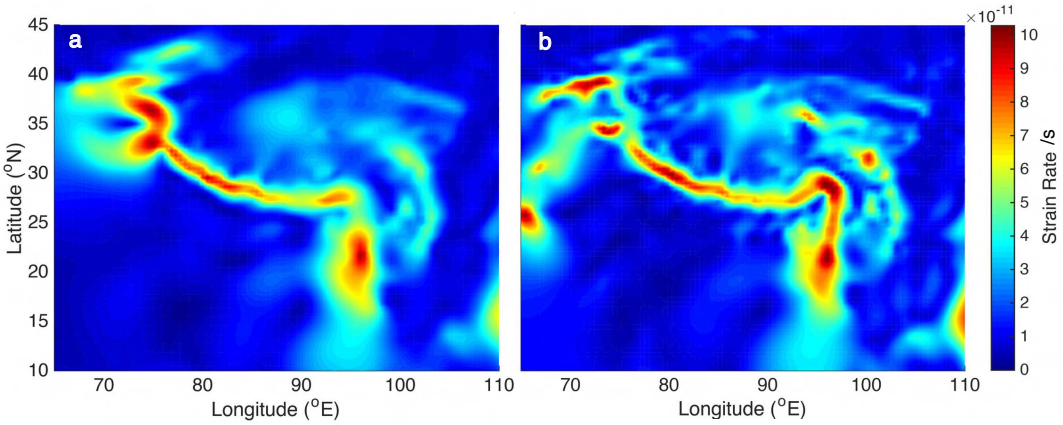

Figure 0.2: Comparison of GPS-derived strain rate map from 2012 (left), and from 2016 (right).

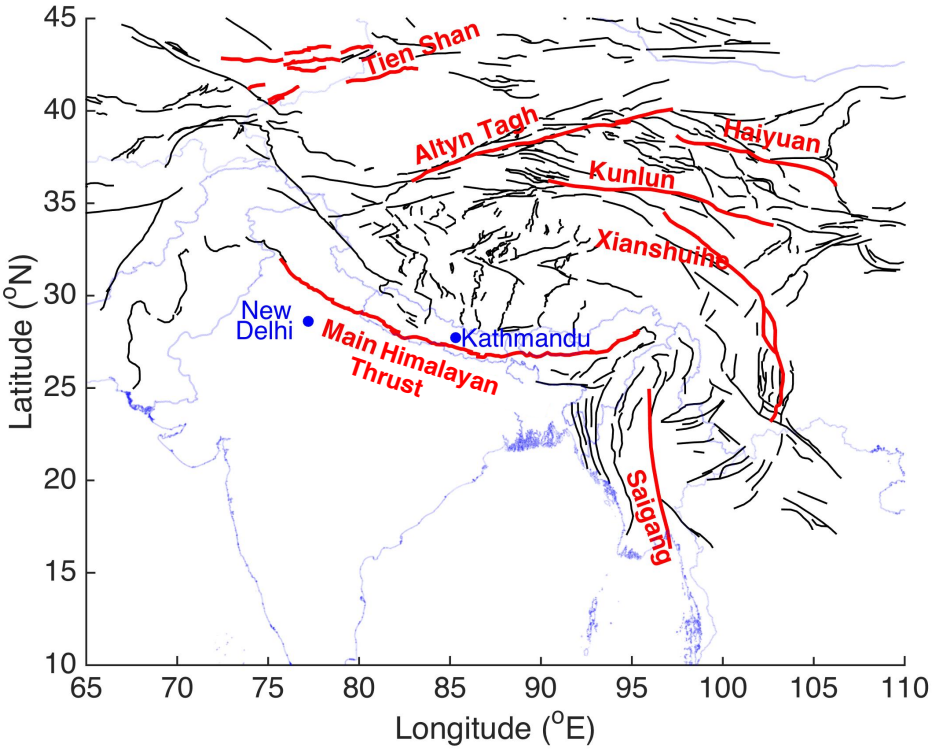

Figure 0.3: Active faults in the area from Styron, Taylor, and Okoronkwo (2010), with faults mentioned in the text highlighted in red. Faint blue lines show the country outlines.

To test this we compared GPS with earthquake strain data, since earthquakes release strain that has built up on a time period much longer than GPS, over hundreds and thousands of years. We find that these two pieces of data covering different timescales give similar results, so we can assume the GPS has been constant through time, as discussed more in Chapter 1. For example, Figure 0.4 shows a comparison of principal horizontal strain rate directions[2] calculated from GPS and earthquakes. We use the Frobenius norm (the square root of the sum of the squared differences of each element in the strain rate tensor) to quantitatively compare the geodetic strain rate and moment tensors:

$$||D||_F = \sqrt{\sum_{i=1}^{m}\sum_{j=1}^{n}|a_{ij} - b_{ij}|^2} \tag{1}$$

where $||D||_F$ is the Frobenius norm of the difference between the two matrices with components a_{ij} and b_{ij}. A histogram and map view of the Frobenius norm differences are shown in Figure 0.4 c and d.

After deciding that the MHT was the most important seismic hazard in the region, and knowing that we can extrapolate GPS back in the past, I used the GPS to find the pattern of coupling on the fault, the topic of Chapter 2. Where the fault is fully coupled, it is locked, so strain is accumulating here. Where the fault is not coupled, it is creeping, so there is some continuous movement and lower strain accumulation, and earthquakes are probably less likely to occur in these areas. As well as GPS we use InSAR data[3], leveling data,[4] and microseismicity[5] and inverted these data to find the coupling pattern, which also tells us the moment build-up rate, or how fast energy is building up, which has to be released.

The results of the coupling inversion can be seen in Figure 0.5, along with the calculated long-term velocities along the fault. The coupling pattern here is rather different to most subduction zones, where there are locked patches surrounded by creeping patches (e.g. Liu et al. (2010), Chlieh et al. (2011), Métois, Socquet, and Vigny (2012), and Schmalzle, McCaffrey, and Creager (2014)). Here there seem to be no creeping patches within roughly 100 km of the surface trace of the fault.

[2]Principal directions are the directions of maximum and minimum strain-rate
[3]Interferometric Synthetic Aperture Radar data
[4]Leveling data measures how much the earth's surface has gone up or down
[5]Microseismicity is small earthquakes

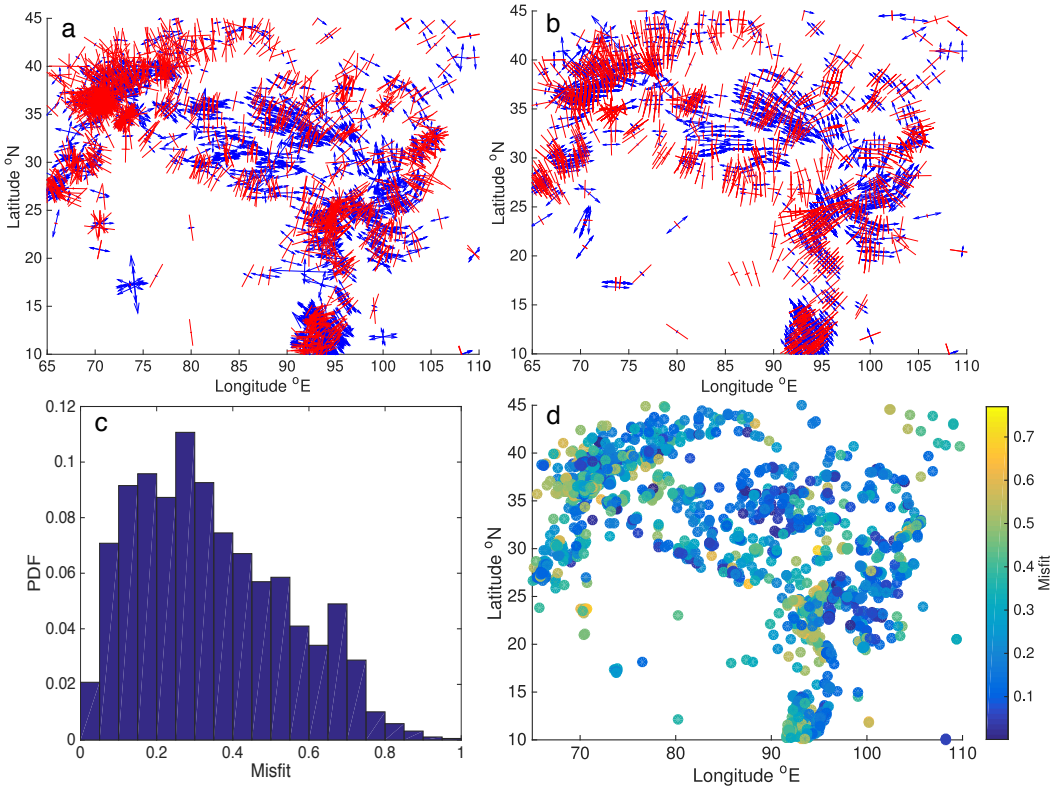

Figure 0.4: Comparison of directions of principal horizontal strain rates. Red lines show direction of maximum compression and blue arrows show direction of maximum extension. a) Moment tensor solutions. b) GPS strain rate map. c) Probability density function (PDF) of normalized misfit of the Frobenius norm between the moment tensor and GPS strain rates, which includes the 3D component and the relative magnitudes. d) Frobenius norm distribution.

Now that we have the coupling pattern we can find the moment buildup rate, and compare this with moment release in earthquakes from the recent and historic records. Almost everywhere along the Himalayan arc, the strain buildup exceeds the estimated strain released by earthquakes during the past 500 years (Figure 0.6). To get the moment back in balance, larger or more frequent large earthquakes than known from the past 500 years are thus needed.

To quantify this further, as shown in Chapter 3, we compare the frequency-magnitude relation of large earthquakes from the past, either historical or paleoseismic records. From the moment build-up rate we found, we can find the largest earthquake that would balance this, given assumptions about the magnitude-frequency distribution. One such assumption is that the earthquake magnitude-frequency distribution fol-

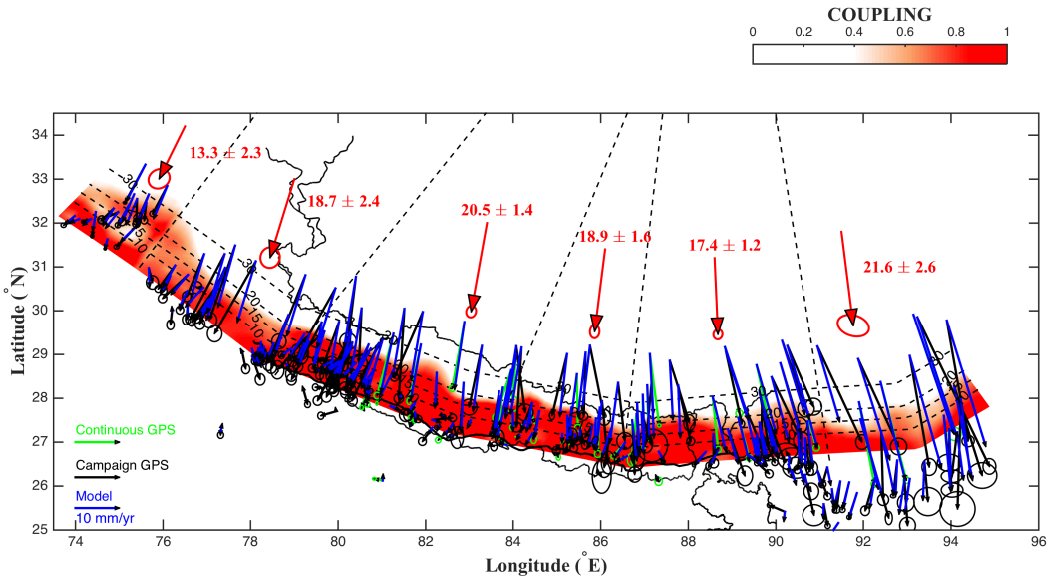

Figure 0.5: Coupling model and fit to the horizontal GPS data. The interseismic coupling is shown as shades of red. A coupling value of 1 means the area is fully locked, while a value of 0 means fully creeping. The green and black arrows and ellipses show the continuous and campaign GPS velocities (in the fixed-Indian reference frame of Ader et al. (2012)), with their error bars, respectively. The blue arrows are the modeled velocities, which fit with the coupling shown. The large red arrows show the long-term velocities in each region. The dashed black lines show the boundaries of the regions, within which the long-term velocity for that region is calculated, as shown by the large red arrows. The solid black lines, labeled at 10 km intervals, show the depth contours of the fault plane.

lows the Gutenberg-Richter (GR) law (Gutenberg and Richter, 1944):

$$log(N(M > M_w)) = a - bM_w \tag{2}$$

where N(M>M_w) is the number of earthquakes above M_w, a is the y-axis intercept, and can be thought of as the productivity, and b is the slope of the line, which often has a value close to 1 (Bird and Kagan, 2004; Godano, Lippiello, and Arcangelis, 2014).

The results of the model with the GR assumption are shown in Figure 0.7. We see that we have to have a very large earthquake, around magnitude 9 or above. This is bigger than any recent earthquake, but there is evidence from paleoseismology that earthquakes of a similar size may have happened more than 500 years ago (Kumar et al., 2006; Kumar et al., 2010).

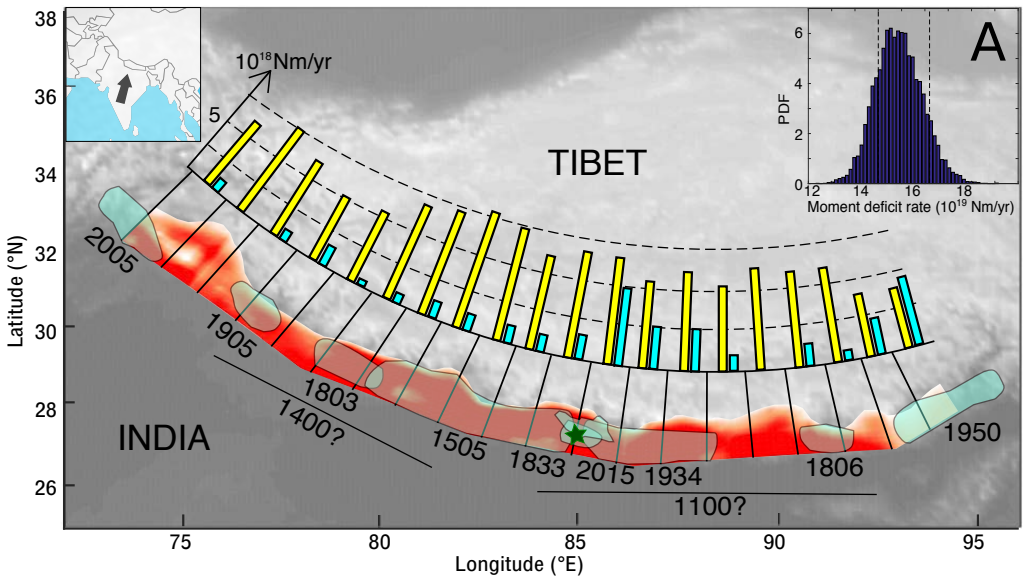

Figure 0.6: Interseismic coupling and moment build-up on the Main Himalayan Thrust. The pattern of coupling (Stevens and Avouac, 2015) is shown in red, overlain by the rough locations of earthquakes M_w7.5-8 for the past 200 years and ≥8 for the past 500 years (Kumar et al., 2010; Galetzka et al., 2015), which are used in calculating the rate of seismic moment release (light blue bars). The approximate extent of surface ruptures of two potential major earthquakes, dated to ~1400AD and ~1100AD from paleoseismic studies, are also shown. The probability distribution function (pdf) in the inset shows the seismic moment build-up calculated from the coupling model, and the yellow bars show its distribution along the arc.

The method used to find the largest possible earthquake, or M_{max}, on the Main Himalayan Thrust cannot be applied to most faults, as a dense GPS network and a catalog of historical earthquakes is needed, which most faults do not have. Historical earthquakes are those found from written records of shaking and building destruction, before the instrumental record began. The regional extent and intensity of shaking is used to calculate a rough magnitude. The historical record for the Himalayan region goes back around 500 years, and only includes earthquakes above magnitude 6.5, as smaller earthquakes do not cause as much shaking or damage, so fewer written reports of shaking can be found. Other large faults in the Tibetan region, such as the Altyn Tagh and the Kunlun, are slipping at half the rate of the Main Himalayan Thrust, which is still significant, but much less is known about them. The Kunlun fault had a large earthquake recently, M_w7.8, but the Altyn Tagh has had no large earthquake in living memory or in historical records. There are however paleoseismic observations and a large scarp, showing that the Altyn Tagh is capable of producing large earthquakes. I study this in Chapter 4.

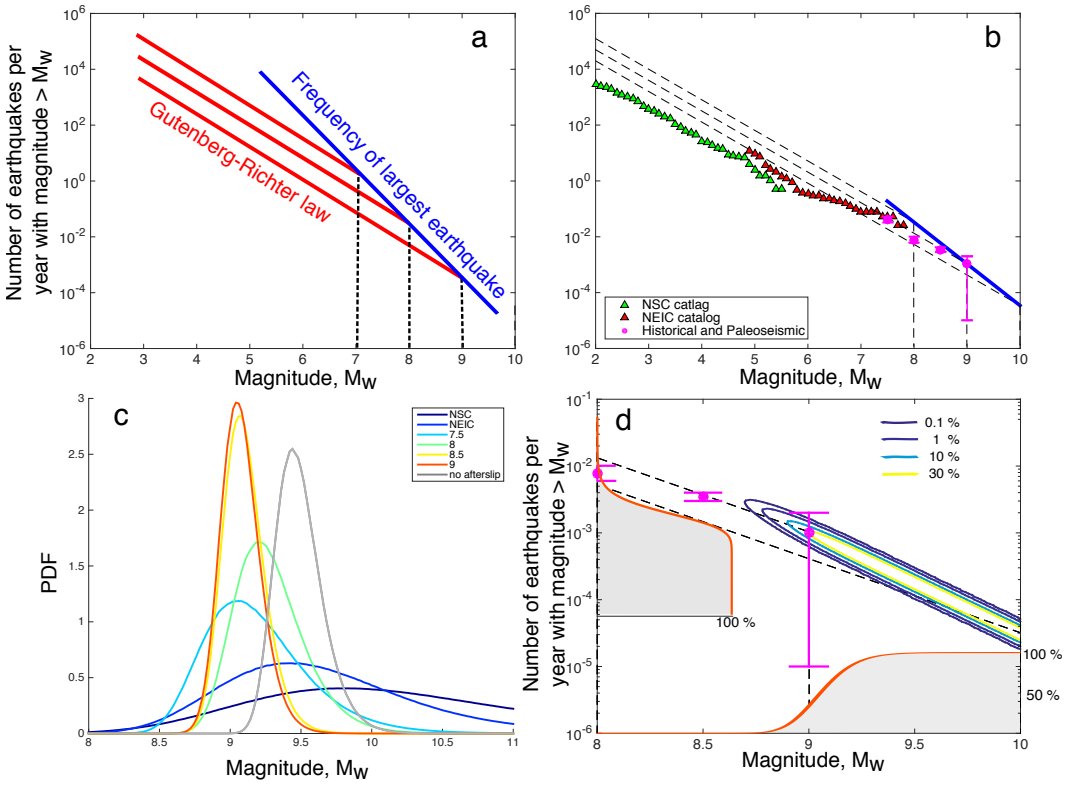

Figure 0.7: a) Blue line shows the frequency of the largest earthquake that would have to occur if it were to be M_{max}. Red lines show theoretical earthquake catalogs which follow the GR law, and intersect the moment line at 7, 8, and 9. b) Here the blue line is the same as in a, but now we have real data from the MHT. Green and red triangles show instrumental data, while pink dots shown historical and paleoseismic data with error bars. c) Result of combining the different earthquake catalogs and rates of different large earthquakes. This shows the probable size of the M_{max} needed to balance the seismic moment build-up. The red curve shows the final result, showing that we need roughly a magnitude 9 earthquake to balance the budget. d) Zoom in of b. Colored contour lines show the 2-D pdf of the magnitude and frequency of the maximum earthquake. Grey shaded cumulative density functions along the x and y-axes represent, respectively, the marginal cumulative probability of the largest earthquake exceeding a given magnitude, and the cumulative marginal probability of its frequency being lower than a given value.

To find the moment build-up, instead of using the GPS and coupling pattern, we used the relation

$$\dot{M}_\circ = \mu \cdot A \cdot s \cdot f_s, \tag{3}$$

where $\dot{M}_\circ$ is the moment build-up rate in Nm/s, μ is the rigidity in N/m^2, A is the fault plane area in m^2, s is the slip rate in m/s and f_s is the fraction released seismically.

Previously when the instrumental data (which normally only includes the rate of small earthquakes) has been extrapolated to higher magnitudes, it underpredicts the rate of larger earthquakes by roughly a factor of 2-3 as compared to the number seen in the historical record. This initially led people to propose the characteristic earthquake model (e.g. Schwartz and Coppersmith (1984) and Wesnousky (1994)), where the Gutenberg-Richter (GR) model was no longer valid across the entire magnitude range. A way to reconcile the GR relationship with the mismatch of historical and extrapolated instrumental data is if we allow the seismicity rate to vary in time. A few previous studies have hypothesized this, suggesting that the missing aftershocks of larger events we have not recorded would increase the average rate of smaller earthquakes as a whole, allowing the entire catalog to follow the GR law (Page and Felzer, 2015; Naylor, Main, and Touati, 2009).

We base our model on this fact that earthquake rate is not constant, and we are missing larger earthquakes with longer recurrence times and all their aftershocks. The aftershocks themselves do not release a significant amount of moment, but they do increase the average rate of smaller earthquakes so. We model missing larger earthquakes and aftershocks, assuming the entire distribution follows the GR law, and aftershocks also follow the GR law with the maximum magnitude aftershock as 1.2 below the mainshock (Bath's Law). When we have completed the modeled catalog, we can see where it intersects the moment build-up line, and therefore find the expected magnitude and recurrence time of the largest earthquake on that fault.

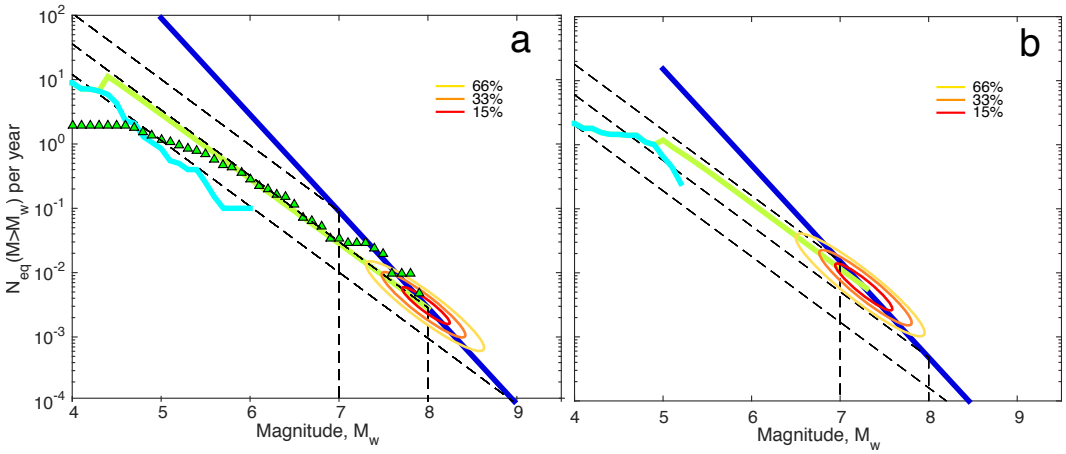

Figure 0.8: GR plot for a) the San Andreas Fault and b) the Boconó fault. The dark blue lines show the moment build-up line. The light blue lines show the instrumental data for the past 20 years. The green straight lines show the modeled complete earthquake catalog. The green triangles show the historic data. The colored ovals indicate the probability that the maximum magnitude earthquake would fall within them.

This model was then tested on faults with historic data. Figure 0.8a shows the results of my modeled catalog compared to the historical catalog on the San Andreas Fault (SAF) and the maximum sized earthquake my model would predict. Figure 0.8b shows the results for the Boconó fault, in Venezuela, an example where we do not have historical data. The uncertainties with this method are high, but it gives a first estimate of M_{max} in areas of sparse data, and uncertainties will decrease in the future as the uncertainties on the input parameters decrease.

This new model is important, particularly in areas of sparse data, where there have not been large earthquakes in living memory, as it provides information about the potential size and recurrence time of the hazard. This highlights the seismic risk and allows increased awareness and preparedness for future large earthquakes. Future work could benefit from using dynamic models to analyze the statistics of earthquake catalogs (e.g. Lapusta and Rice (2003) and Lapusta and Liu (2009)). This would allow the investigation of the time-dependent seismic hazard, rather than just the long-term average hazard.

In the future, more geodetic studies will narrow down the uncertainty on the moment build-up rates, and a longer instrumental record will decrease uncertainties on the average rates of earthquakes. However, what we really want to have is an

instrumental catalog and geodetic data that covers an entire seismic cycle on a large fault. For real observations, we would have to wait hundreds to thousands of years, however physics-based dynamic models (e.g. Lapusta and Rice (2003) and Lapusta and Liu (2009)) could help us in the future to extrapolate seismicity rates of small earthquakes to larger ones. Our methods have been designed to assess the long-term average seismic hazard only, and it would be useful to also extend the work to consider time-dependent seismic hazard analysis.

The following four chapters present four articles that I have written during my PhD, two of which have already been published. In Chapter 1, I show that the MHT is the main area of strain buildup in the region, and that the GPS strain rates are constant with time. Chapter 2 is the first paper I wrote about using GPS data near the MHT to find the coupling pattern and seismic moment build-up rate. Chapter 3 is also a published paper, and uses the results from Chapter 2 to find the larger earthquake needed to balance the seismic moment budget. Chapter 4 builds on the method of Chapter 3 to expand the method to areas with no historic earthquake data.

Chapter 1

CONSISTENT SEISMICITY AND STRAIN RATES IN THE INDIA-ASIA COLLISION ZONE

ABSTRACT

We compare the geodetic strain rate field over the India-Asia collision with seismicity. We find a correlation between the background seismicity rates, estimated from the rate of independent earthquakes, and geodetic strain rates. We also show that the orientation of strain release by earthquakes, estimated from their moment tensors, agrees with the orientation of elastic strain build up calculated from the geodetic data. These observations show that geodetic strain rates can be assumed stationary through time on the timescale needed to build up the elastic strain released by earthquakes, which is typically of the order of 100-1000 years. This means that geodetic data in the Tibet-Himalaya region can be extrapolated back in time to estimate strain buildup on active faults or the kinematics of continental deformation. A corollary is that the geodetic strain rate and long-term slip-rates on active faults should be consistent if geodetic strain is primarily elastic. If strain rate changes significantly, over hundreds or thousands of years, it would be incorrect to compare geodetic rates with historical earthquakes and slip rates calculated from geomorphic/geological offsets.

1.1 Introduction

Over the last few decades GPS geodesy has emerged as a major tool to investigate crustal deformation (e.g. Herring (2010)). Thanks to the effort of many institutions around the world it is now possible to produce relatively detailed strain rate maps of actively deforming regions. These data can be used to infer the kinematics of crustal deformation and the governing dynamic processes (e.g. England and Molnar (1997a)). The data can also be used to monitor interseismic strain rate buildup on active faults and to draw inferences about seismic hazard (e.g. Shen, Jackson, and Kagan (2007), Riguzzi et al. (2012), Stevens and Avouac (2015), and Stevens and Avouac (2016)), which is the motivation for this study. The concept is that seismicity releases the elastic strain that has built up on the fault while it is locked between large earthquakes, and that geodetic data can be used to constrain the rate of elastic strain build up, which places constraints on the rate of seismic moment release over the long-term average (e.g. Avouac (2015), Rong et al. (2014), Kagan and Jackson (2013), and Bird et al. (2015)).

This approach makes two fundamental assumptions that are debatable. Firstly, geodetic strain rate is assumed stationary. This seems to be a reasonable assumption based on the similarity of geodetic strain rate with geological slip rate on a number of continental strike-slip faults (Meade, Klinger, and Hetland, 2013); however, there are counter-examples (e.g. Friedrich et al. (2004), Niemi et al. (2004), Bennett, Friedrich, and Furlong (2004), Oskin et al. (2008), Ganev et al. (2012), Peltzer et al. (2001), and Dolan, Bowman, and Sammis (2007)). One possible explanation is that high deformation rate would switch from one fault to the other. For example, Peltzer et al. (2001) found that strain accumulation rate in the East California Shear Zone is currently three times its average, and the Garlock fault shows no evidence of current strain accumulation, though it has slipped by 7 mm/yr on average over the Holocene. This and other examples suggest that interaction between faults could induce significant temporal variations of loading rates. Temporal variations could also result from viscoelastic reloading (e.g. Kenner and Simons (2005) and Oskin et al. (2007)). Another assumption is that geodetic strain rate is entirely elastic strain. Some fraction of the geodetic strain rate might actually be anelastic. These issues have been debated mostly based on the comparison of geological and geodetic rates. Here we take another approach based on the comparison of geodetic rates with background seismicity rates in the India-Asia collision zone. Earthquakes release elastic strain built up over a duration much longer than the period covered by

geodetic measurements. As a result, temporal variations of strain rates would reflect in geometric inconsistencies between the geodetic strain rate and co-seismic strain rate. Secondly, if the seismicity follows the Gutenberg-Richter (GR) distribution (Gutenberg and Richter, 1944) up to the largest earthquakes, the rate of small earthquakes would reflect the rate of the larger earthquakes. The GR distribution states that $log(N(M > M_w)) = a - bM_w$, where N(M>$M_w$) is the number of earthquakes above M_w, a is the y-axis intercept, and can be thought of as the productivity, and b is the slope. Assuming that interseismic strain rate is entirely elastic, and given that the rate of large earthquakes must scale with fault slip rates (Brune, 1968), we would expect background seismicity rate to scale with geodetic strain rate.

The India-Asia collision zone is an interesting area for this analysis given the sheer size of the deforming area, the intense seismic activity, the diversity of focal mechanism and the recent accumulation of geodetic measurements. Also, the comparison of long term slip rate and geodetic rates on some of the major faults in the area has been much debated (e.g. Mériaux et al. (2004), Chevalier et al. (2005), Brown, Molnar, and Bourlès (2005), Cowgill (2007), and Wright et al. (2004)). A number of studies have combined geodetic and geologic slip rates, and seismicity to determine the pattern and rates of crustal deformation in the area (e.g. Holt et al. (2000), England and Molnar (2005), and Delescluse and Chamot-Rooke (2007)). We do not repeat or revisit such studies, but simply assess the assumption also made in such studies that the strain rate field is stationary. These methods would indeed be incorrect if strain rate changed on a decadal/hundred-year time frame.
Hereafter we first present the strain rate map produced from our compilation of the geodetic data. We next present the seismicity data and discuss the correlation with the strain rate map.

1.2 Geodetic strain rates

We study the region of latitude 10-45° and longitude 65-110° to cover at large the zone of deformation resulting from the India-Asia collision. It includes the entirety of the Himalaya and Tibetan Plateau, as well as the Tien Shan. We use 2369 GPS measurements compiled from the literature (Figure 1a, see Supplements for references). Where necessary, we only took data that had been corrected for the effects of large earthquakes in the original publications. The data spans varying time periods, with the oldest GPS data starting in 1994.

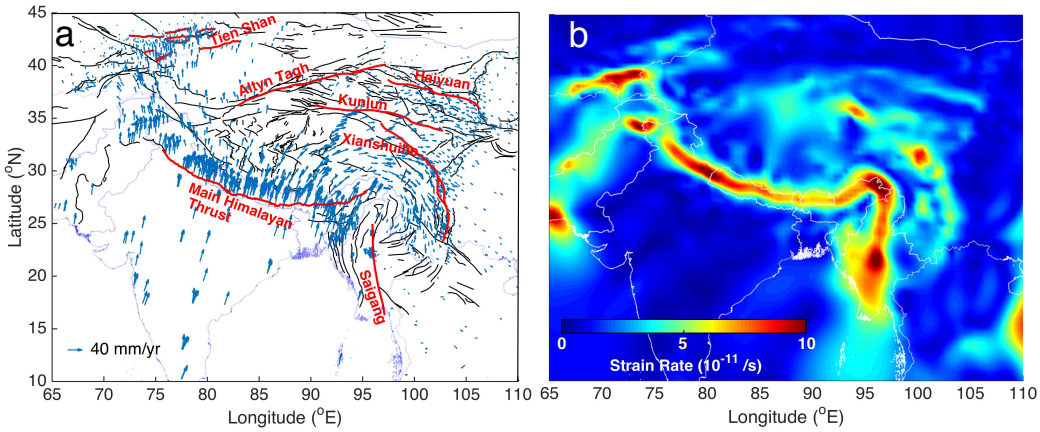

Figure 1.1: a) GPS data used in the strain rate calculation. Black lines show faults from Styron, Taylor, and Okoronkwo (2010) and red lines highlight faults mentioned in the text. b) Second invariant of the strain rate tensor for region of interest calculated from GPS data. For the method and GPS data references see the Methods section.

We used the method of Tape et al. (2009) to determine the horizontal strain rate field. This method uses multi-scale wavelets to match the resolution to the density of observations, so no data points are redundant. The second invariant is plotted in Figure 1b. The zones of higher strain rate correlate relatively well with known active faults (Styron, Taylor, and Okoronkwo, 2010) (Figure 1). The Himalaya clearly stands out as a continuous strip of higher strain rate where the strain rate reaches $10\text{x}10^{-11}$ per year. The shortening rate across the range matches the slip rate on the Main Himalayan Thrust at the few sites where both determinations can be compared, so that in that particular case the geodetic strain rate must be essentially elastic (e.g. Stevens and Avouac (2015)).The high strain rate strip can be seen bending around the eastern and western syntaxes. The North-South striking Saigang Fault on the eastern end shows narrower and then more diffuse deformation, where a number of faults take up the 15 mm/yr rate (Wang et al., 2011). The Tien Shan can also be seen as a region of fairly high strain rate. On the eastern edge of the Tibetan Plateau, from South to North, the Xianshuihe, Kunlun and Haiyuan strike-slip faults can be made out. The Altyn Tagh can also been faintly seen, bordering the north-west edge of the plateau, though there are fewer GPS stations in this region, which perhaps is why it is less prominent. The slightly increased areas of strain rate heading north perpendicular to the Main Himalayan Thrust coincide with extensional grabens. Southwest of the western syntax, there are rather few GPS points, which may be a cause of the broad area of strain rate increase.

1.3 Comparison with seismicity rate

We use 10 years of earthquake data from 2005-2016, taken from the ISC catalog (International Seismological Centre, 2013), with the largest magnitude the 2008 Sichuan M_w7.9 earthquake. We take earthquakes only up to 50 km depth, leaving 122,015 earthquakes. We decluster the earthquakes using the Reasenberg declustering method (Reasenberg, 1985), and end up with 63,225 earthquakes. We used the Shuster Spectrum test (Ader and Avouac, 2013) to verify that the catalogue is well declustered and that the declustered earthquakes are consistent with a Poisson process (See Supplementary Figure S1). Overall, the catalog follows the Gutenberg-Richter law well, and yields a mean b value of 0.94±0.01 (Supplementary Figure S2). The regional seismic moment release rate for the past 10 years ($2.7\text{x}10^{20}$ Nm/yr) is similar to that estimated during the past century ($1.7\pm0.7\text{x}10^{20}$ Nm/yr, Holt et al. (2000)).

The rate of small earthquakes in this catalogue can be assumed to represent the background seismicity rate, as aftershocks have been removed. The study area was divided into regions corresponding to 10 different levels of strain rate, and the earthquakes within each of these areas were extracted (Supplementary Figure S3). The number of events was then normalized by the areas. Gutenberg-Richter plots for each region are shown in Figure 2a.

The Gutenberg-Richter plots within areas of different strain rate show that in general, the higher the strain rate, the higher the rate of smaller earthquakes (less than 6). This is not true for the highest magnitude earthquakes, where they tend to occur in areas of lower strain rate. This is because these areas are larger, so the earthquake record is more complete here than in the areas of higher strain rate. With time we expect catalogs to become more complete so we would see larger magnitudes in the areas of higher strain rate, which are smaller in area. In Figure 2b we compare the strain rate in each region with the normalized earthquake rate. The two rates are correlated and the correlation is much higher than what could result from chance (compare dots and grey lines in Figure 2b). We determine a best fitting linear relation between the rate of earthquakes and strain rate:

$$\dot{E} = 1.05 \pm 0.15 \times 10^{7} \cdot \dot{\epsilon} \tag{1.1}$$

where $\dot{E}$ is earthquake rate per km^2, and $\dot{\epsilon}$ is strain rate per second. The constant has units of seconds per km^2. We also find that the observations are generally within the expected range of variability for a Poisson earthquake process.

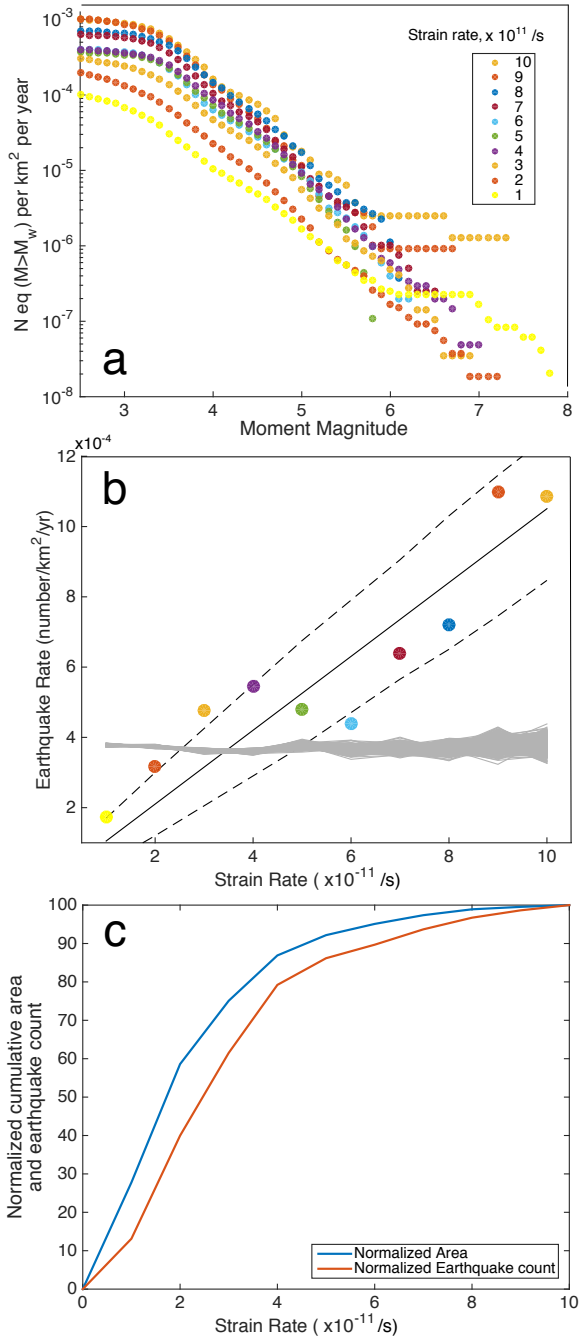

Figure 1.2: a) Gutenberg-Richter plot of declustered catalog within areas of different strain, normalized per area. See Figure S2 for areas of different strain rate. b) Comparison of normalized earthquake rate and strain rate from GPS. Colored dots correspond to discrete regions of different strain rate levels. Grey lines show 100,000 realizations of randomized distributions of earthquakes. These show greater dispersion as strain rate increases because the areas in which these strain rate levels occur decreases. The solid black line shows the linear best fit, and the two dashed lines show the 2-sigma errors on the line, assuming that earthquakes are a Poisson process. c) Strain rate versus normalized cumulative area (blue) and normalized cumulative earthquake count (red).

At medium strain rates the number of earthquakes appears slightly low. This observation is probably due to a methodological bias. These medium strain rate areas tend to be regions surrounding regions of even higher strain rate, where earthquakes do occur at a much higher rate. The actual location of faults here may play a role, as the large faults themselves may cross areas of different strain rate level, and be concentrated in the higher strain rate areas, leaving the medium-strain rate areas relatively earthquake poor. The medium-strain rate areas may be a result of lack of resolution of the GPS, with there actual strain rate levels being lower, as the low density of GPS broadens out the areas of higher strain rate, which would lead to areas of apparently higher strain rate with fewer earthquakes. It may be that not just the strain rate, but also the location of faults is important for earthquake rate. The high earthquake rate in the areas of high strain rate, where the most important faults are, suggests that there is not much aseismic slip else there would not be so high an earthquake rate here.

1.4 Comparison with seismic moment tensors

For the earthquake strain tensors we use the CMT catalog from 1976 to 2016 (Dziewonski, Chou, and Woodhouse, 1981; Ekström, Nettles, and Dziewoñski, 2012). The smallest earthquake is M_w4.6 and the largest is again the 2008 Sichuan M_w7.9. We take earthquakes again up to 50km depth and this leaves 1879 earthquakes.

For every earthquake, the directions of horizontal principal strain were determined using the Kostrov approach (Kostrov, 1974), according to which each earthquake is considered to represent an increment of strain, which is calculated by representing it by an equivalent homogeneous strain of the volume containing the fault. These were then compared with those from the GPS strain rate map (Figure 3). Comparing directions of principal strain from both earthquakes and GPS strain rate field shows that both the directions and relative magnitudes of principal strain are very similar. We do not use absolute magnitudes as large earthquakes would have an overwhelming contribution, but the catalog is not representative of the long term, i.e. the recurrence time of large earthquakes is a lot longer than the 10 years of earthquake data we have used.

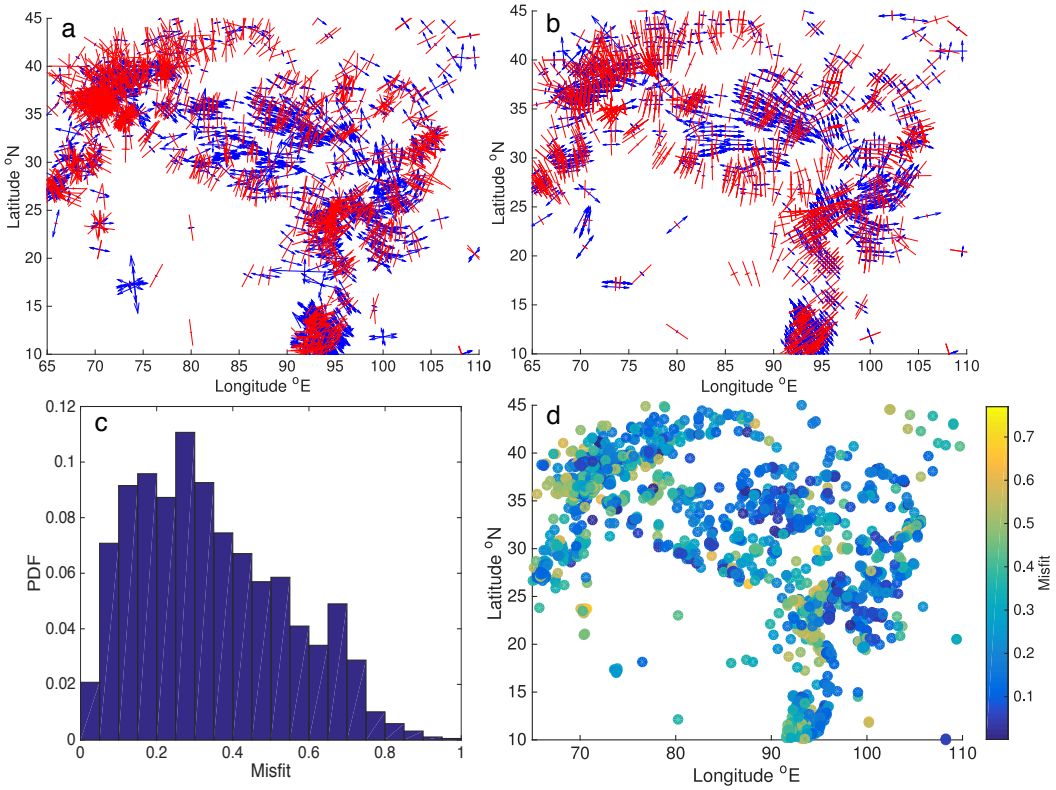

Figure 1.3: Comparison of directions of principal horizontal strains. Red lines show direction of maximum compression and blue arrows show direction of maximum extension. a) Moment tensor solutions. b) GPS strain rate map. c) Misfit of the Frobenius norm between the moment tensor and GPS strain rates, which includes the 3D component and the relative magnitudes. d) Frobenius norm distribution.

Both show strong compression perpendicular to the Himalayan arc, with very small extension parallel. In the Tibetan Plateau itself, there is significant East-West extension and now only minor North-South compression. We use the Frobenius norm (the square root of the sum of the squared differences of each element in the strain rate tensor) to quantitatively compare the geodetic strain rate and moment tensors:

$$||D||_F = \sqrt{\sum_{i=1}^{m}\sum_{j=1}^{n} |a_{ij} - b_{ij}|^2} \tag{1.2}$$

where $||D||_F$ is the Frobenius norm of the difference between the two matrices with components a_{ij} and b_{ij}.

All tensors are normalized to unity so that only the directions and the ratio of principal values are actually compared. It can be seen that the misfit is in general small, and randomly distributed across the area. There are few places where the earth-

quakes and GPS strain rate fit with extremely low misfit (i.e. < 0.1) because both the angle and relative magnitudes would have to be very similar at the same time; it is more likely that one of these quantities is more different. The misfits are overall much better than what would be expected from a random distribution. The probability of obtaining such a low median misfit randomly is less than 1% (See Supplementary Figure 1.S3).

We estimated the expected level of misfit given the uncertainties on the moment tensors and on the GPS strain rates. To do so we assumed that nearby measurements (at distance less than 100 km) can be considered to represent independent measurement of the same quantity. We then calculated the standard deviation of the Frobenius distance between such data, and this expected misfit was used to simulate earthquakes that 'perfectly' fit the GPS strain rate data (Supplementary Figure S4). This calculation shows that the misfit between the seismic moment tensors and the geodetic strain rate tensors is still larger than values expected if the tensors were perfectly collinear, taking into account the data uncertainties. The discrepancy may be due to some variation in strain rate with time, but also may be due to strain partitioning, where the earthquake moment tensors are influenced by the geometry of faults on which they occur.

We find that over the broader regions, not just on large faults, there is agreement between earthquakes' strain release and GPS strain rate. This is more evidence that the strain rate field from GPS has been consistent at a timescale of thousands of years and is representative of the stress field that is driving strain release by earthquakes.

1.5 Discussion-Conclusion

Our study shows that seismicity rate determined using small and moderate independent earthquakes correlate well with geodetic strain rates over the India-Asia collision zone. The strain rate is calculated from the GPS, which records at the decadal timescale, whereas the earthquake rate reflects strain release events of strain accumulated on a centennial to millennial timescale. The stress build up rate on active faults is typically 1-10 kPa/yr in the Himalayan region (Bollinger et al., 2004a) and similar in California (Parsons, 2006; Freed, Ali, and Bürgmann, 2007), compared with a typical stress drop of 1-10 MPa (e.g. Kanamori and Brodsky (2004)), so

the time needed to reload a fault after an earthquake is typically 100-1000 years. The correspondence between strain rate and earthquakes suggests that the geodetic strain field is representative of stress built up over the longer timescale.
A similar correlation has been found at subduction zones by Kagan (1999). Such spatial correlation is the equivalent in space of correlation in time between post-seismic strain rates and aftershocks (e.g. Perfettini and Avouac (2004) and Hsu et al. (2006)) or between seasonal variations of strain and seismicity observed in the Himalaya (Bettinelli et al., 2008). The fact that the correlation holds in areas of smaller strain rates suggests that even in those areas, geodetic strain is probably dominantly elastic and released by seismicity in the longer run. If this were not the case, we would expect a cutoff strain rate, below which we would get no seismicity, but instead strain release by viscous flow.

As observed in Italy (Riguzzi et al., 2012), we find that larger earthquakes fall in area of lower strain rate. This observation is probably a bias due to the earthquake catalogs being more complete in those larger areas than in the smaller areas of higher strain rate. We suspect that this bias might also explain the similar correlation observed in Italy.

We find that past seismicity rates and strain rates match, suggesting that GPS and background seismicity rates may be considered constant through time. The correlation between principal strain directions of geodetic surface strain and moment tensors also suggests that the geodetic strain rate tensor has not changed much through time either. This means the current strain rates measured over decades can be extrapolated back in time to evaluate strain build up on active faults over the entire interseismic period. It means that we can assume the same rates on faults back in time, and so can use the historic and paleoseismic record in conjunction with rates from geodetic data to study seismic hazard. This lends support to the practice of combining geologic slip rates and seismicity data to develop kinematic models of continental deformation (Haines and Holt, 1993; Holt, Li, and Haines, 1995; England and Molnar, 1997b) or based on elastic block modeling (e.g. Meade and Hager (2005)).

Supporting Information for "Consistent Seismicity and Strain Rates in the India-Asia Collision Zone"

Introduction

Here we show extra figures relating to data. GPS data was compiled from the literature (Bettinelli et al., 2006; Calais et al., 2006; Socquet et al., 2006; Gan et al., 2007; Jade et al., 2007; Banerjee et al., 2008; Yang, Li, and Wang, 2008; Maurin et al., 2010; Mohadjer et al., 2010; Mukul et al., 2010; Zubovich et al., 2010; Jade et al., 2011; Ponraj et al., 2011; Ader et al., 2012; Mahesh et al., 2012; Szeliga et al., 2012; Gahalaut et al., 2013; Ischuk et al., 2013; Liang et al., 2013; Schiffman et al., 2013; Jade et al., 2014; Kundu et al., 2014; Vernant et al., 2014; Jouanne et al., 2014; Wang et al., 2014; Gupta et al., 2015).

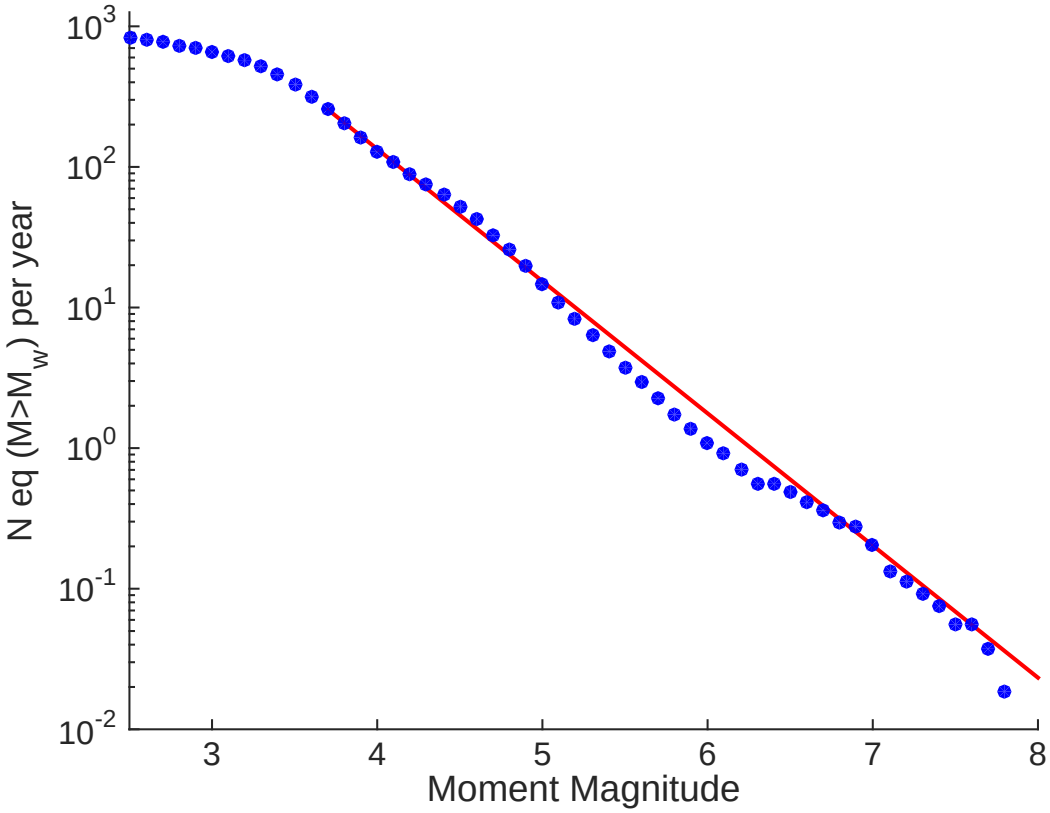

Figure 1.S1: Gutenberg-Richter plot showing the entire declustered catalog as blue circles. The b value calculated from the maximum likelihood method (Aki, 1965) is 0.94±0.01, and the mean is shown as the red line.

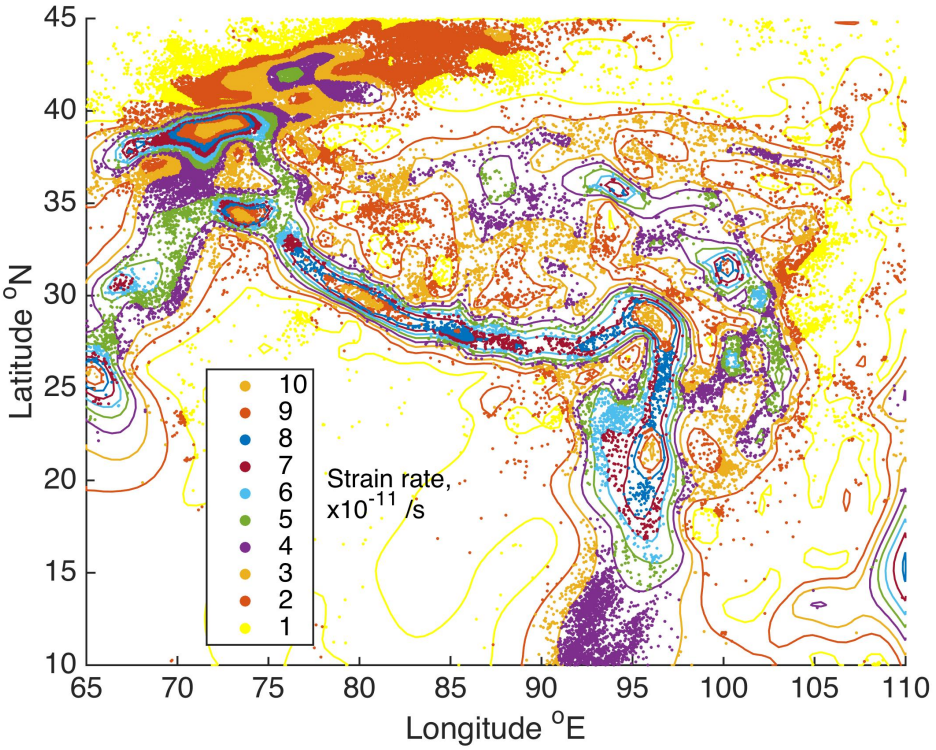

Figure 1.S2: Plot showing boundaries of areas of different strain rate from GPS data, and the locations of earthquakes within them, both color-coded by different strain rate.

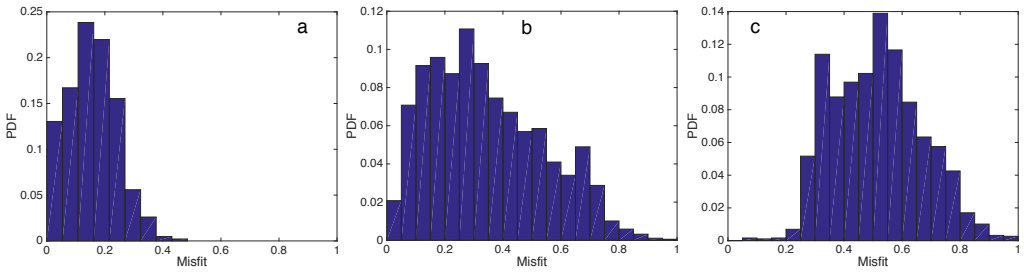

Figure 1.S3: Probability density functions (PDFs) of Frobenius norm misfit of strain rate tensor to GPS strain rate tensor. a) Modeled strain that is perfect GPS strain plus a standard deviation of 0.13±0.075. b) Real data from earthquake strain. c) Modeled completely random strain. The median misfit is 0.16, 0.31, and 0.51 respectively.

Chapter 2

INTERSEISMIC COUPLING ON THE MAIN HIMALAYAN THRUST

(Published as “Interseismic coupling on the main Himalayan thrust" by V. L. Stevens and J. P. Avouac, Geophysical Research Letters, 2015)

ABSTRACT

We determine the slip rate and pattern of interseismic coupling on the Main Himalayan Thrust (MHT) along the entire Himalayan arc based on a compilation of geodetic, InSAR and microseismicity data. We show that convergence is perpendicular to the arc and increases eastwards from 13.3±1.7 mm/yr to 21.2±2.0 mm/yr. These rates are comparable to geological and geomorphic estimates, indicating an essentially elastic geodetic surface strain. The interseismic uplift rate predicted from the coupling model closely mimics the topography, suggesting that a small percentage of the interseismic strain is permanent. We find that the fault is fully locked along its complete length over about 100 km width. We do not find any resolvable aseismic barrier that could affect the seismic segmentation of the arc and limit the along strike propagation of seismic ruptures. The moment deficit builds up at a rate of $15.1\pm1 \times 10^{19}$ Nm/yr for the entire length of the Himalaya.

2.1 Introduction

There is now a relatively good coverage of GPS measurements of surface displacements spanning the Himalayan arc (Figures 2.1 and 2.S1). These data indicate that the Himalaya accommodates about half of the 40 mm/yr convergence rate between India and Eurasia as some earlier studies have shown (e.g. Bilham, Larson, and Freymueller (1997), Larson et al. (1999), Jouanne et al. (2004)). The high strain rate there is consistent with the high seismic hazard associated with the range. The Himalayan range has indeed produced a number of deadly earthquakes recently (e.g. M_w 7.8 Nepal 2015, M_w 6.9 Sikkim 2011 and M_w 7.6 Kashmir 2005) and has been known for even larger historical earthquakes of magnitude more than 8 (e.g. the M_w 8.5 Assam 1950 (Chen and Molnar, 1990) and the M_w 8.2 1934 Nepal-Bihar earthquakes (Sapkota et al., 2013), indicating that a fraction of the geodetic strain rate is elastic strain which is ultimately released by earthquakes.

A primary objective of this study is to assess how much of the geodetic strain is actually elastic and to quantify the current rate of moment deficit accumulation along the Himalaya. This quantity is of importance as it sets the seismic hazard level (Bilham, Gaur, and Molnar, 2001) . We also aim to assess if this pattern is spatially stationary through time in the interseismic period, or whether it can vary significantly. To answer these questions, we adopt the same methodology as Ader et al. (2012), who focused on the Nepal Himalaya, but consider the entire Himalayan range based on a regional compilation of recent GPS, Synthetic Aperture Radar interferometry (InSAR), and microseismicity data. As a starting point we assume that, as demonstrated for the Himalaya of central Nepal, the long-term shortening rate across the range is entirely taken up by slip along the Main Himalayan Thrust (MHT) fault, the basal fault along which the Himlayan wedge is thrust over the Indian crust (e.g. Cattin and Avouac (2000)). The geodetic data can then be used to determine both the long term slip rate on the fault and the pattern of interseismic coupling. Interseismic coupling is defined as the ratio of interseismic deficit of slip rate to long term slip rate (1 if the fault is fully locked and 0 if it is creeping at the long term slip rate). The pattern of interseismic coupling can reveal locked patches where future earthquakes might occur, or aseismic barriers that can arrest earthquake ruptures, and allows us to calculate the rate of accumulation of moment deficit (Chlieh et al., 2008; Moreno et al., 2011; Avouac, 2015). Hereafter, we first describe the data set and the method used. We next discuss the modelling results and implications.

2.2 Data

GPS

There has been a considerable amount of new GPS data from the Himalayan arc area published during the past few years. Coverage is irregular but now extends all the way along the Himalayan arc. We compiled the GPS data from the literature (Bettinelli et al., 2006; Calais et al., 2006; Socquet et al., 2006; Gan et al., 2007; Jade et al., 2007; Banerjee et al., 2008; Mukul et al., 2010; Jade et al., 2011; Ponraj et al., 2011; Ader et al., 2012; Mahesh et al., 2012; Gahalaut et al., 2013; Liang et al., 2013; Schiffman et al., 2013; Jade et al., 2014; Kundu et al., 2014; Vernant et al., 2014). All the data were expressed in the same ITRF2005 reference frame.
Where the GPS were highly spurious (e.g. where there were three measurements at one station, and one of the measurements greatly differed, or if the GPS velocity visually stuck out from the overall pattern), perhaps due to very local earthquakes, they were removed from the dataset (see Dataset S1), or errors were doubled. The GPS were then converted into the fixed India reference frame using the pole of Ader et al. (2012). The details of GPS processing can be found within the relevant papers. For the coupling model, 39 continuous stations and 174 campaign stations were used - those that were within 300 km of the fault trace. (Figure 2.S1). Measurements at the same location were averaged, and weighted according to their uncertainties.

Leveling and InSAR data

The pattern of coupling on a megathrust is better resolved where constraints from vertical displacements are available. Such constraints can be provided by leveling or InSAR measurements. We used leveling data from the Survey of Nepal collected between 1977 and 1990 (Jackson and Bilham, 1994). The Survey followed a road through the Himalaya of central Nepal, and the location of the data can be seen in Figure 2.S1. The uncertainties on the leveling data are low with respect to those on the GPS vertical and help constrain well the pattern of coupling locally (Ader et al., 2012).
We used the InSAR data from a swath over the Kali Gandaki area area in Central Nepal (Grandin et al., 2012) (Figure 2.S1). The radar images were acquired between 2003 and 2010. The InSAR data were down-sampled uniformly across the area by simply averaging nearby pixels, to use 41 points in the inversion (Figure 2.S1). These data, which were not used by Ader et al. (2012), improve the resolution significantly between 83°E and 84°E and from near the fault trace to 29°N.

Microseismicity

The background crustal seismicity in the Himalaya is known to consist mainly of thrust events in the area of stress build up fringing the downdip end of the locked portion of the MHT (e.g. Cattin and Avouac (2000), Bollinger et al. (2004b)). As such, these data can be used to help constrain interseismic coupling on the MHT. Within Nepal, earthquakes were taken from a relocated catalog of the National Seismological Centre (NSC), recorded between 1995 and 2001 (0.8<M<5.5) (Ader et al., 2012; Rajaure et al., 2013). Between 77° and 81°E, seismicity from a second relocated catalog, recorded between April 2005 and June 2008 was used (1<M<5) (Mahesh et al., 2013). Elsewhere, we used the NEIC catalog from 1964 to 2014 (4<M<7.7). Earthquakes from areas of active rifts in southern Tibet and events deeper than the Moho were removed from the catalogue so that only the crustal seismicity presumably associated to stress build-up on the MHT was kept.

Long-term shortening rate estimates on the MHT

The long-term shortening rate on the MHT has now been estimated at a number of locations along the Himalayan front from geomorphic and geological studies (Table 2.S1). These data are used in this study for comparison to the long term shortening rates on on the MHT determined from the modeling of the geodetic data. In the Northwestern Himalaya, geomorphic studies of offset terraces give long-term shortening rates of 11-14 mm/yr (Thakur et al., 2014; Parkash et al., 2011; Wesnousky et al., 1999). In Nepal, geomorphic and structural studies give rates of 18-21 mm/yr (Lavé and Avouac, 2000; Bollinger et al., 2014; Mugnier et al., 2003). At the eastern end of the Himlayan range, further geomorphic studies give similar shortening rates of 20-23 mm/yr (Burgess et al., 2012; Berthet et al., 2014).

2.3 Methods

We follow the method of Ader et al. (2012), but extend the model from just Nepal to the whole Himalayan range. As well as considering a larger area, an additional dataset within Nepal (InSAR) and the wealth of GPS data now available elsewhere, we also modify the modeling technique to incorporate the microseismicity information. We invert the GPS, leveling and InSAR data using the backslip approach (Savage, 1983) to solve for the long-term velocities and the pattern of coupling on the MHT. The slip deficit (which gives the pattern of coupling) and long-term slip rates computed from the Euler poles describing long term block motions are

summed together to model the GPS motions. The method assumes that interseismic surface strain is entirely elastic deformation driven by the pattern of creep on the MHT. This assumption is tested later by comparing GPS-derived horizontal shortening rate (calculated from the slip rate on the fault plane and its dip) with geomorphic/geological shortening rates.

We consider the total length of the arc, roughly 2000 km, from 73°E to 96°E. Due to the arcuate-shape, we simplify the fault geometry (based on Styron, Taylor, and Okoronkwo (2010)) into five planar subfaults (Figure 2.S2). To allow for previously seen along-strike variations of the shortening rate across the range (e.g. Jouanne et al. (2004), Schiffman et al. (2013), and Vernant et al. (2014)), we divide the arc into six different sections (Figure 2.S2). We calculate the best fitting shortening rate within each of them. The boundaries of these sections were picked where the GPS appeared to change most, and to coincide with the main extensional grabens in Southern Tibet and across the arc (Gan et al., 2007; Kundu et al., 2014; Hurtado, Hodges, and Whipple, 2001) (Figure 2.S2). Slip on the MHT is allowed to happen in the strike-slip and dip-slip directions. We have taken the role of extension in a simplified way by assuming it is homogeneously distributed (as also assumed in Ader et al. (2012)).

The assumption of a rigid-Indian plate breaks down around the eastern end of the Himalayan arc where there is evidence for internal deformation (Vernant et al., 2014). To account for this deformation, we consider two blocks south of the eastern Himalaya (Figure 2.2), the eastern-most one being the Assam block, and the other the Shillong block. The inversion solves for the poles of rotation of these two blocks with respect to India, as well as the long-term velocity on the MHT and the coupling pattern.

The fault is discretized into 2057 patches (17 downdip and 121 along strike, with dimensions roughly 15 x 17 km). The dip angle is set to 10° as in previous studies (Ader et al., 2012; Jouanne et al., 2004). Note that the fault geometry is idealized as it does not need to present the real ramp-and-flats geometry of the fault where it is locked (Vergne, Cattin, and Avouac, 2001). The elastostatic Green's functions relating unit slip on each patch to surface displacements at the data locations are computed using Okada's solution (Okada, 1985). We assume an elastic half space with Poisson coefficient of 0.25. The modeling is independent of the shear modulus. We take a value of 30 GPa to estimate moment from slip potency. The backslip azimuth is assumed equal to the azimuth of the long term slip rate predicted by the Euler poles describing the rigid block motion of the various blocks. For each patch,

the degree of interseismic coupling (i.e. locking) is found from the ratio of the slip deficit rate to the long-term slip rate. A value of 0 implies the fault patch is entirely creeping at the long-term slip rate, and a value of 1 implies it's fully locked. Figure 2.S2 shows the model setup.

We solve the equation $d = GM$ where d = data vector of 611 parameters, G = Green's function matrix (using Okada (1985)), m = unknown parameters we want to solve for (slip rates on 2057 fault patches, long-term velocities in six sections and two poles of rotation (for each of the two eastern blocks).

Because the inversion is ill-posed, as the number of parameters exceeds the number of data points, we regularize the inversion by penalizing the roughness of the slip-distribution. In practice, we minimize the Laplacian of the slip distribution. As in Ader et al. (2012), the weight put on the Laplacian is adjusted according to the resolution on each path, and 3 times stronger in the along strike direction than down-dip, as we expect there to be rapid variations along dip, but less rapid variations along strike. The resolution is calculated using the Moore-Penrose pseudoinverse matrix (Aster, Borchers, and Thurber, 2013). We calculate the correlation of each patch with its neighbours and then weight each line of the Laplacian matrix by the decimal logarithm of the resolution size on the corresponding patch. The Laplacian is also regulated using the microseismicity information. We use the fact that that microseismicity seems to follow areas with a large gradient of coupling (the downdip edge of the locked fault zone) where stress build-up is maximum (Cattin and Avouac, 2000; Bollinger et al., 2004b). To encourage gradients of coupling to locate in areas of higher seismicity, the weighting on the Laplacian is reduced there. In practice the weight is inversely proportional to the number of events in that patch to the power of a third.

The shape of the arc and extension in the Tibetan plateau causes a strike-slip component to appear at the down dip end of the modeled fault, 230-250 km north from the surface trace, which is an artifact of the model. To reduce this effect, we minimize the coupling at the down dip end, while elsewhere strike-slip motion is allowed freely.

As in Ader et al. (2012) we determine the distribution of backslip on the fault by minimizing the chi-square criterion

$$\chi^2(\mathbf{m}) = \| \mathbf{C_d}^{-1/2}(\mathbf{Gm} - \mathbf{d}) \|_2 + \lambda \| \Lambda\mathbf{m} \|_2 + \mu \| \mathbf{I_d}\mathbf{m} \|_2 \qquad (2.1)$$

where $\mathbf{C_d}$ is the data covariance matrix, Λ is the Laplacian matrix, $\mathbf{I_d}$ is the matrix which gives the slip at depth when multiplied by $\mathbf{m}$, λ and μ are weights on the constraints. We use $\lambda = 1.1$ and $\mu = 0.01$ to penalize the strike-slip component at depth, with $\mu = 0$ elsewhere than along the downdip end of the fault. The datasets are weighted equally, as the reduced chi-squared calculated from the misfit between the observations and model prediction is similar for them all. After the inversion, we constrain the interseismic coupling value to lie between 0 and 1 by simply thresholding values above 1 and less than 0. Before the constraint, roughly 15% of the data lie outside of the permitted 0-1 range. Both the strike-slip and dip-slip components of each fault element and long-term velocities are used in the coupling calculation. We have not tested for the effect of earth sphericity, which we assume to be small as the strain signal is always dominated by local gradients of coupling. For a more detailed description of the method, see Ader et al. (2012).

2.4 Results and Discussion

The coupling pattern and long term shortening rates

The pattern of coupling and long term slip rates on the MHT corresponding to our best fitting model is shown in Figure 2.1. The reduced chi-squared is 2.84, suggesting that some of the signal is not explained by the model's assumptions or that uncertainties are slightly underestimated. This model explains 92 % of the data variance. Long-term velocities are found to be about 18-20 mm/yr across most of the arc, decreasing in the west to about 13 mm/yr.

The poles of rotation of the Assam and Shillong crustal blocks are listed in Table 2.S2. The poles agree with those found by Vernant et al. (2014) for similar blocks, although the rotation rate for the Shillong block is about 50 % lower in our solution. This may be due to the difference of block geometry or the tradeoff with long-term velocities. Imposing the Euler poles of Vernant et al. (2014) does not alter the results significantly (Figure 2.S3). The fit to the data changes depending on the regularization and the weight put on by the smoothing. Using the microseismicity to regulate the Laplacian, as in Figure 2.1, the reduced chi-squared calculated from only the misfit between the observations and model prediction is 3.09, only 8 % larger than the value of 2.84 obtained with a homogenous (though still weighted by data resolution) Laplacian. Figure 2.S4 shows an inversion with the same parameters but not using the microseismicty to regulate the Laplacian. The difference between the two models is modest. The main difference is that where the sensitivity

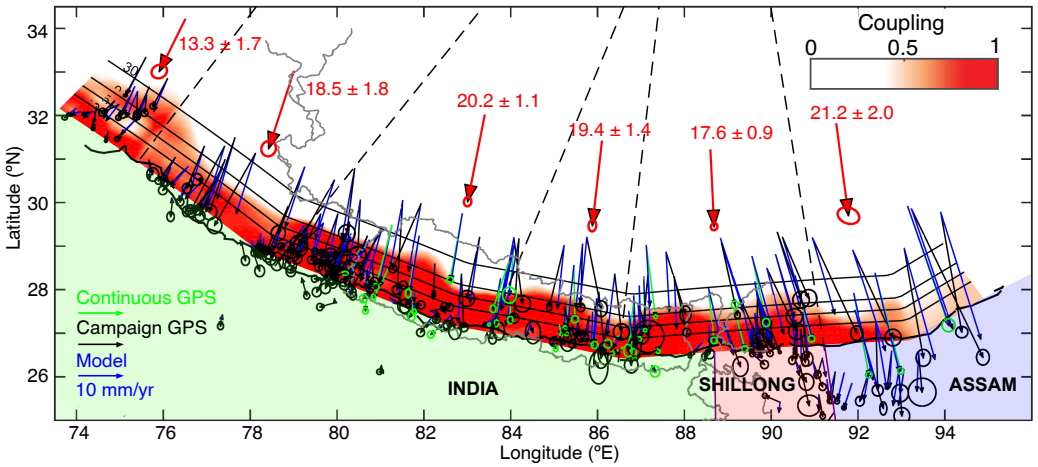

Figure 2.1: Coupling model and fit to the horizontal GPS data. The interseismic coupling is shown as shades of red. A coupling value of 1 means the area is fully locked, while a value of 0 means fully creeping. The green and black arrows and ellipses show the continuous and campaign GPS velocities (in the fixed-Indian reference frame of Ader et al. (2012)), with their error bars, respectively. The blue arrows are the modeled velocities, which fit with the coupling shown. The large red arrows show the long-term velocities in each region. The dashed black lines show the separation of the regions, within which the long-term velocity for that region is calculated, as shown by the large red arrows. The solid black lines, labeled at 10 km intervals, show the depth contours of the fault plane. The labels INDIA, SHILLONG and ASSAM refer to three blocks which are assumed to be rigid. The residuals to the horizontal GPS, the InSAR and leveling data are shown in Figure 2.S5. Electronic data of the coupling pattern are included in an SI file.

of the geodetic data is low, the downdip end of the locked fault zone in the model of Figure 2.1 coincides better with the zone of microseismic activity (Figure 2.2) than the model with homogeneous Laplacian weighting (Figure 2.S4).
No systematic residuals are found (Figure 2.S5), though larger residuals can be seen in the very east where the resolution is poorest (Figure 2.S6). In places of low resolution, microseismicity helps in resolving the location of the downdip transition from locked to creeping.

The coupling pattern in Figure 2.1, the best fit to all the available data, shows that the fault is locked along its length to roughly 100 km downdip from the surface. The locking is nearly binary, as in there is a sharp transition between the locked and creeping zones. One exception is the very western end, where the fault appears to be locked to a much wider width, and the transition is more diffuse. This could be

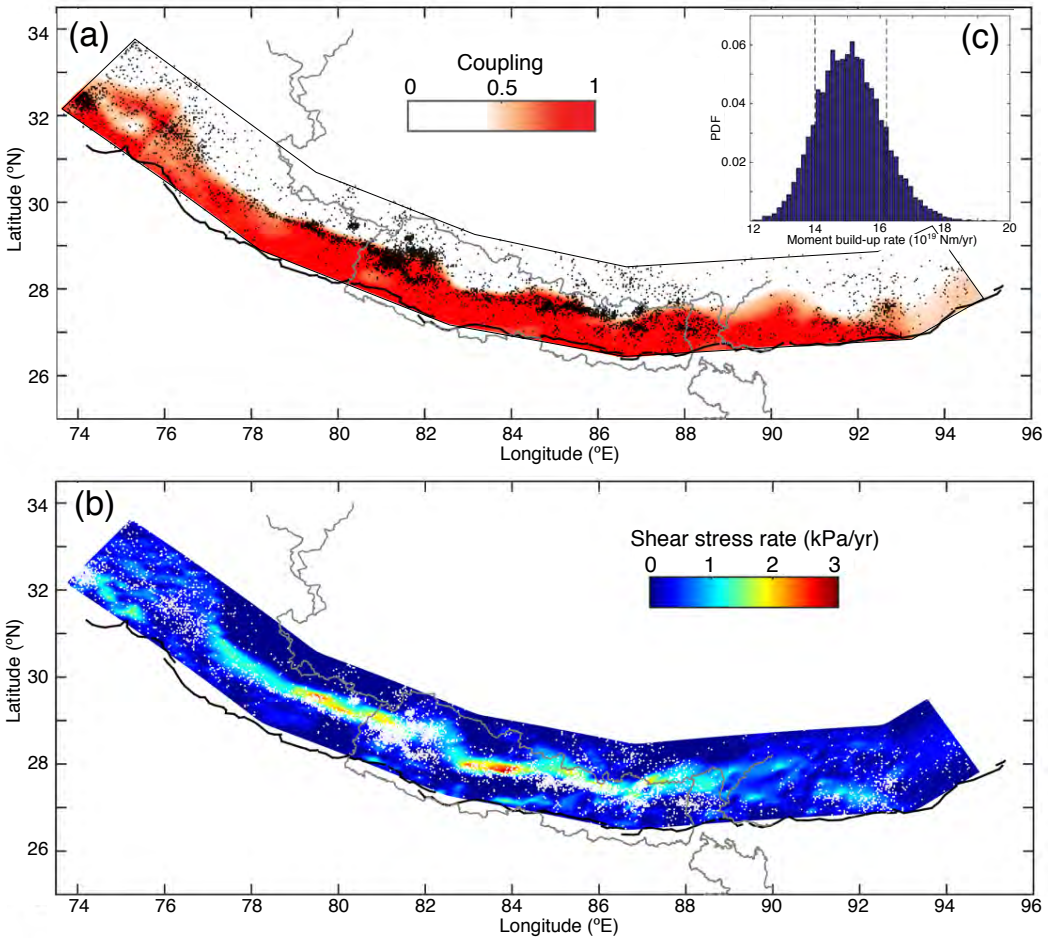

Figure 2.2: (a) The same coupling model as in Figure 2.1, with the location of seismicity used to regulate the Laplacian smoothing. Seismicity within Nepal is from an NSC catalog (Ader et al., 2012; Rajaure et al., 2013) seismicity between roughly 77°E and 81°E is from Mahesh et al. (2013) and the remainder is from NEIC. The modeled fault is outlined in black. (b) Shear stress accumulation rate on the fault plane, calculated from the coupling pattern, overlain by the same microseismicity as in Figure 2.2a, here shown as white dots. Electronic data of the stress rate pattern are included in an SI file. (c) Probability distribution function of the total moment build-up rate per year. Dashed lines show one standard deviation.

due to a more distributed zone of deformation in that part of the Himalaya (Thakur et al., 2014) or the sparsity of GPS data. The lower coupling at the eastern end could be a reflection of lack of data in the area, and the complexity of local tectonics. Overall the coupling pattern shows very little along-strike variation. This is much different from the heterogeneous pattern of coupling observed at subduction zones (see Avouac (2015) for a review), though similar to the findings of Cheloni, D'Agostino, and Selvaggi (2014) who find a uniform pattern of coupling along the southern front of the Alps.

The lack of creep, and the fairly homogenous coupling pattern in the 0-20 km seismogenic depth range, suggests that there are no obvious aseismic barriers that would arrest seismic ruptures.

Figure 2.2 confirms that background seismicity generally falls in the area of interseismic stress build up. The correspondence is especially clear where the catalogs have been relocated, between about 77°E and 88°E. The correspondence of seismicity and the downdip edge of the locked zone has also been observed for the southern front of the Alps (Cheloni, D'Agostino, and Selvaggi, 2014). As expected, the model that does not use the seismicity to regulate the Laplacian does not have such quite good correlation, though it is still notable (Figure 2.S4). Noteworthy is the fact that the relocated catalogue of Mahesh et al. (2013) which extends from 77°E and 81°E follows the downdip edge of the locked fall zone quite well also in the model of Figure 2.S4 where we haven't used the seismicity to weight the Laplacian smoothing. This observation confirms the correlation already noted for Nepal (Cattin and Avouac, 2000; Bollinger et al., 2004b; Ader et al., 2012). It is thus probably valid to assume that this correlation holds for the whole Himalayan arc. This suggests that if microseismicity elsewhere was better relocated, it would fall in a more compact area around the transition zone and help constrain better the coupling pattern.

Evidence that interseismic strain is primarily elastic and stationary

To test the assumption of elasticity, we compare estimates of long-term slip rates from geomorphic and structural studies to our geodetic estimates (Figure 2.3, Table 2.S1). The close correspondence suggests that most of the interseismic deformation is elastic. If a significant amount of deformation were permanent, the long-term convergence rate predicted by the geodetic data would be higher than the conver-

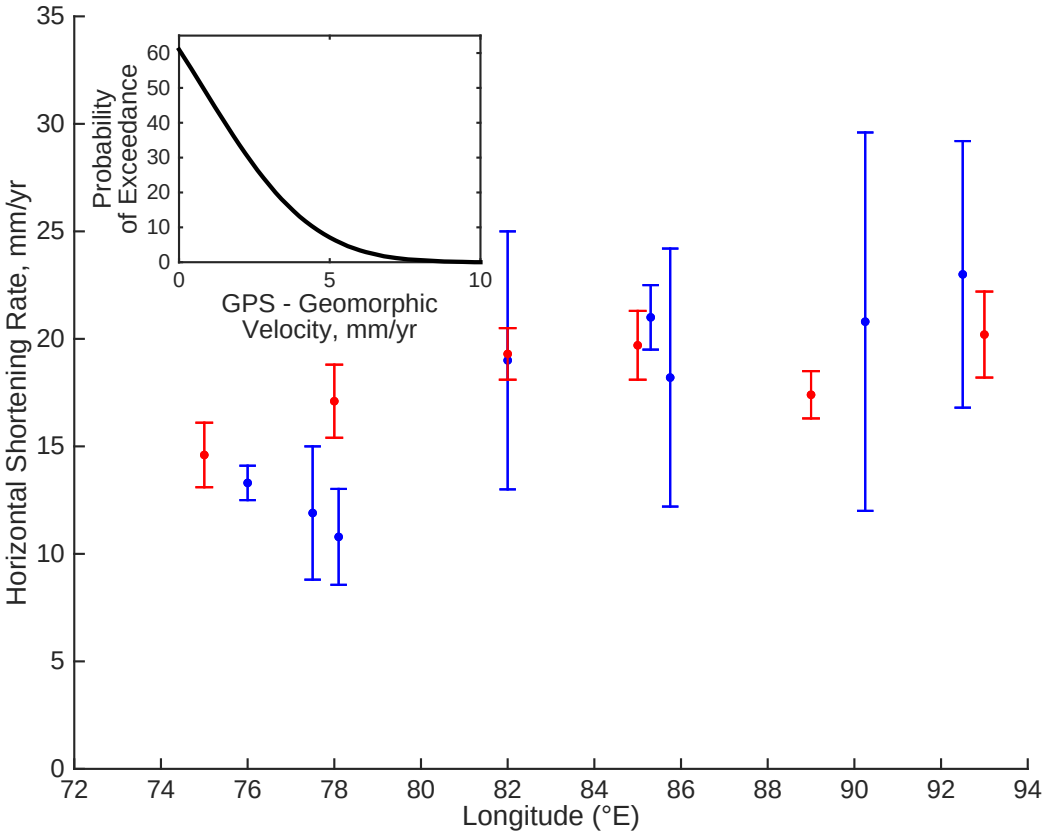

Figure 2.3: Shortening rate across the Himalayas from the results of this study (red) and geomorphic studies (blue). Geomorphic data from west to east are from (Thakur et al., 2014; Wesnousky et al., 1999; Parkash et al., 2011; Mugnier et al., 2003; Lavé and Avouac, 2000; Bollinger et al., 2014; Berthet et al., 2014; Burgess et al., 2012). Inset shows the probability that the average modeled long-term GPS velocities exceed the average velocities from geomorphic studies by different amounts.

gence rate found at the surface trace of the MHT. We see this happen outside of uncertainties only at one point, in the western Himalaya. This confirms the assumption that strain rate is elastic, geodetic convergence rates must vary little with time and that anelastic strain of the upper crust in the interseismic period is small. Taking the geological and geodetic rates and associated uncertainties at face value, we can estimate the possible amount of geodetic shortening in excess of the geological rate that could reflect anelastic strain (Figure 2.4). After averaging the data, we find that the probability that anelastic interseimic convergence rate exceeds 2 mm/yr (hence about 10 % of the geodetic shortening) is only 30 %.

Figure 2.4 shows that the azimuth of slip during thrust events along the Himalayan arc is closely parallel to the azimuth of the long-term convergence determined from

geodesy. This observation also indicates that interseismic strain is probably spatially stationary with time.

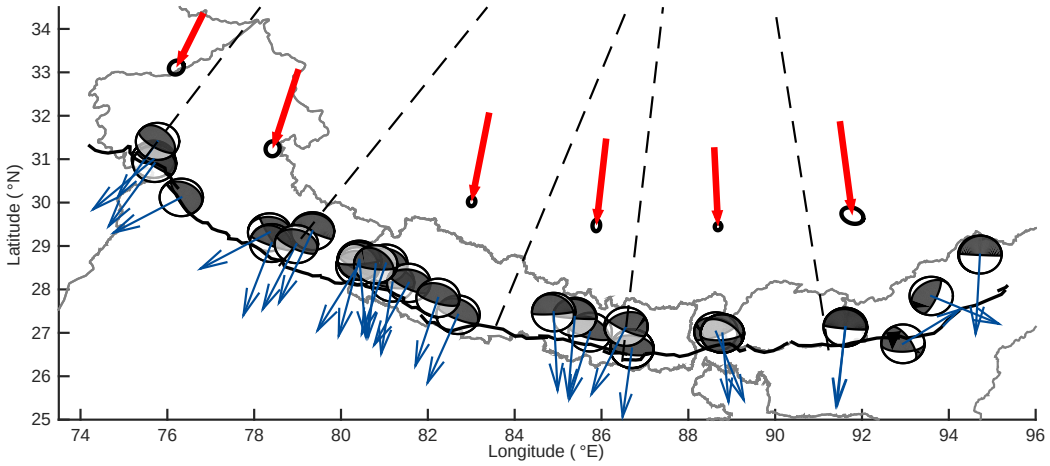

Figure 2.4: Focal mechanisms from the CMT catalog. Blue arrows show the direction of the slip vectors i.e. the movement of the hanging wall. Red arrows show the direction of the long-term velocity vectors calculated in this study (in the fixed-Indian reference frame of Ader et al. (2012)). The dashed black lines show the boundaries between the different regions for which long-term velocities were calculated for. The thick black line shows the surface trace of the MHT and the grey lines show country borders.

From the coupling pattern, the uplift rates can be calculated and then compared with the current topography (Figure 2.5). The close similarity in map view is striking, including detailed features such as the embayment of the arc at 82°E, and the kink in the western end. As was inferred earlier from the colocation of the bulge of interseismic uplift with the front of the High Himalaya (Bilham, Larson, and Freymueller, 1997; Meade, 2010), this correlation suggests that some fraction of the interseismic geodetic strain, albeit small as discussed above, is actually anelastic and contributes to topographic uplift in the long run. The main control on uplift rate might be the geometry of the MHT, rather than the precipitation pattern, as also concluded by Godard, Lavé, and Cattin (2006). In fact, the building of the topography in the long term also probably result from ramp overthrusting (Pandey et al., 1995; Lavé and Avouac, 2001; Cattin and Avouac, 2000; Herman et al., 2010; Grandin et al., 2012). This mechanism cannot be assessed based on measurements of interseismic strain only, as if the ramp is within the locked domain it is undetectable. Only creeping patches, whether on the MHT or elsewhere, would contribute.

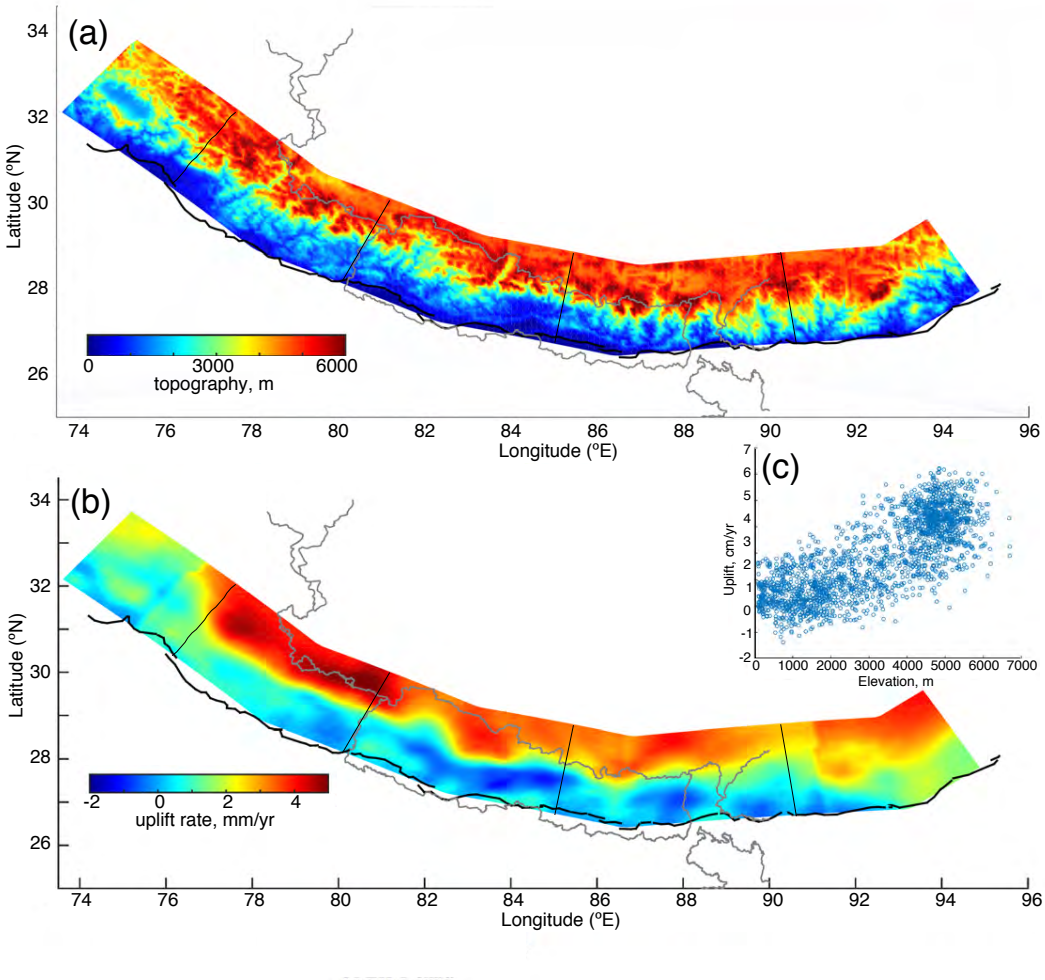

Figure 2.5: Comparison of topography with uplift rate. (a) Topography. Black lines show location of topographic and uplift rate profiles shown in Figure 2.S7. (b) Uplift rates calculated from the coupling pattern. (c) Correlation of topography with uplift rate, R value 0.78. Each dot represents an uplift rate from each patch used to model the fault (roughly 15x17 km) and the topography averaged over the same region.

In the Central Himalaya, where the coupling boundary is sharp, the uplift rate change is sharp, and this corresponds well with the steep topographic front. This downdip variation of coupling is possibly of thermal origin. The transition zone between locked and creeping coincides approximately with where the MHT intersects the 350°C isotherm (determined by Herman et al. (2010)). Slip is expected to be stable at higher temperature for quartzo-feldspathic rocks based on laboratory measurements (Blanpied, Lockner, and Byerlee, 1995). Fluids released from metamorphic reactions could also play a role in favouring the transition to aseismic creep (Avouac, 2003). In the east and the west, the coupling change occurs over a greater downdip distance, which reflects in the modeled uplift rate, and this is also seen in the topography. See Figure 2.S7 for cross sections of the modelled uplift rate and topography. The close correlation of interseismic uplift with topography is another indication that the coupling pattern is probably stationary through time.

Seismic moment build-up rate

The long-term velocities and coupling pattern can be used to calculate the seismic moment build-up rate. Here we adopt the conservative hypothesis that all of the interseismic surface strain is elastic. This can be seen in Figure 2.2c, with a most likely rate of $15.1 \pm 1.1 \times 10^{19}$ Nm/yr. This quantity is estimated from the area of the fault plane and the calculated slip on each patch. The standard deviation (shown as dashed black lines on Figure 2.2c) is estimated by Monte Carlo simulation of 10,000 different distributions of patch velocities, calculated from the best fitting patch velocity, the covariance matrix, and the chi squared fit.

2.5 Conclusions

All along the Himalayan arc the MHT appears to be fairly uniformly locked from the surface to beneath the front of the high range over a width of 100±20 km, except in the far west where it extends to about 150 km. We see only modest variations of the geometry of the lower edge of the locked zone, which also reflects in the seismicity and topography. We see no resolvable aseismic barriers that could affect seismic ruptures, so if the seismic activity of the Himalaya is segmented, the cause for the segmentation would have to be of another origin. We can imagine an earthquake nucleating at any point along the arc, and rupturing for a significant distance. In this context, zones of lower stress due to past earthquakes or geometric complexities would be the main factors contributing to the arrest of seismic ruptures along strike.

The amount of anelastic deformation in the interseismic period has to be small given the consistency of geodetic slip rate on the MHT calculated here, with range front velocities determined from geological studies; the creep rate at depth is transferred to the surface trace of the fault requiring interseismic deformation of the overhanging thrust sheet to be mostly recovered during slip events on the locked portion of the MHT. However, because of the correlation between interseismic uplift rates and the topography, the anelastic deformation cannot be null. From the general agreement between geodetic and geological rates, we find the fraction of anelastic deformation is up to 10 % at the 70 % confidence level.

The variations of the down-dip edge of the locked zone are consistent with geodesy, seismicity, and topography. Evidence for the stationarity of slip rates and interseismic coupling through time comes from three sources; 1) the correlation of geomorphic and GPS studies, 2) the correspondence of topography and uplift, and 3) the consistency of earthquake thrust vectors with GPS velocities. This study provides constraints on the rate of accumulation of seismic moment which needs to be released by transient slip events on the MHT. The results from this study can be used to constrain the probable location, frequency, and magnitude of large earthquakes in the Himalaya based on a slip budget approach. This analysis is left for a subsequent study.

Supporting Information for “Interseismic Coupling on the Main HimalayanThrust"

Contents

1. Tables 2.S1 to 2.S2.
2. Figures 2.S1 to 2.S7.

Additional Supporting Information (Files uploaded separately)

1. Dataset S1 - GPS Data used in the Inversion.
2. Dataset S2 - Electronic data for coupling map of Figure 1.
3. Dataset S3 - Electronic data for stress rate map of Figure 2b.

Introduction

Here we show extra figures relating to data, model set-up, resolution, and residuals.

Table 2.S1: Long term slip rates from geomorphic studies and modelled here

Lon	Slip Rate (cm/yr)	Uncertainty	Modelled Slip Rate (cm/yr)	Modelled Uncertainty	Reference
76.0	13.3	0.8	14.6	1.5	Thakur et al. (2014)
77.5	11.9	3.1	17.1	1.7	Wesnousky et al. (1999)
78.1	10.8	2.2	17.1	1.7	Parkash et al. (2011)
82 .0	19	6.0	19.3	1.2	Mugnier et al. (2003)
85.3	21	1.5	19.7	1.6	Lavé and Avouac (2000)
85.8	18.2	6	19.7	1.6	Bollinger et al. (2014)
90.3	20.8	8.8	17.4	1.2	Berthet et al. (2014)
92.5	23	6.2	20.2	2.0	Burgess et al. (2012)

Table 2.S2: Rotation Poles with respect to India for the Sikkim/Shillong and Bhutan/Assam Blocks of this study, and the Shillong and Assam Blocks in the study of Vernant et al. (2014).

Block	Lon	Lat	Rotation Rate	Study
Assam	88.1	26.6	-1.13	this study
Shillong	87.1	25.6	-0.62	this study
Assam	87.8	26.8	-1.13	Vernant et al. (2014)
Shillong	88.8	26.4	-1.15	Vernant et al. (2014)

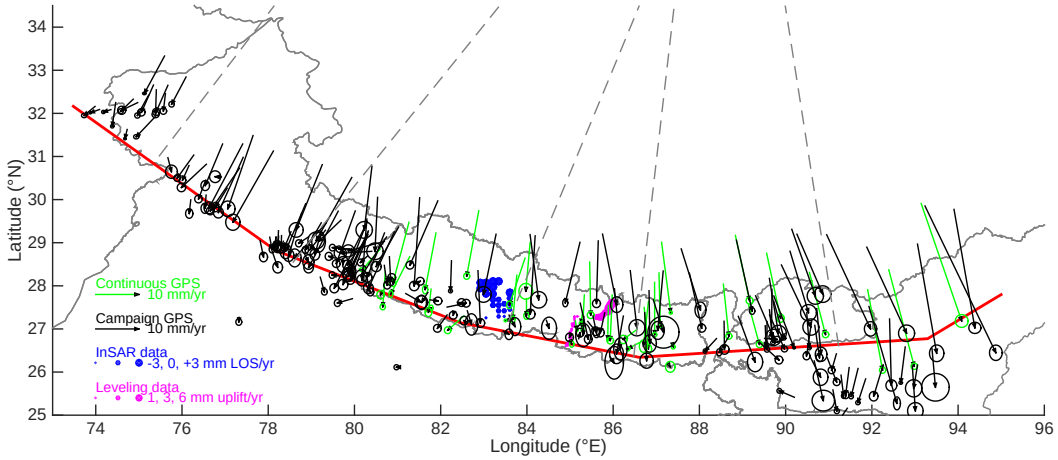

Figure 2.S1: Location of data used in the inversion. Arrows show velocities relative to India (as defined by Ader et al. (2012)) determined from continuous (green) and campaign (black) GPS data. Ellipses show the uncertainties at the 67% confidence level. The blue circles are InSAR data. The magenta circles are leveling data. The thick red line is the simplified geometry of the MHT used in the model. Country borders are marked in grey.

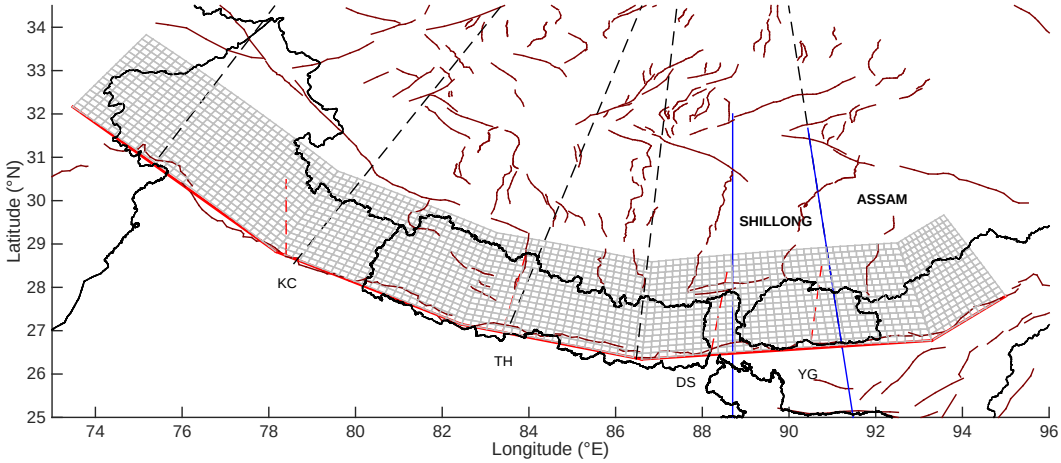

Figure 2.S2: The model setup. The red line shows the simplified surface trace of the fault, and the grid shows the discretization used in this model. The dashed black lines are the boundaries between different regions of uniform long term slip rate. The blue lines show the edges of the two blocks for which rotation poles are found. The red dashed lines show the rough location of major grabens. KC = Kaurik Changdu rift (Kundu et al., 2014). TH = Thakkola graben (Colchen, 1999). DS = Dingjie-Sehnza fault zone (Gan et al., 2007). YG = Yadong-Gulu rift (Gan et al., 2007). Thinner red/brown lines show faults from Styron, Taylor, and Okoronkwo (2010).

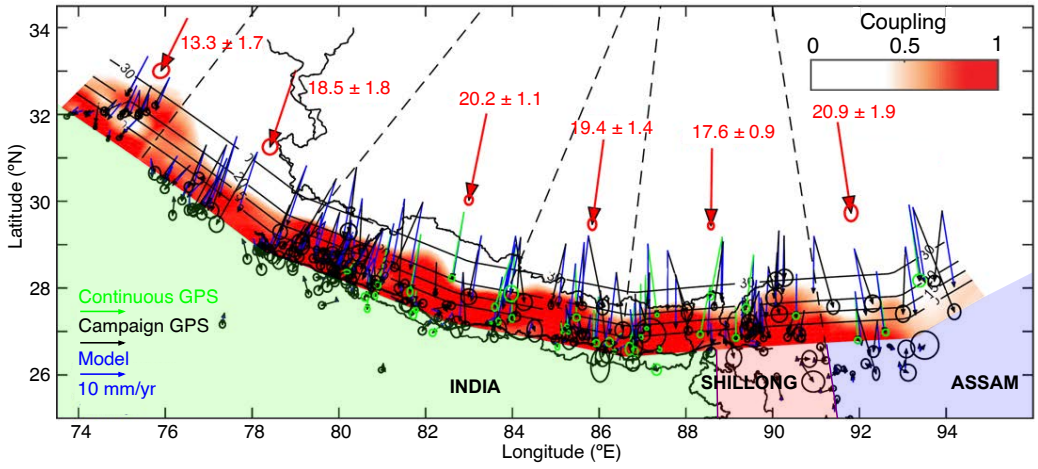

Figure 2.S3: Same as Figure 2.2, except with the poles of Vernant et al. (2014) imposed and not solved for.

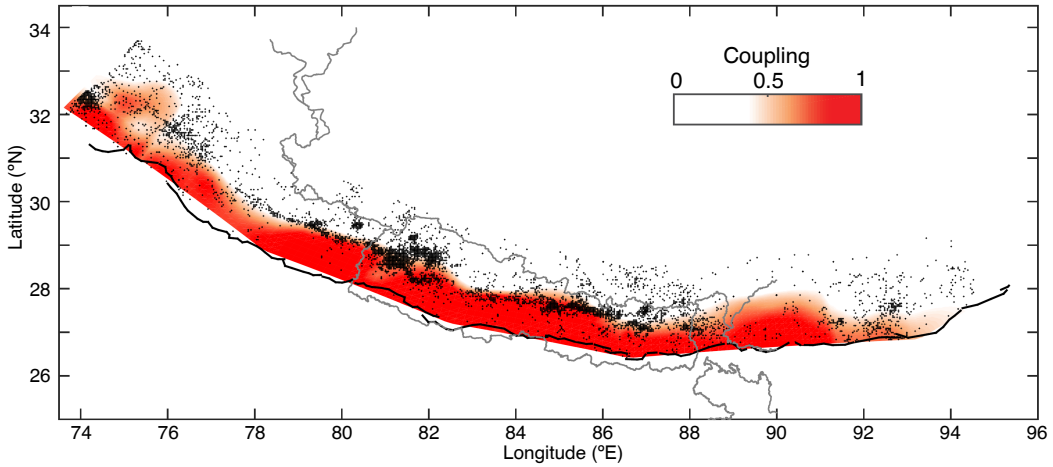

Figure 2.S4: Same as Figure 2.1a, except with uniform weighting of the Laplacian. The coupling model is thus not regulated by the seismicity.

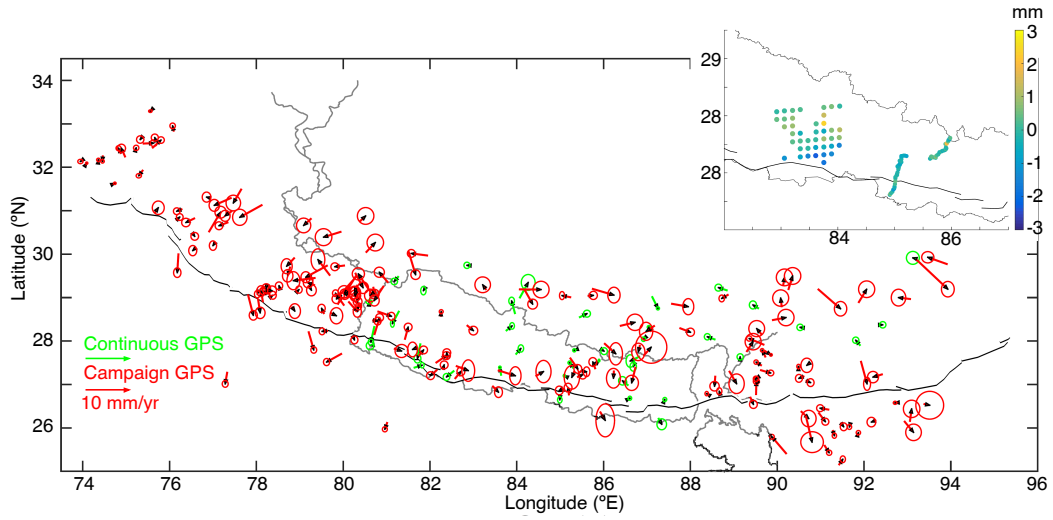

Figure 2.S5: Residuals to the GPS data, with uncertainy ellipses. Campaign measurements are in red, and continuous measurements in green. The inset shows the residuals of the InSAR and leveling data.

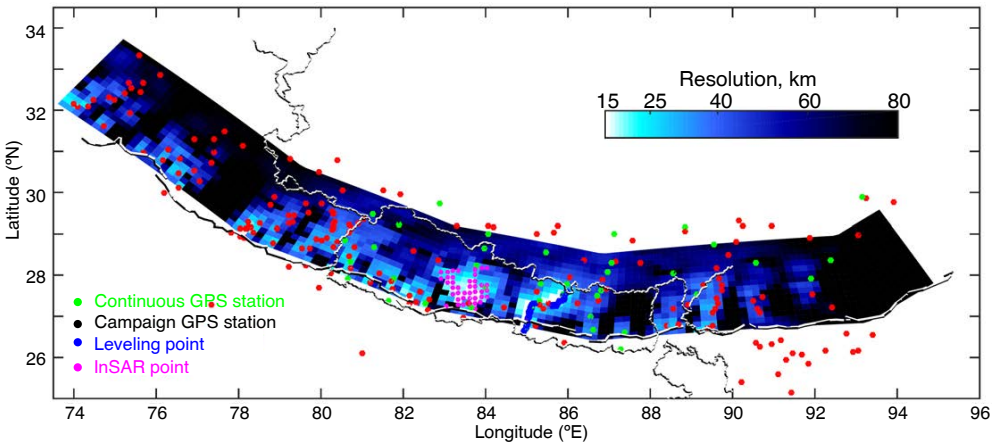

Figure 2.S6: Resolution on each patch of the fault. The resolution here is the characteristic size of the smallest inhomogeneities of coupling which could in principle be resolved, given the spatial distribution and uncertainties of the measurements. The figure is saturated at a resolution of 80 km, as above this value we assume there is no resolution on the corresponding patch, and so slip on this patch is just determined by slip on the neighbouring patches. See Ader et al. (2012) for details of the calculation. The location of data points used to find the resolution are also shown.

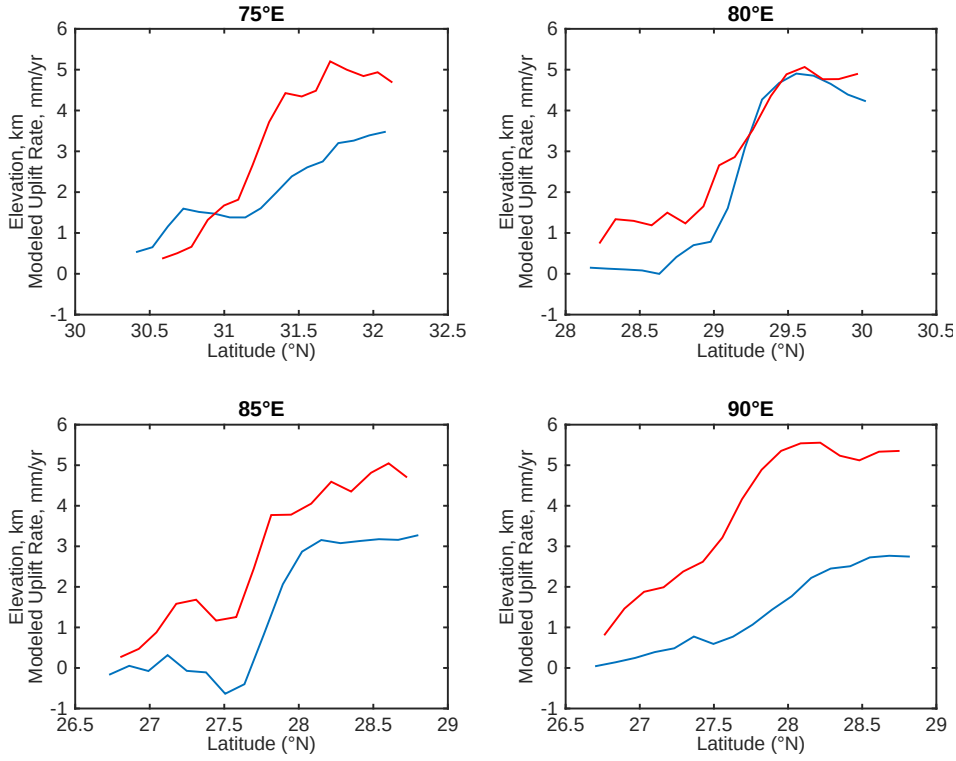

Figure 2.S7: Smoothed elevation (red) compared with modelled uplift rates (blue) at different longitudes. Profile locations are shown in Figure 2.5 of the main text.

Chapter 3

MILLENARY M_W > 9.0 EARTHQUAKES REQUIRED BY GEODETIC STRAIN IN THE HIMALAYA

(Published as “Millenary M_w >9.0 earthquakes required by geodetic strain in the Himalaya" by V. L. Stevens and J. P. Avouac, Geophysical Research Letters, 2016)

ABSTRACT

The Himalayan arc produced the largest known continental earthquake, the M_w~8.7 Assam earthquake of 1950, but how frequently and where else in the Himalaya such large magnitude earthquakes occur is not known. Paleoseismic evidence for co-seismic ruptures at the front of the Himalaya with 15 to 30 m of slip suggest even larger events in medieval times, but this inference is debated. Here we estimate the frequency and magnitude of the largest earthquake in the Himalaya needed so that the moment released by seismicity balances the deficit of moment derived from measurements of geodetic strain. Assuming one third of the moment build-up is released aseismically and the earthquakes roughly follow a Gutenberg-Richter distribution, we find that $M_w > 9.0$ events are needed with a confidence level of at least 60% and must return approximately once per 800 years on average.

3.1 Introduction

Subduction megathrust faults are known to produce the largest earthquakes on Earth, which can reach a moment magnitude (M_w) well above 9.0. Whether continental megathrust faults, such as the Main Himalayan Thrust (MHT) along which the Himalayan wedge is thrust over India, can host such large earthquakes is less clear. Geodetic measurements of interseismic strain indicate that the MHT is nearly completely locked over a ~120 km width all along the arc (Ader et al., 2012; Bilham, Larson, and Freymueller, 1997; Mukul et al., 2010; Schiffman et al., 2013; Stevens and Avouac, 2015) (Figure 3.1A). Locking results in a moment deficit accumulating at a rate of $15.1 \pm 1.1 \times 10^{19}$ Nm/yr. The interseismic locking pattern is probably stationary as indicated from the correlation with topography. The 3500 m elevation contour line outlines the downdip edge of the locked fault zone (Figure 3.1B) and also bounds the northern extent of thrust earthquakes (Avouac, 2003; Bollinger et al., 2004b). The along-strike uniform locking, despite different segments being in different stages of the seismic cycle, also suggests that temporal variations are small.

The consistency of geological slip rates with geodetic shortening rates (Stevens and Avouac, 2015) requires that transient slip events on the locked portion of the MHT must add up to compensate interseismic slip deficit. This is observed in eastern Nepal where trenches have revealed five to seven >12 m slip events over the last 3600 yr, most probably associated with large earthquakes including an M_w8.4 in 1934 and a similar earthquake in 1255 (Bollinger et al., 2014). The slip budget seems to close locally over this time period (Bollinger et al., 2014). Paleoseismic studies have revealed even larger (> 15 m) slip events around 1100 AD at distant sites (Kumar et al., 2010; Lavé et al., 2005; Upreti et al., 2000). Assuming they are due to the same earthquake, the rupture length would have exceeded 700 km, about twice as long as in 1934. Similarly, a very large earthquake may have ruptured the Himalayan front around 1400 AD in the Kumaon-Garwal Himalaya (Kumar et al., 2006) (Figure 3.1A). Large seismic slip events are documented also in Bhutan (Berthet et al., 2014), although this area is devoid of significant recorded large earthquakes. Paleoseismic studies thus raise the possibility of $M_w > 9.0$ earthquakes.

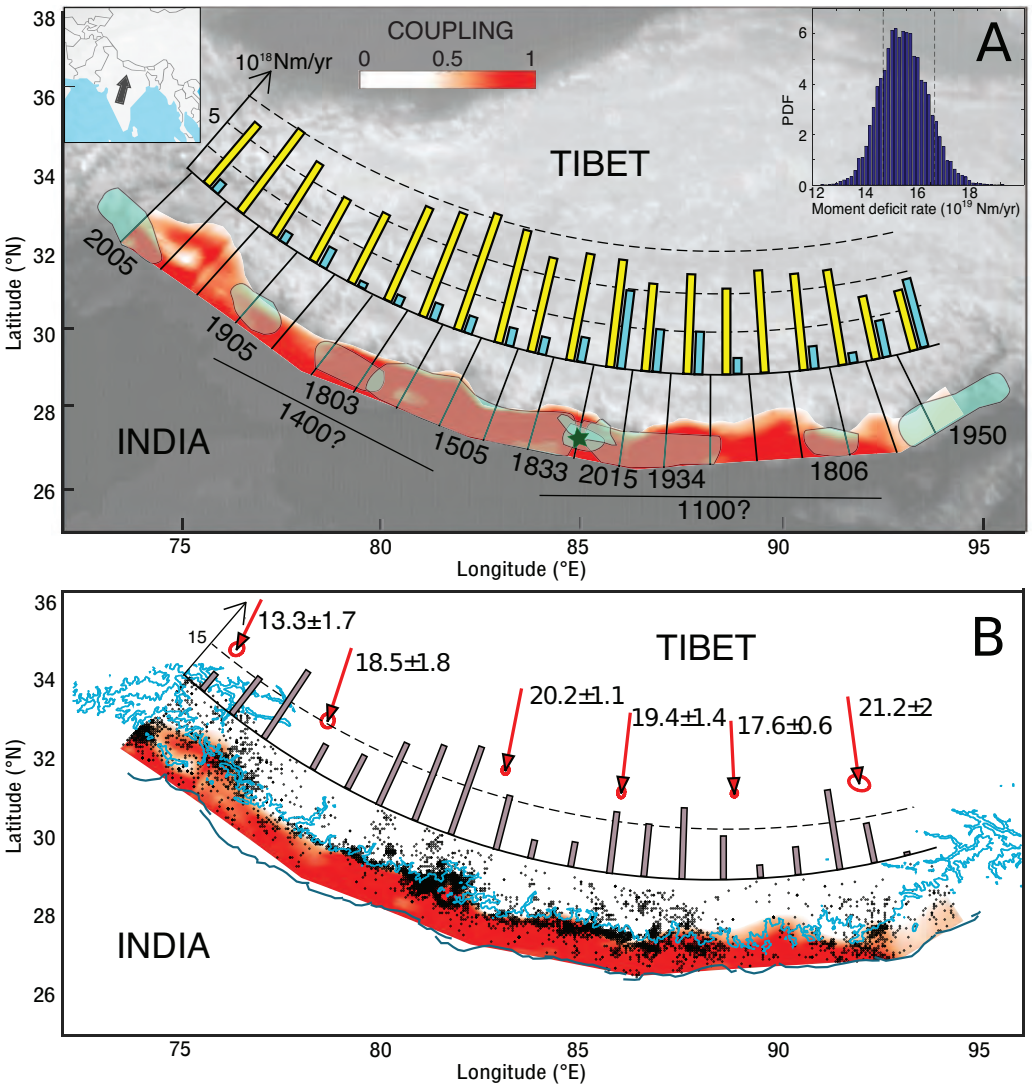

Figure 3.1: Interseismic coupling and moment build-up on the Main Himalayan Thrust. a) The pattern of coupling (Stevens and Avouac, 2015) is shown in red, overlain by the rough locations of earthquakes M_w7.5-8 for the past 200 years and ≥ 8 for the past 500 years (Kumar et al., 2010; Galetzka et al., 2015), which are used in calculating the rate of seismic moment release (light blue bars). The approximate extent of surface ruptures of two potential major earthquakes, dated to ~1400AD and ~1100AD from paleoseismic studies, are also shown. The probability distribution function (pdf) in the inset shows the seismic moment build-up calculated from the coupling model, and the yellow bars show its distribution along the strike of the arc. b) Same coupling pattern, now with the surface trace of the Main HimalayanThrust (Styron, Taylor, and Okoronkwo, 2010) in dark blue and the 3500 m elevation contour line in light blue. The 3500 m contour seems to mark the downdip extent of the locked fault zone. The MHT appears locked from the surface, where is emerges along the front of the sub-Himalaya, following the trace of the Main Himalayan Thrust to beneath the front of the high Himalaya. Red arrows show convergence across the range in mm/yr. Black dots show seismicity from the NSC and NEIC catalogs (Ader et al., 2012; Stevens and Avouac, 2015). The grey bars show the distribution of the number of earthquakes above 4.9 (the magnitude of completeness) of the declustered NEIC catalog (see Supplementary Information for details).

We confirm Bilham, Gaur and Molnar's (Bilham, Gaur, and Molnar, 2001) inference that the moment deficit accumulating in the interseismic period outweighs the moment released by the known seismicity. $M_w < 5.5$ earthquakes from local monitoring in the interseismic period release < 1% of the moment deficit due to locking of the MHT (Figure 3.2A). $M_w \leq 7.8$ earthquakes reported in the NEIC catalog (http://neic.usgs.gov) released less than 10% of the interseismic moment deficit over the past 30 years covered by this catalog. Historical earthquakes (Tables 3.S1, 3.S2 in Supplementary Information), which reach to $M_w 8.7$, still fall short of balancing interseimic locking. Even if we extend the catalog up to $M_w 9.0$ events to account for the paleoseismic evidence, seismic slip still falls short of balancing the interseismic deficit of slip, as shown from the gap between the seismic moment build-up and release rate from earthquakes (Figure 3.2A). The imbalance can also been seen from the comparison of moment release to build-up through time over the past 1000 years (Figure 3.S5).

Balancing the slip budget seems to require more frequent $M_w 9.0$ events than we assumed (1 in 1000 years), or even larger earthquakes. This analysis ignores the role of aseismic slip and the moment accounted for by undetected earthquakes. These factors need to be taken into account to assess quantitatively the slip budget balance and the probability of large events. We first describe the method used, and then go on to discuss the results.

3.2 Method and Data

We assess the magnitude and return period of the largest earthquake needed to balance the slip budget at the scale of the whole Himalayan arc. We assume that fault slip above the brittle-ductile transition, as indicated by the depth distribution of earthquakes, is entirely seismic, and that the seismic slip events must add up to match the long term slip rate on the fault (Brune, 1968; Molnar, 1979). We include the contribution of aftershocks and transient aseismic slip in the slip budget. This approach has been applied recently to the Sunda Megathrust and the Longitudinal Valley fault in Taiwan. In these examples, the seismicity known from historical accounts and instrumental records and afterslip balance the interseismic deficit of moment (Avouac, 2015).

No spontaneous aseismic transient has yet been observed in the Himalaya despite nearly 20 years of monitoring with tectonic geodesy. Therefore we deem the contribution of spontaneous transients small, though we cannot exclude the possibility of rare transients as observed on some subduction megathrusts (Radiguet et al., 2012;

Wallace and Beavan, 2006). More importantly, aseismic slip following large earthquakes, so-called afterslip, could contribute significantly to the budget. Afterslip over the year following the M_w7.6 2005 Kashmir earthquake released possibly as much as 56±19% of the coseismic moment (Jouanne et al., 2011). Afterslip in the first two months following the M_w7.8. 2015 Gorkha earthquake released no more than 10% of the co-seismic moment (Galetzka et al., 2015).

Our calculations use the probability distribution function (pdf) of the rate of accumulation of the moment deficit in the interseismic period (inset of Figure 3.1a). Errors outside the formal errors in the seismic moment build-up rate are considered, and would all lower the rate of build-up. Firstly, if viscoelastic effects were significant, the elastic back-slip model used would overestimate the build-up rate (Wang, Hu, and He, 2012; Li et al., 2015), though since there have not been large earthquakes along the MHT recently, this effect is not likely to be significant. In Northern Chile, the viscoelastic effect was found to cause a bias of 12% (Li, pers. comm.), and while the tectonic setting is different here, we consider the bias to be $<$ 20%. The refined evaluation of this source of uncertainties is left to future studies. Secondly, unresolved creeping patches on the fault would also lower the build-up rate. However, to be unresolved these patches would have to be small, and where we have the densest GPS we do not see any, suggesting there may be none at all. This suggests creeping patches could lower build-up rate by up to 10%.
From now on we assume that the moment released by seismic slip events is augmented by 50% due to a combination of aseismic afterslip and errors in seismic moment build-up rate, discussed above. We take this high value of 50% as we want to use an upper estimate of the amount that would be released aseismically, so that our final result is a conservative value, meaning the largest earthquake would have to be at least that big. Additionally, we first use the truncated Gutenberg-Richter (GR) law (California Earthquake Probabilities, 1995; Field, Jackson, and Dolan, 1999), so we assume that the seismicity follows the (GR) law up to the largest earthquake in the distribution (Method 1). Unlike other studies, we consider the effect of aftershocks produced by the larger earthquakes. If a very large earthquake has not occurred in the instrumental record (as is the case in the Himalaya, where the record is 39 years long) we will be missing almost all of its aftershocks. These would change the average rate of smaller earthquakes, and so shift the whole seismic curve upward. Excluding these aftershocks would lead to an overestimation in the maximum magnitude earthquake using the truncated GR method. Here we

simulate missing aftershocks from the historical and paleoseismic earthquakes. We do this simply by using Bath's law for the largest aftershock (1.2 below the mainshock) and then assuming that the smaller aftershocks follow a GR distribution with b-value equal to the original earthquake catalog. The results of this can be seen in the green and red lines of Figure 3.2B.

For Method 1 we use Monte Carlo analysis and simulate 40 million different scenarios taking into account the uncertainties on the various quantities entering the calculation (the earthquake magnitude-frequency data themselves, the b-value, the size of the largest aftershock, and the rate of moment accumulation). We extrapolate the frequency-magnitude relationship derived from the earthquake datasets to the magnitude needed to balance the slip budget (blue line in Figure 3.2B). We thus get the magnitude-frequency of the expected maximum earthquake.

Method 1 is incorrect if the frequency-magnitude GR distribution defined by the smaller earthquakes cannot be extrapolated to the largest event in the distribution, as is assumed in the characteristic earthquake model (Schwartz and Coppersmith, 1984). It is indeed possible that the very large earthquakes, which rupture entirely the width of the seismogenic zone, do not follow the same statistics as the smaller events. We therefore make another calculation without this assumption (Method 2). We determine the 2-D pdf of the magnitude (M_w) and frequency (1/T, where T is the long term averaged return period) of the largest earthquake by multiplying the probability of balancing the slip budget, P1, and the probability of observing this largest earthquake over a given period of time, P2. P2 is calculated assuming that independent earthquakes follow a Poisson process and based on the largest known earthquake over the various periods of time covered by the earthquake catalogs. More details of the method and results obtained with different assumptions are given in the Supporting Information.

The data we analyze comes from different earthquakes datasets as detailed in the Supporting Information. One is the seismicity of Nepal, which has been well monitored from a local network operated by the National Seismic Centre (NSC) Nepal (Ader et al., 2012; Pandey et al., 1999). Another catalogue is the 1976-2015 NEIC catalog which includes the M_w7.6 earthquake of 2005 and the M_w7.8 earthquake of 2015. The NEIC catalogue yields a higher seismicity rate than the NSC catalogue in the 4.5-5.5 magnitude range, where both catalogues are complete, due mostly to the contribution of the aftershocks of the 2005 and 2015 events. We next estimated the rate of $M_w > 7.5$, $M_w > 8.0$, $M_w > 8.5$, and $M_w > 9.0$ based on the historical catalog, and take their aftershocks into account (Tables 3.S1 and 3.S2).

3.3 Results and Discussion

In Method 1 the datasets can be used independently or jointly to calculate the pdf of the magnitude and return period of the largest earthquake needed to close the slip budget, consistent with the GR law. Figure 3.S2 shows that whatever catalog is used, the maximum earthquake would need to reach between M_w8.5 and M_w10. A M_w10 is unphysical, as a single rupture of the whole Himalayan arc (2500 km long), assuming a standard scaling law (Schwartz and Coppersmith, 1984) which implies an average slip of 50 m, would reach 'only' M_w9.7.

Figure 3.3a shows the 2-D pdf of the magnitude and frequency of the maximum earthquake (colored contour lines) as well as the marginal cumulative probability of the largest earthquake exceeding a given magnitude, and the marginal cumulative probability of its frequency being lower than a given value (grey shaded cumulative density functions along the x and y axis). The probability of closing the slip budget with the maximum event not exceeding M_w8.5 is extremely small ($5.7\text{x}10^{-5}$%). The probability of closing the slip budget with the largest earthquake not exceeding M_w9.0 is only about 34%. The probability of the return period of the largest event being more than 1000 yr (corresponding to an annual frequency of less than 10^{-3}) is 66%. This analysis implies $M_w > 9$ events with a >1000 yr return period at the 67% confidence level.

With Method 2, assuming earthquakes follow a Poisson distribution, the probability of closing the slip budget with the largest earthquake not exceeding M_w9.0 is about 37% (Figure 3.3B). The probability of observing the largest event over 1000 years is now 45%. Both methods thus indicate that the largest earthquake in the Himalaya must exceed M_w9.0 at > 63% confidence level. In both cases, the average return period of the largest earthquake is estimated to be >800 yr at the whole-arc scale.

Some studies have found suggestions of earthquake supercycles (e.g. Sieh et al. (2008)), though in the Himalaya we have not seen earthquake clustering in the past 500 years. To balance the moment with magnitude no larger than 8.5, we would need a magnitude 8.5 roughly once every 120 years. So, if only 2 occurred in the past 500 years, as the historical catalogue suggests, this quiet period would need to be compensated by periods of clustered events, for example a 500 year period with 6 events. We give this example although this possibility seems improbable to us in view of the paleoseismic data.

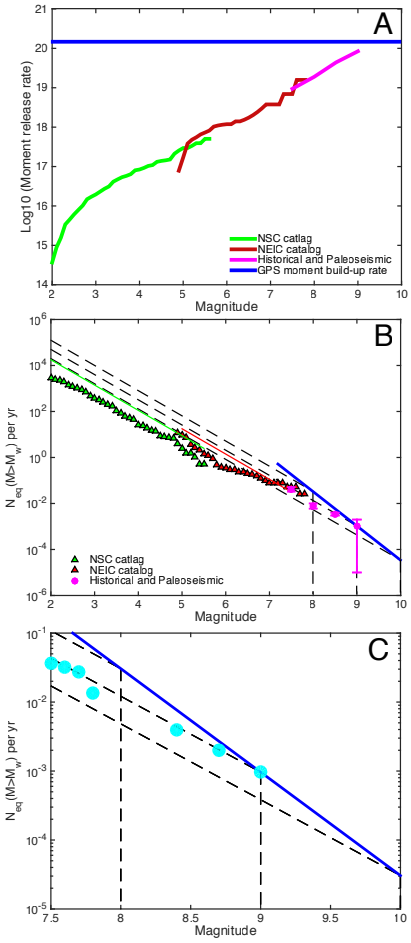

Figure 3.2: Comparison of interseismic moment build-up and seismic moment released by known earthquakes. a) Plot showing moment release rates for different sized earthquakes. Blue line shows the moment build-up rate calculated from the coupling pattern - the width of the line shows the errors. The curves showing the moment released by earthquakes are cumulative (all earthquake with magnitude less than the abscissa value are added). The catalog of historical and palesoseismic events is listed in Table 3.S1. The plot assumes one M_w9 event in the past 1000 years. With these assumptions, seismicity does not balance locking of the MHT in the interseismic period and to do so it would need to extend up to a magnitude more than M_w9. b) Gutenberg-Richter plot with the same assumptions. The blue line shows the magnitude-recurrence time relationship of earthquakes that would take up the seismic moment. The black dashed lines show (top to bottom) where the seismicity should lie given an earthquake with maximum magnitude 8, 9, or 10 respectively, assuming it follows the GR law with a b-value of 1.1. The pink markers show the estimated long-term average seismicity rates, and associated uncertainties (error bars show one sigma errors), by grouping magnitudes into bins of 0.5-magnitude unit range (Table 3.S2). This allows for a better estimation of uncertainties. c) Gutenberg-Richter plot of historical earthquakes (Table 3.S1) compared with the frequency-magnitude of the largest event needed to balance the slip budget.

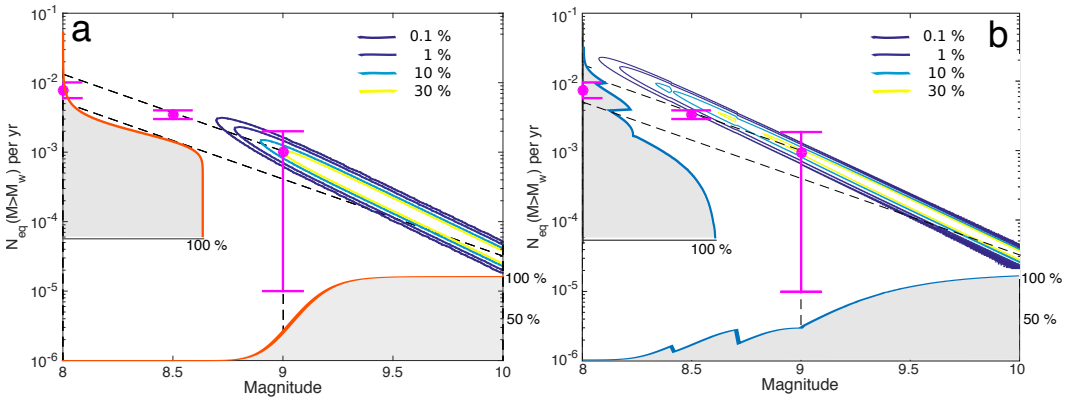

Figure 3.3: Probability distribution functions of the frequency-magnitude of the largest earthquake need to balance the slip budget. a) Method 1. Colored contour lines show the 2-D pdf of the magnitude and frequency of the maximum earthquake. Grey shaded cumulative density functions along the x and y-axes represent, respectively, the marginal cumulative probability of the largest earthquake exceeding a given magnitude, and the cumulative marginal probability of its frequency being lower than a given value. Pink markers show the binned magnitudes as in Figure 3.2B. b) Method 2. As in A, the shaded curves show the probability an earthquake of that magnitude, or recurrence time, could occur and take up the needed seismic-moment. The probability drops after each of the magnitudes of the large earthquakes because above that magnitude we have seen fewer earthquakes and they are short of balancing interseismic moment deficit. The drop after magnitude 9 is smaller because the recurrence time needed for a magnitude 9 to close the slip budget is closer to the observation period, 1000 years, so it is much more likely that we could have missed an earthquake with this recurrence time. Blue markers showed the unbinned magnitudes, as in Figure 3.2C.

3.4 Conclusion

We conclude that millenary $M_w > 9.0$ earthquakes are very likely, confirming inference from paleoseismic studies (Kumar et al., 2010; Lavé et al., 2005; Upreti et al., 2000). To arrive at this result we have used instrumental and historical/paleoseismic earthquake catalogs, along with the moment build-up rate derived from geodetic data. An alternative, less likely, scenario is that the rate of M_w8 to 8.5 earthquakes is much higher than estimated from historical data. In both cases, our analysis implies a high level of seismic hazard along most of the Himalayan arc.

Supporting Information for Supporting Information for "Millenary $M_w > 9$ earthquakes required by geodetic strain in the Himalaya"

Contents

1. Text 3.S1 to 3.S2.
2. Figures 3.S1 to 3.S5.
3. Tables 3.S1 to 3.S2
4. References

Introduction

Here we give more details of the methods and data used in the maintext. Figures 3.S1 to 3.S2 help clarify the method while figures 3.S3 and 3.S4 show the results of changing assumptions. Figure 3.S5 shows a comparison of moment build-up and release through time. Tables 3.S1 and 3.S2 show original and binned data respectively for the historical and paleoseismic earthquakes.

Method 1

We use the instrumental, historical, and paleoseismic earthquakes catalogs, along with the total moment build-up rate each year, to find the maximum likely earthquake size. In this first method, we assume earthquakes follow a GR distribution,

$$log_{10}N(M_w) = a - bM_w \tag{3.1}$$

where a and b are constants, M_w is the magnitude, and N is the number of earthquakes above magnitude M_w. a is the number of earthquakes above $M_w = 0$, and can be thought of as the productivity. We also assume that the b-value is 1.1±0.1, the largest aftershock is 1.2±0.1 below the mainshock, and the seismic moment build-up is 15.1±1.1 x10^{19} Nm/yr.

The total moment line is found from the integration of the number and magnitude of earthquakes, assuming the GR law as above, and the relation between moment (M_o) and magnitude:

$$M_\circ = 10^{\alpha(M_w+\beta)} \tag{3.2}$$

where $\alpha = 2/3$ and $\beta = 10.7$.

$$N_\circ = 10^{\alpha} - 10^{(a-bM_w)} \tag{3.3}$$

where $N_\circ$ is the number of earthquakes below magnitude M_w.

$$Total \quad moment \quad release = \int_{-\infty}^{M_w} M_\circ(M'_w) N_\circ(M'_w) dM'_w \tag{3.4}$$

So we get

$$a = log_{10} \frac{M_\circ}{10^{(1.5-b)M_w} - 1} - log10(3) - 9 - log10(b) - bM_w. \tag{3.5}$$

Since we have estimates of $M_\circ$ and b we can use this equation to find the relation between M_w and the recurrence time, if M_w were to be the maximum sized earthquake.

Data

Instrumental Seismicity

We use the NSC catalog (from 1995 to 2001), which covers five years of microseismicity in Nepal, and contains 12,201 earthquakes with magnitudes 0.3 to 5.5. These magnitudes are reported in local magnitudes (M_L), and we use the method of Ader et al. (2012) who used a subset of events reported also in the CMT catalog, to convert into moment magnitude (M_w):

$$M_w^{NSC} = 0.84 M_L^{NSC} + 0.21. \tag{3.6}$$

Since this catalog contains only earthquakes recorded in Nepal, we scale up by a factor of 3, assuming the microseismicity is consistent along the arc.

We use the NEIC catalog between 1976 and August 2015. We take earthquakes within 100 km of the surface trace of the Main Himalayan Thrust. To account for the fact that some of these earthquakes are not on the MHT, we use the CMT catalog covering the same area to find the percentage of the total that are thrust events. We find that 75% are thrusts, so we scale the NEIC catalog by 0.75. Large earthquakes are reported as M_w in the NEIC catalog; however for those reported as m_b we use (Scordilis, 2006)

$$M_w^{NEIC} = 0.85M = m_b^{NEIC} + 1.03. \quad (3.7)$$

The catalog we use then contains 1,465 earthquakes between magnitudes 4.9 and 7.8. Figure 3.2B shows lateral variations of the seismicity rate derived from the NEIC catalog from 1976 to present after declustering. The earthquakes were declustered using ZMAP (Wiemer, 2001) and Reasenberg's method (Reasenberg, 1985) with the optimum parameters obtained by Ader and Avouac for this catalog (Ader and Avouac, 2013). The magnitude of completeness is estimated to be M_w4.9.

Historical and Paleo- Earthquakes

The historical earthquakes considered in this study are listed in Table 3.S1. This list is based on the historical catalogs of Ambraseys and Douglas (2004), Bilham (2004), and Pant (2002). We revised the magnitudes of the 1934 Bihar Nepal and 1950 Assam earthquakes to M_w 8.4 and 8.7, respectively, based on the moment determined from the long period seismic waves (Chen and Molnar, 1977; Molnar, 1984) assuming a dip angle of 5^o-10^o consistent with the estimated dip angle of the seismogenic portion of the MHT. The magnitudes of the 1344 and 1505 earthquakes are debated. We have assigned M_w8.4 to the 1505 event. Some authors argue that this earthquake was in fact more minor (Rajendran et al., 2013) and that the major event in western Nepal is actually the 1344 earthquake (Mugnier et al., 2011). This earthquake could match the paleoseismic event in the Kumaon-Garwal Himlaya dated to 1400 AD (Kumar et al., 2006). A recent study (Schwanghart et al., 2016) confirms the probability of significant earthquakes in 1110, 1255, and 1344 from catastrophic valley infilling events corresponding to these dates.

Based on Table 3.S1 we constituted a possible model of the long-term averaged rate of large earthquakes in the Himalaya (Table 3.S2). For earthquakes $\geq M_w$9, there are two earthquakes which could be in this range - the 1100 AD and 1400 AD earthquakes (see Table 3.S1); however these could both be below M_w9. So we choose the range 0-2 earthquakes $\geq M_w$9 in the past 1000 years to be the 1σ uncertainties.

For earthquakes $\geq M_w$8.5 we consider the two above, 1100 AD and 1400 AD earthquakes, which have a larger certainty of being above 8.5 than 9. We also consider the 1255 and 1950 earthquakes, though we are less certain if the 1255 earthquake

Table 3.S1: Earthquakes above magnitude 7.5 for the past 1000 years from paleoseismic, historical and instrumental catalogs.

Date	Magnitude	Location	Reference
1100	> 8.5	Eastern Himalaya	Lavé et al. (2005) and Kumar et al. (2010)
1255	8.0-8.5	Nepal	Sapkota et al. (2013)
1344	> 8.0	Nepal	Mugnier et al. (2013)
1400	> 8.5	Western Himalaya	Kumar et al. (2006)
1505	8.2	Western Nepal	Ambraseys and Douglas (2004)
1555	7.6	Kashmir	Ambraseys and Douglas (2004)
1720	7.5	N Uttar-Pradesh	Ambraseys and Douglas (2004)
1803	7.5	Garwhal	Ambraseys and Douglas (2004)
1806	7.7	Samye	Ambraseys and Douglas (2004)
1833	7.7	Nepal	Ambraseys and Douglas (2004)
1905	7.7	Kangra	Ambraseys and Douglas (2004)
1934	8.4	Bihar-Nepal	Chen and Molnar (1977) and Bilham (2004)
1950	8.7	Assam	Chen and Molnar (1977) and Bilham (2004)
2005	7.6	Kashmir	Avouac et al. (2006)
2015	7.8	Gorha-Nepal	Galetzka et al. (2015)

Table 3.S2: Proposed rate of large earthquakes estimated based on the data of Table 3.S1. Range of number of earthquakes at the 1-σ confidence level. For magnitude 7.5, we use the past 200 years of data, and scale up to 1000 years.

Magnitude	Number per 1000 years
$\geq$ 9.0	0-2
$\geq$ 8.5	3-4
$\geq$ 8.0	6-9
$\geq$ 7.5	33-50

was over magnitude 8.5, so we assign the 1σ range as 3-4 in the past 1000 years.

For earthquakes $\geq$ M_w8, we have the four potentially above 8.5 and the 1505 and 1934 events. We consider these six events to be a lower bound on the 1σ uncertainty, but we may be missing some, for example if the 1100 and 1400 earthquakes were actually two earthquakes of around 8 instead of nine, so we consider 9 as an upper 1σ bound.

For the earthquakes in the range M_w7.5-8, we used only the past 220 years of data (with the oldest earthquake being the 1803 Garwhal earthquake). This is because for these smaller earthquakes, the historical record deteriorates more quickly than

for the larger earthquakes as the shaking created is lesser and over a smaller area, so may more easily be missed. We then assume a similar rate of earthquakes for the past 220 years as for the past 1000 years. There have seen six recorded earthquakes of size M_w7.5-8 in the past 220 years (Table 3.S1). We take this as the 1σ lower bound, and assuming perhaps at least three missed earthquakes in this size range, take nine as the 1σ upper bound, so there is a 68% chance that there were between six and nine earthquakes in this magnitude range. The data used are summarized in Table 3.S2.

b-value and moment released by aftershocks

The b-value is used in calculating the slope of the line that takes up the seismic moment buildup, in simulating the aftershocks and in calculating the equivalent a value for the pieces of data. The latter is the most affected by the uncertainty in the b-value.

We find the b-value using the NSC catalog. We use the maximum likelihood method (Aki, 1965) to find the b-value, after choosing Mc (the lower cutoff value) using a bootstrap method, implemented in ZMAP (Wiemer, 2001). We find M_c = 3.2 and b = 1.1±0.04. We increase the formal uncertainty on the b-value to 1.1±0.1, as the NSC catalog only contains one third of the arc and only contains magnitudes up to 5.5 so the uncertainty may be more than the actual value obtained from the NSC catalog alone.

We are missing aftershocks of large earthquakes in the instrumental catalogs, as there have been no great (> M_w8) earthquakes since instrumental records began. We simulate aftershocks simply by assuming they follow a GR distribution with b-value 1.1±0.1, and that they follow Bath's law, with the largest aftershock 1.2±0.1 below the mainshock. For example, every time we have a magnitude 8 in the record, we assume an aftershock sequence with largest aftershock 6.8, with smaller earthquakes with frequency in accordance with GR. If the magnitude 8 occurred once every 100 years, this aftershock sequence would also occur every 100 years. In this way, we add missing aftershocks to the current catalogue. We add missing aftershocks for magnitudes 7.5, 8, 8.5, and 9. Adding aftershocks increases uncertainties due to b-value uncertainty and uncertainty in magnitude-frequency relations of the larger earthquakes. The addition of the aftershocks does not change the maximum

predicted earthquake size significantly, but it shows that the full earthquake catalog may follow more closely the GR law.

We can compare our aftershock model with aftershocks seen elsewhere. For the Gorkha 2015 earthquake, the first aftershock sequence had the largest aftershock 1.1 below the mainshock, whilst the second larger earthquake was only 0.5 below. Using the same method as described above, we find the b-value for the Gorkha aftershock sequence to be 1.08. For the Kashmir 2005 earthquake, the largest aftershock was 1.2 below the mainshock.

Finding the Maximum Earthquake

Instrumental earthquakes

If we use the NSC catalog, by simply extending the line using the b value found to the line that takes up the maximum moment, we find the results would be very high (M_w10.4) as we are missing aftershocks. If we add aftershocks it becomes M_w9.8. There are large uncertainties on this because of the large uncertainties in the number of aftershocks and b value uncertainties have the largest effect for extending smallest earthquakes. The answer gives us a magnitude of between 8.5 and 10.5 with 60% probability.
We can do the same for the NEIC catalog, which gives a magnitude 9.1 without aftershocks and 9 with. The aftershocks here have less of an affect here because the earthquakes are larger, so there will be fewer added earthquakes of this size.

Larger earthquakes

We then look at four points: the average recurrence times seen of magnitudes 7.5, 8, 8.5 and 9, which is discussed in the data section. We use Monte Carlo analysis using b = 1.1±0.1, Baths Law = 1.2±0.2, the earthquake recurrence time data in Table 3.S2 and a seismic moment buildup rate of 15.1±1x10^{19} Nm/yr. We run 40 million simulations to get a probability density function (pdf) of the probable maximum earthquake, and its recurrence time, predicted by each point (shown in Figure 3.S1).

Afterslip

Afterslip is a large unknown in the model. Aside from the Gorkha 2015 and Kashmir 2005 earthquakes (afterslip respectively ~10% and ~ 56% as mentioned in the

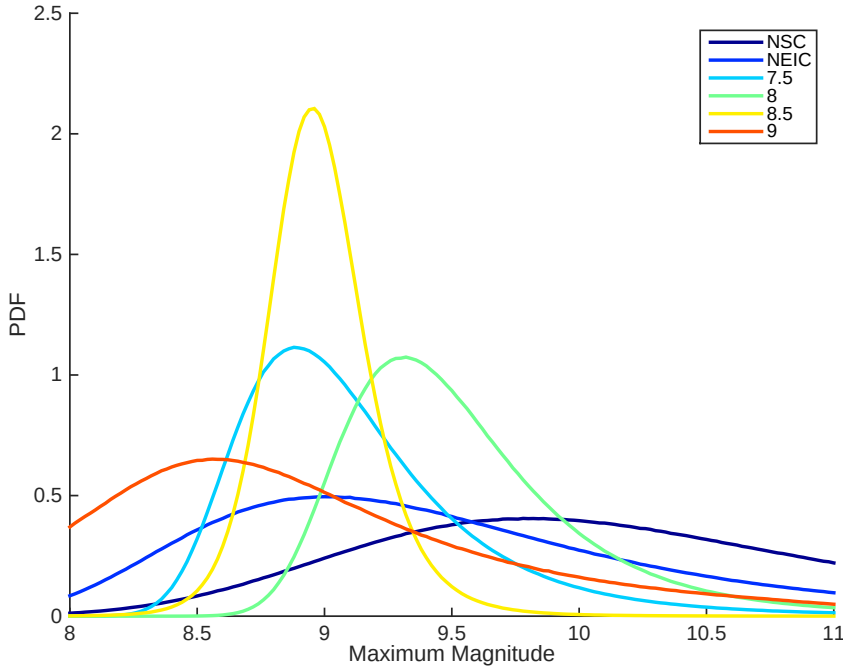

Figure 3.S1: All data sets used separately to predict the maximum moment.

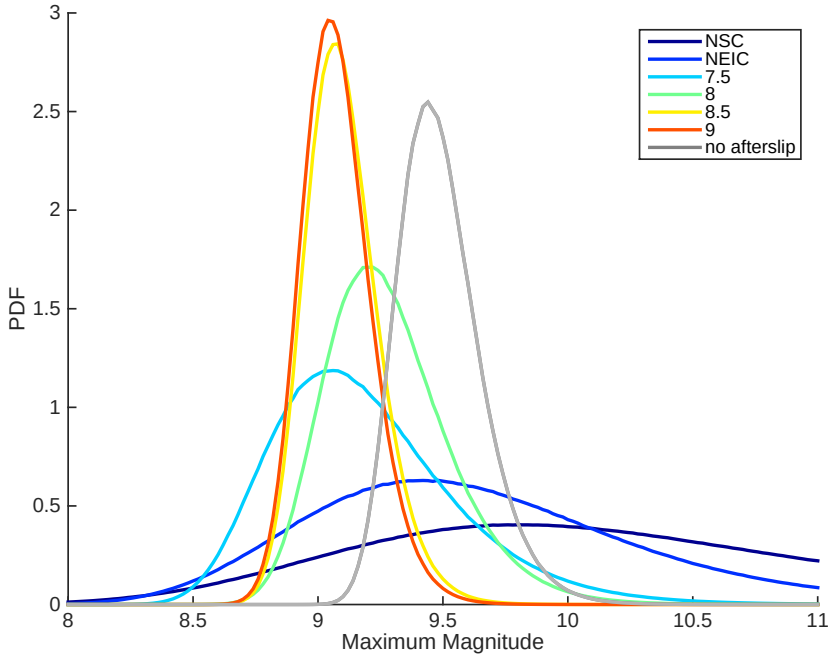

Figure 3.S2: Data sets combined. Grey line shows the case with zero afterslip.

main text), we see that for other large earthquakes, afterslip has varied between 10% and up to 70%. For the Chile M_w8.8 earthquake in 2010, 20-30% of the moment was released as afterslip (Lin et al., 2013). In Sumatra M_w9.1 earthquake, about 30% was released as afterslip (Chlieh et al., 2008). However in the Chichi M_w7.6 earthquake, only 13% was released postseismically (Hsu et al., 2006). For the Tohoku-Oki earthquake, about 20% of the moment was released as afterslip (Yamagiwa et al., 2015). For the seismogenic portion of the Central Peru megathrust, 50-70% of the moment may be released aseismically (Perfettini et al., 2010). If we assume no afterslip at all, we get a maximum magnitude of roughly 9.5 (grey line in Figure 3.S2).

Method 2

For the second method we relax the assumption of the GR distribution. We use the observation of one M_w8.7 and possibly one M_w9.0 in the past 500 and 1000 years, respectively, along with the assumption that independent earthquakes follow a Poisson distribution. The probability of observing k event over a time τ, given the seismicity rate λ is:

$$P1 = \frac{e^{-\lambda\tau}\lambda\tau^k}{k!} \tag{3.8}$$

where λ = occurrence rate, τ = time window considered, and k = number of occurrences. Knowing that we have seen one M_w8.7 in 500 years, and one $M_w > 9.0$ in 1000 years, we can work out the probability of not observing a possible larger magnitude event with a given return period ($1/\lambda$).

We then find the probability that these different sizes of earthquakes and recurrence times would take up the moment needed (P2).

We then multiply these two probabilities together to find the probability that the earthquake occurs and that all earthquakes combined (including this largest event with its specific magnitude and return time, and all smaller earthquakes) balance the interseismic moment deficit.

For example, P1 for one M_w8.5 event in 500 years is close to 1, and P1 for four M_w8.5 events in 500 years is only about 7%. P2 for the first event is almost zero, whilst P2 for the second event is 95%. This leads to their final probabilities both being low (almost zero in the former case and roughly 7% in the latter case).

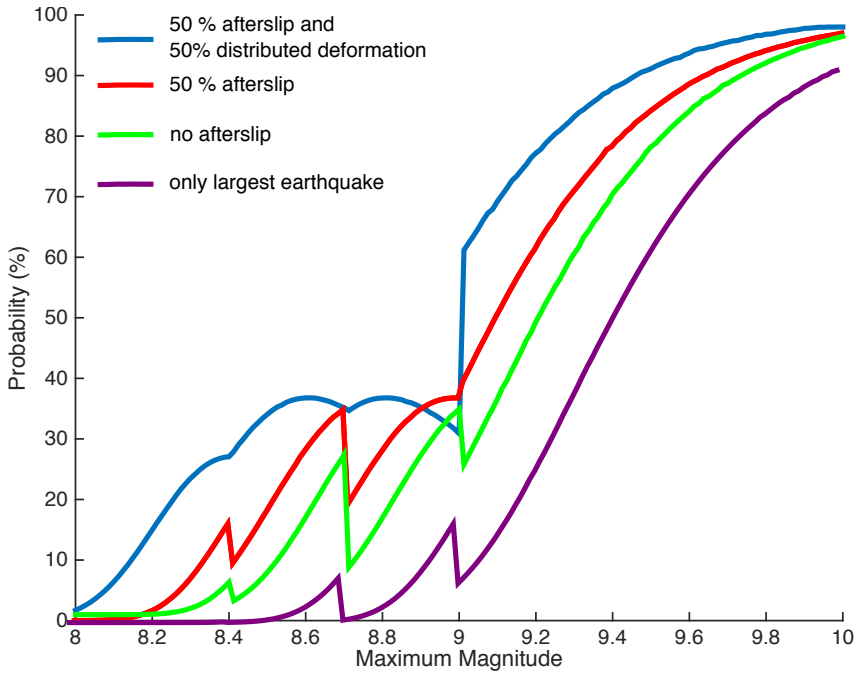

Figure 3.S3: The red line shows 50% afterslip and this is used in the main text. The green line assumes zero afterslip. The purple line shows the probabilities if we assume the largest earthquake releases all the moment, with 50% afterslip. The blue line shows 50% afterslip and a 50% decrease in moment build-up due to distributed deformation.

We also test alternative assumptions. As well as assuming here that the maximum earthquake is the largest in a catalog of earthquakes, we also show the end member where the largest earthquake is the only earthquake. With the former assumption, two-thirds of the moment is taken up in the largest earthquake, and one-third in all the other earthquakes. As expected, having no other earthquakes decreases the chance that a certain magnitude can take up all the moment (purple line in Figure 3.S3).

We also test the method assuming zero afterslip (green line), and assuming we have 50% less seismic moment build-up on the MHT (due to distributed deformation) as well as 50% afterslip (also shown in Figure 3.S4). Distributed deformation could occur if faults or folds north of the MFT took up some of the slip. 50% is an upper bound, and we expect only up to 10% of the deformation to be distributed (Stevens and Avouac, 2015).

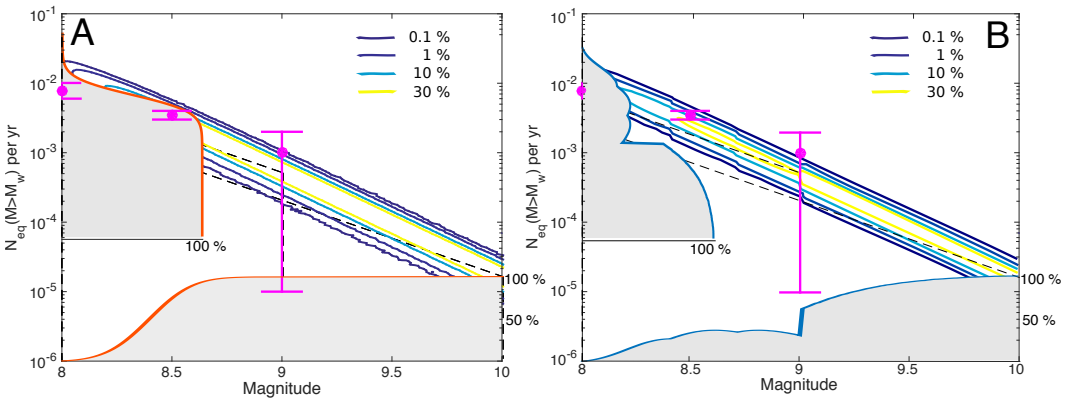

Figure 3.S4: Same as Figure 3.3 in the main text, but now assuming anelastic shortening of the Himalayan wedge takes up all the shortening across the Himalaya. The underlying MHT is still assumed seismic but long-term slip rate tapers linearly to zero at the surface. The rate of seismic moment build-up is halved.

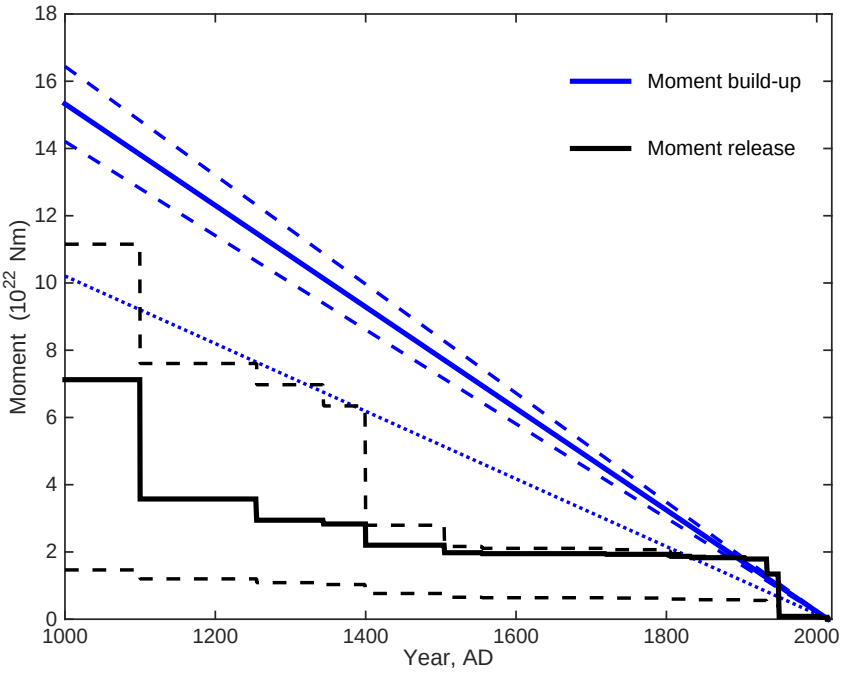

Figure 3.S5: Seismic moment released from major earthquakes along the Himlayan Front compared to moment accumulation since 1000 AD. Blue lines show moment build-up calculated from the coupling model of Stevens and Avouac (2015). The solid line shows the mean, the two dashed lines show the one-sigma errors. The dotted line shows the mean reduced by 50% - used in most of the calculations. The black lines show moment release. The solid line shows the preferred model, whilst the dashed lines show the highest and lowest reasonable magnitudes for past earthquakes.

Chapter 4

DETERMINATION OF THE MAXIMUM PLAUSIBLE EARTHQUAKE M_{MAX} FROM BACKGROUND SEISMICITY AND THE MOMENT BUDGET BALANCE

ABSTRACT

We describe a simple method to determine the maximum magnitude earthquake on crustal faults, M_{max}, and its return period. The method requires knowing the background seismicity rate, estimated from instrumental data, and the rate of moment deficit accumulation in the interseismic period, which can be estimated from the fault geometry, long term slip-rate, and assumed seismic coupling. Our method assumes a double-truncated Gutenberg-Richter (GR) law, and that the moment released by seismic slip balances the moment deficit accumulated in between earthquakes. We assume that in our instrumental record we are missing the many aftershocks that would occur from large infrequent events, which would increase the average rate of smaller earthquakes for the entire seismic cycle. We extrapolate the instrumental record using the GR law to model the frequency of larger events and their aftershocks. This increases the frequencies of smaller events on average, which when newly extrapolated predicts a higher frequency of larger events. We iterate this process until stability is reached, and then assume a balance of the moment build-up with the averaged catalog to find the maximum magnitude. We first apply and validate the approach with examples of faults with good historical catalogs. We next show examples of applications to faults with no historic catalogs, and test if the results are consistent with paleoseismic data where available.

4.1 Introduction

The magnitude, M_{max}, and return period of the maximum plausible earthquake on a particular fault or in a certain area is important in seismic hazard analysis. This information is most commonly derived from historical data, that is from the estimated magnitudes of earthquakes based on written records of shaking and building damage, and requires an a priori model of the frequency-magnitude distribution assigned to the fault or to the area of interest. One common difficulty is that, in absence of any physical constraints on the maximum possible earthquake, the distribution is unbounded and the maximum plausible earthquake depends on the time period considered (Holschneider, Zöller, and Hainzl, 2011; Zöller and Holschneider, 2016). If fault slip-rate or geodetic strain are known, the information can be additionally constrained based on a seismic moment budget (e.g. Kagan and Jackson (2013), Rong et al. (2014), Bird et al. (2015), Stevens and Avouac (2016), Ader et al. (2012), and Avouac (2015)). Ideally, the method involves the determination of the rate of elastic strain build-up on the active faults, which requires dense geodetic data, though this can also be estimated from the fault geometry and the long-term slip rate. We describe here a simpler method that does not require any historical data and assumes simply that the seismicity obeys the Gutenberg-Richter (GR) law (Gutenberg and Richter, 1944):

$$log(N(M > M_w)) = a - bM_w \tag{4.1}$$

where N(M>M_w) is the number of earthquakes above M_w, a is the y-axis intercept, and can be thought of as the productivity, and b is the slope of the line. The method requires only knowledge of the fault geometry, the long-term slip-rate of the fault and some earthquake catalog at the regional scale. More sophisticated methods can be used in areas with abundant information. The method here is most appropriate to regions where there is little information on past seismicity, fault slip rates and interseismic geodetic loading. Hereafter, we first describe common methods of finding M_{max}, the use of instrumental data, and discuss the probability that seismicity rate changes with time. We next describe our method and demonstrate that it performs relatively well when applied to case-examples with relatively abundant data. We next apply it to less well-constrained examples.

Previous methods

Some simple methods of calculating M_{max} do not involve statistical analysis of the seismic catalog. One method is simply to use the largest earthquake in the

historical record and add 0.5 (Kijko and Graham, 1998; Sokolov, CH., and Wen, 2001), though this is very limited where there is no significant historical record, and may greatly underestimate M_{max} unless the record is very long. Another method is to use scaling relations between the length of the fault and the maximum earthquake (see relationships in Wells and Coppersmith (1994)). This method can be applied where there is no historical data, but issues come with deciding on whether, and how, to divide the fault up into segments. Recently we have seen earthquakes that have ruptured through previously defined separate 'segments', for example in the Tohoku-Oki 2011 and Sumatra 2004 earthquakes, exceeding the maximum expected earthquakes in those regions. Recently the USGS has discovered that perhaps earthquakes can 'jump' between different previously separated faults in Southern California, allowing for a prediction of larger M_{max} (Field et al., 2014).

Many studies use statistical methods based on historical earthquake catalogs to find M_{max}. The statistics can either be used alone to find M_{max} within a time range at certain confidence intervals (e.g. Kijko (2004), Zöller, Hainzl, and Holschneider (2010), and Zöller, Holschneider, and Hainzl (2013)), or the conservation of moment principle can be applied (e.g. Rong et al. (2014), Kagan and Jackson (2013), Bird and Kagan (2004), and Bird et al. (2015)). Methods that do not use the conservation of moment principle in general can only find M_{max}, within time intervals (e.g. Zöller and Holschneider (2016) and Holschneider, Zöller, and Hainzl (2011)). In both methods, the double-truncated GR distribution (Kijko, 2004; Holschneider, Zöller, and Hainzl, 2011), with a 'hard' M_{max}, or the tapered GR distribution (Kagan, 1997; Bird and Kagan, 2004), with a 'soft' M_{max}, can be used. This soft limit is the magnitude above which the frequency of earthquakes no longer follows the GR rate, but tapers off exponentially, meaning the seismic moment release follows the Gamma distribution (Kagan, 2002a; Kagan, 2002b; Zöller, Hainzl, and Holschneider, 2010). Other methods include characteristic earthquakes (e.g. Field et al. (2014)) or there are methods where no a priori distribution needs to be defined (e.g. Kijko (2004)). This method uses a non-parametric Gaussian estimator based on the data themselves to find M_{max}, though this method in practice requires several of the largest events to already be recorded in the catalog. Other methods use the theory of extreme values of random variables to find M_{max} (Pisarenko et al., 2008; Pisarenko, Sornette, and Rodkin, 2010).

Using instrumental data and changing rates

In various areas across the globe, GR extrapolation of the instrumental data (that is, the earthquake rates recorded instrumentally, which have taken place for roughly the past 40 years), to higher magnitudes, seems to underpredict the number of larger earthquakes seen in the historical catalog and previous attempts to use the instrumental record to predict M_{max} have given results not in agreement with historical records (e.g. Wesnousky (1994) and Stirling, Wesnousky, and Shimazaki (1996)). For example, in California the extrapolated instrumentally predicted rates of magnitudes 6 or 7 were half that seen in the historical record (e.g. Stirling, Wesnousky, and Shimazaki (1996) and Field, Jackson, and Dolan (1999)). In Japan also, many faults show low instrumental seismicity compared to historic data (Ishibe and Shimazaki, 2012; Parsons et al., 2012).

This underprediction of historical rates led to the characteristic earthquake (CE) hypothesis (Schwartz and Coppersmith, 1984; Kagan, 1993; Wesnousky, 1994; Stirling, Wesnousky, and Shimazaki, 1996; Field, Jackson, and Dolan, 1999). The CE model has more recently gone out of fashion, for example in California where the CE model was originally developed, many studies suggest a GR distribution fits better on the San Andreas Fault for instrumental, historic and paleoseismic data (e.g. Parsons and Geist (2009), Field and Page (2011), and Page and Felzer (2015)). More recent paleoseismic studies also suggest a more diverse size of larger earthquakes on individual segments, so more consistent with the GR rather than CE law (e.g. Akçiz et al. (2010)). Other studies suggest GR also fits well in other regions e.g. Parsons et al. (2012) found that a GR distribution could explain earthquake data in Japan.

Other problems with the CE model are that choosing segments is subjective (Geller, Mulargia, and Stark, 2015; Kagan and Jackson, 2012) and recently earthquakes have ruptured across many 'segments', such as Sumatra (Main et al., 2008), Tohoku-Oki (Kagan and Jackson, 2013), and recently the WGCEP has decided that earthquakes in California can jump across different 'segments' to increase M_{max}. Parkfield, a 'classic' example of a CE segment, has recently not behaved according to the CE model (e.g. Bakun et al. (2005)). It is even harder to define segments where there have been fewer paleoseismic and historical earthquakes recorded, so it would be hard in areas of sparse data which we focus on.

A way to reconcile the low instrumental seismicity with the GR law is to assume that the seismicity rate varies in time and in most places for the past few decades we have had lower seismicity than on average for that fault. In earthquake catalogs, unless we have recorded the complete seismic cycle, which will only be the case if the catalog is less than 30 or so years long, we are probably missing aftershocks of large events so the smaller earthquakes will appear less frequent than they actually would be on average over the entire seismic cycle. It has previously been suggested that the average seismicity is often higher than that recorded by the instrumental record, and that the mismatch depends on the time since the last large earthquake (Page and Felzer, 2015; Naylor, Main, and Touati, 2009). Page and Felzer (2015) suggest that rate changes in instrumental data can explain the discrepancy between extrapolated instrumental data and the frequency of large events in the historical record. Their study modeled aftershocks in California and showed that this could explain the discrepancy, and it would be similar elsewhere.

Rate changes have been observed in many places, at all magnitudes and timescales. In California, swarms can increase the short-term rate a hundred-fold (Vidale and Shearer, 2006). There have been clusters and quiescence in the LA basin, with potentially a trade-off with Mojave Desert seismicity (Dolan, Bowman, and Sammis, 2007) or the San Jacinto fault (Hutton, Woessner, and Hauksson, 2010). At the Wrightwood site there have been times when strain rate was three times the long-term average, and then periods of quiescence (Weldon et al., 2004). Also noted in the paleoseismic record are shifts of stress from the SAF to other nearby faults (Bennett, Friedrich, and Furlong, 2004). There are suggestions that the SAF has been anomalously quiet recently. Bird (2009) suggests that in the period 1997-2008, only 37% of the moment needed was released, mainly missing on the SAF and Cascadia subduction zone, and after the 1906 San Francisco earthquake seismicity rates decreased significantly in the local area, possibly due to stress shadowing from a coseismic static stress field change (Reasenberg, Hanks, and Bakun, 2003).

Similarly, triggering from static stress changes has been shown to dominate some regional catalogs, and Naylor, Main, and Touati (2009) showed that in Japan low monthly rates occurred much more often that high monthly rates, and this would also occur on longer timescales, so we are most likely to sample a lower rate. For

example, after Tohoku-Oki, seismicity jumped about 10 times immediately and then decayed to a rate around 3 times the pre-Tohoku-Oki value (Toda and Stein, 2013). Kagan and Jackson (2012) suggest that earthquakes, even large ones, are clustered in time and not quasi-periodic. We would have to wait for M_{max} to occur, with all its aftershocks, to find the average rate of small earthquakes. This is not convenient when we are trying to find M_{max}.

Many places show changes in earthquake rate, and in slip rate, so it is hard to say what the average rate of seismicity is on any fault, except from plate models. On the timescale of a few million years, much greater than repeat times, the far-field drivers of plate motion are stationary, but not stationary over shorter timescales where more local processes can lead to unsteady rates. In short catalogs, the degree of stationarity is impossible to assess. Jumps in mean rates coincide with infrequent extreme events. For example, the Sumatra 2004 earthquake was large enough to change the global frequency-moment distribution from a gamma distribution before the event to a pure power law GR afterwards (Main et al., 2008).

Finding magnitudes and recurrence intervals using paleoseismic data is difficult (Scharer et al., 2010; Akçiz et al., 2010). For example, the M_w8.8 Maule Chile earthquake had a peak slip half that of M_w9 Tohoku-Oki, but twice the along-strike slip (Zhan et al., 2012), so the normal scaling relations sometimes introduce large errors. Studying paleoseismic data with various trenches along-strike of the earthquake, Wesnousky (2008) showed that slip at the surface is variable along length, so the exact trench location could have a large effect on the magnitude estimates. Biasi and Weldon (2006) tried to overcome the problem of sampling only at a point, by scaling probabilities of finding a given displacement within a rupture for any magnitude considered, and the probabilities of each magnitude, though this method records a priori a decision about the frequency-magnitude distribution, so using it to determine whether it is GR or CE would be circular.

Paleoseismic events extend the catalog back in time, though often not enough to make a representative probability density function of recurrence times for different magnitudes (Parsons, 2008). Different studies have used the Wrightwood, California, paleoseismic site, to say that the occurrence of past earthquakes has three different distributions: (1) clustered (Weldon et al., 2004), (2) quasi-periodic (Scharer

et al., 2010), and (3) fitting the GR distribution (Parsons and Geist, 2009).

There are similar arguments on other faults about whether their slip rate and seismicity has been constant in time or not. Clustering in seismicity, probably due to stress transfer at the end of each rupture, has been observed on the North Anatolian Fault (Stein, Barka, and Dieterich, 1997; Hartleb et al., 2006). The Dead Sea Transform fault has had a similar slip rate for the past 20 Ma comparing geological (Garfunkel, Zak, and Freund, 1981) with GPS studies (Le Beon et al., 2008; Reilinger et al., 2006); however, it also shows clustering of earthquakes in time (Marco and Agnon (1995)). It has been suggested that earthquakes on the Alpine Fault have been quasi-periodic during the past 8000 years (Berryman et al., 2012), though on nearby faults the slip rates have been shown to be quite variable (Ninis et al., 2013). Even though it may seem that we have had many particularly larger earthquakes recently (e.g. Tohoku-Oki, Japan, Chile), these recent rates are not distinguishable from a normal Poisson process (Michael, 2011; Shearer and Stark, 2012) and there should be about 5 M>9 earthquakes per century, which is what was seen (Kagan and Jackson, 2013).

Given that even in California, there are arguments over GR or CE with different answers in different regions and using different datasets, we do not have enough data elsewhere to be able to suggest one model would work better than the other so we have used the simple GR model.

Next we explain the method, show some results where we compare them against historical data, and results where there is no historical data, then go on to discuss these results.

4.2 Model

Here we assume a double truncated GR relationship, with M_{max} being the hard upper limit, and the cutoff magnitude being the lower limit, below which the record is not complete. We also use the principal of moment conservation, which states that the moment buildup rate on the fault (from tectonic forces) would equal the moment release on that fault (from both seismic and aseismic processes). We model the average earthquake catalog for the entire seismic cycle by adding on larger earthquakes and their modeled aftershocks according to the GR law, and then find the upper magnitude of this catalog that is needed to balance the moment. This is visualized on Figure 4a, where we can draw a line on the GR plot of the frequency-magnitude that would be needed for each magnitude to balance the moment build-up (see sup-

plementary methods for more details). The earthquake catalog will also form a line, also on the plot. Where the full catalog, i.e., that which covers the entire seismic cycle, intersects the moment build-up line, this will be the maximum earthquake.

The model requires only an instrumental earthquake record (here 20 past years from the USGS catalog) and an estimate of the seismic moment build-up rate. This rate can be found either from interseismic coupling models where available or from the fault geometry and the average slip-rate (here both taken from the literature) through the relation $\dot{M}_\circ = \mu L W \bar{u}$, with $\dot{M}_\circ$ the moment rate build-up, μ the rigidity (here assumed to be 33 GPa), L the length of the fault, W the width of the fault, and $\bar{u}$ the slip-rate along the fault. The width can be calculated from the seismogenic depth and the dip of the fault. The brittle-ductile transition is around 8-15 km in the continents (e.g. Kohlstedt, Evans, and Mackwell (1995)) and the coupled depth of continental lithosphere is around 8.6^{+11}_{-4} km (Bird and Kagan, 2004). We assume strike-slip faults dip at 90^o and the seismogenic depth is 12.5±2.5 km unless there are better local estimates.

The main uncertainty with this method is that we do not know the proportion of moment build-up released aseismically versus seismically. This cannot be found without more in-depth knowledge of the seismic moment released over the full seismic cycle compared to the seismic moment build-up. For continental faults, often almost all of the build-up is released seismically and in our model we assume a uniform fraction of aseismic release from 0-20%. Moment build-up rate can also be found from geodetic data if available.

We use numerical analysis with Monte Carlo analysis of 100,000 average earthquake catalogs. Uncertainties in the input parameters such as the b value can have any form, and are propagated through the model to get the uncertainties in M_{max} and recurrence times. We describe our choice of b value and how we model aftershocks, and then go through the model using an example of the San Andreas Fault.

b-value

b-values are generally around 1, though they can vary in space and time (Wiemer and Wyss, 2002). For example in California, values of 0.9 (Bakun, 1999), 0.95 (Tor-

mann, Wiemer, and Hauksson, 2010), 1.02±0.11(Felzer, 2008), 1.03±0.12 (Page and Felzer, 2015), 1.05 (Marsan and Lengliné, 2008), and 1.09±0.9 for Landers aftershocks (Felzer et al., 2002) have been found, but many also find a value of about 1, from both historic and instrumental catalogs (Felzer, Abercrombie, and Ekström, 2004; Field et al., 2014; Hutton, Woessner, and Hauksson, 2010; Wang, Jackson, and Kagan, 2009). Reasons for variation are different areas studied, different tectonic settings, different catalogs used, different methods used to find the cutoff magnitude, errors in the magnitudes of historical earthquakes (Zöller, Hainzl, and Holschneider, 2010) and sometimes different magnitude scales. For example when the local magnitude was redefined in Southern California, the b value changed from 1.16 to 0.95 (Tormann, Wiemer, and Hauksson, 2010).

In Japan there are larger variations in estimates of b-value, from 0.88 for 92 years of historical data (Satake, 2015), to 0.9-1.2 for aftershocks of Tohoku-Oki (Omi et al., 2013; Toda and Stein, 2013), though still a general convergence around 1 (Bird and Kagan, 2004; Grunewald and Stein, 2006; Parsons et al., 2012).

Because of this variation in well instrumented regions, we do not believe a b-value could be found accurately in areas with sparse data (Felzer (2006)). Studies of instrumental global seismicity find a b-value of 0.93-0.98 (Bird and Kagan (2004) and Kagan and Jackson (2012)) and the average b value for continental strike-slip faults has been found to be 0.98 (Bird and Kagan (2004)). For this reason we assume a b-value of slightly more than 1 to err on the side of caution in terms of estimating the maximum magnitude size, so use 1.025±0.025 at 1-σ confidence levels for all areas studied, though this could easily be altered if different b-values were found.

Aftershocks

We try and create the average earthquake distribution, not by averaging globally (like Bird and Kagan (2004)), but by filling it in to get an average using aftershocks. We simulate aftershocks simply by assuming they follow a GR distribution with a b-value the same as the main catalog, and that they follow Båth's law (Båth, 1965), with the largest aftershock 1.2±0.1 below the mainshock. For example, every time we have a magnitude 8 in the record, we assume an aftershock sequence with the largest aftershock 6.8, and then smaller earthquakes with frequency in accordance

with GR. If the magnitude 8 occurred once every 100 years, this aftershock sequence would also occur every 100 years. It would be possible to use a different aftershock distribution in the model. This is similar to other studies that have modeled the number of aftershocks as $10^{\alpha M}$ where M is the mainshock magnitude and α is a parameter to be determined. In our model α is the same as the b-value, so about 1, as also used in other studies (Felzer, Abercrombie, and Ekström, 2004; Helmstetter, Kagan, and Jackson, 2005). ETAS models (Ogata, 1988) tend to have a lower value of α, from 0.5-0.7 (e.g. Marsan and Lengliné (2008), Console et al. (2003), and Guo and Ogata (1997)) that vary between aftershock sequences. ETAS models require various parameters to be known beforehand, which is exactly what we do not have in areas of sparse data.

Our aftershock model compares favorably with aftershocks observed in reality (see Figure S4.1). For Tohoku-Oki 2011 the largest aftershock was 1.1 magnitude unit below and the b value was 0.9-1.2 (Toda and Stein, 2013; Omi et al., 2013). For Gorkha 2015, the first aftershock sequence had the largest aftershock 1.1 magnitude unit below the mainshock, whilst the second larger aftershock was only 0.5 magnitude units below. The b value for this aftershock sequence (using the maximum likelihood method (Aki, 1965; Utsu, 1965) was found to be 1.08. 31 earthquakes above M_w5 occurred, and 105 above $M_w4.5$, while the model here would produce 40 and 125 respectively. For the Kashmir 2005 earthquake, the largest earthquake was 1.2 magnitude unit below, and the aftershock catalog had a b value of 1.09±0.07, as found by Tahir and Grasso (2014). Here the aftershock rate was high and 48 earthquakes above M_w5 occurred, and 198 above $M_w4.5$, while the model we use here would produce 25 and 80, respectively.

Data

The fault studied needs to cover an area large enough that GR is fulfilled, and where earthquake rates are constant over a time interval of 20 years. The model averages everything along the fault length, so can only be applied if the setting, percent seismic release, and instrumentally recorded earthquakes are fairly similar along its length. For the instrumental catalog, the events are a lot smaller, so they have to be within 10 km of the fault trace, except for the Kunlun and Boconó faults where the traces are less well known and errors in epicentral locations are greater so we use 20 km.

For the instrumental catalog, we do not decluster fully, but we remove large earth-

quakes and their aftershocks. This is because the model assumes the final catalog will obey the GR law up to the largest earthquake, which is not the case with only one large earthquake and its aftershocks, as there will be a jump between the largest aftershock and the mainshock. For example, the M_w7.8 Gorkha 2015 earthquake and its aftershocks were removed using Reasenberg declustering (Reasenberg and Jones, 1989).

Model steps: “Filling in" the earthquake catalog to find average activity rate

Here we choose Gaussian uncertainties for b, seismogenic depth and cutoff magnitude (M_c) value, while we use a uniform distribution for the fraction of moment released aseismically.

From Figure 4.1a, a precursory look would suggest that extrapolating the instrumental data, and assuming GR with a b-value of around 1, would give a maximum magnitude of around M_w9, which is very high. As described earlier, we suggest that this is because the instrumental catalog does not show the average over the entire seismic cycle, as it is missing all the aftershocks from large events. In our model we try and simulate a complete averaged catalog. This includes larger earthquakes not recorded in instrumental time, and all of their aftershocks.

1. In the first step we guess a maximum magnitude that is larger than we expect the answer to be. In Figure 4.1b and c we show the example where we have initially chosen 9. We initially find the rate at the cutoff magnitude (found using the maximum curvature method, implemented using ZMAP (Wiemer, 2001) to extrapolate the instrumental data according to the GR law, and add on the number of ‘missing’ M_w9 earthquakes it suggests. We then also add on the modeled aftershocks. This increases the average rate of smaller earthquakes so raises the entire instrumental catalog slightly. We then extrapolate again from this new slightly raised catalog to find the number of ‘missing’ M_w8.9 earthquakes (with a smaller step-size, fewer iterations would be needed, but the results would converge to the same value). Again we add their aftershocks, again this raises the instrumental catalog, and repeat this process going down in steps of 0.1 until the cutoff magnitude, in this case M_w4.4. This process is shown in Figure 4.1b.

2. Now we have added earthquakes from M_w9 to M_w4.4, the instrumental catalog has been shifted upwards, and we realize that we have added on too few

M_w9 earthquakes for what the extrapolation now predicts. This can be seen from the difference between the highest orange line (old extrapolation) and the lowest yellow line (new extrapolation) in Figure 4.1c. Therefore we repeat the entire process again, with two more repetitions shown in Figure 4.1c in orange, yellow, and green. The adjustments needed in each loop become smaller and smaller until the addition is minimal.

3. After steps 1 and 2 we find that we have an 'averaged' seismic catalog for the entire seismic period, with a maximum magnitude of 9. However, this extrapolated (green) line intersects the maximum earthquake line at M_w8.1, suggesting that M_w8.1 would be the maximum earthquake. This is therefore inconsistent, so we have to lower our trial guess. As we lower our guessed maximum magnitude earthquake, the final predicted maximum earthquake becomes slightly higher, as we have added on fewer earthquakes. We decrease our guessed value until it matches the value predicted, so we have been consistent. This is shown in Figure 4.1c, where our initial maximum magnitude was guessed at 8.1, and the predicted maximum magnitude is also 8.1.

We test the instrumental data for the SAF to see if it is a reasonable realization of 20 years of data of the modeled final average catalog for that fault. To do this we first find the number and magnitude of mainshocks in the modeled final catalog. We want to generate catalogs that cover 20 years, so if the recurrence time of the largest earthquake is e.g. 200 years, we randomly select 10% of the mainshocks. We add aftershocks to the mainshocks (which start at a magnitude of 1.2±0.1 below the mainshock (1-σ error)), which in the case shown (Figure 4.2), since the cut-off magnitude is 4.5, only contribute when the mainshock is above roughly magnitude 5.7. The results show that our instrumental catalog is a reasonable realization of the modeled average catalog.

4.3 Results

In all our examples we use earthquakes from the USGS catalog (http://earthquake.usgs.gov/) from 1996 to present, giving us 20 years of data. For strike-slip faults we select earthquakes within 10 km of the fault trace, to allow for errors in the epicenter, fault trace locations, and off-vertical dips. For reverse faults we consider the dip of the fault. We assign a b-value of 1.05±0.25 (1-sigma, with a Gaussian distribution) everywhere. We assume the seismogenic depth is 12.5±2.5 unless we have

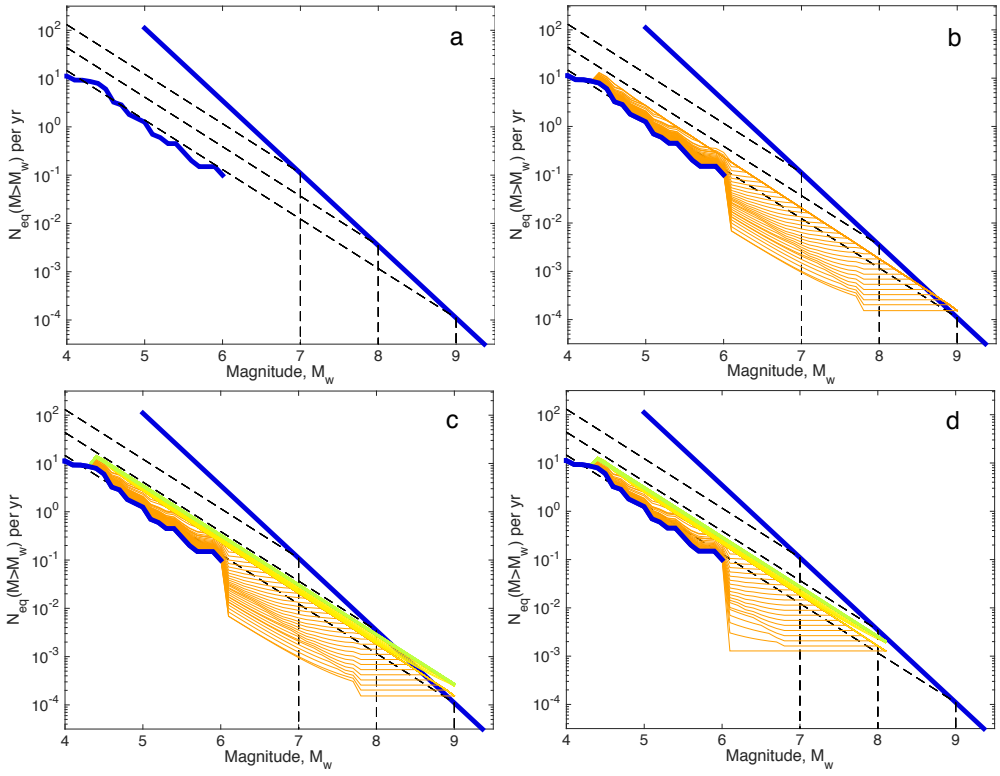

Figure 4.1: Demonstrating steps of the method. Straight blue line is moment build-up rate line, which shows the frequency of the maximum magnitude earthquake that would need to occur to take up all the moment build-up. The lower wiggly blue line is the instrumental catalog, here from the San Andreas Fault. The black dashed lines are demonstrative to show the GR law with b of 1, so where the earthquake catalog should lie to intersect maximum magnitudes of 7, 8, and 9. a) The original setup. b) Orange lines show the first round of adding on missing earthquakes from magnitude 9 down to the cutoff magnitude, here 4.4. c) Orange lines are the same as for b, but now yellow and green lines show two more rounds of adding on missing earthquakes. The number needed to be added on decreases with each round, which is why the lines get closer and closer together. d) Same as c but now showing a trial maximum magnitude of 8.1, which is the maximum magnitude that is predicted.

evidence that it differs. We take the fault traces and slip rates from the literature. To calculate moment build-up we need the length of the fault, the seismogenic depth, and the slip rate.

San Andreas Fault (SAF)

The SAF is a heavily studied large continental strike-slip fault, in the vicinity of large population centers such as LA and San Francisco. We assume an average

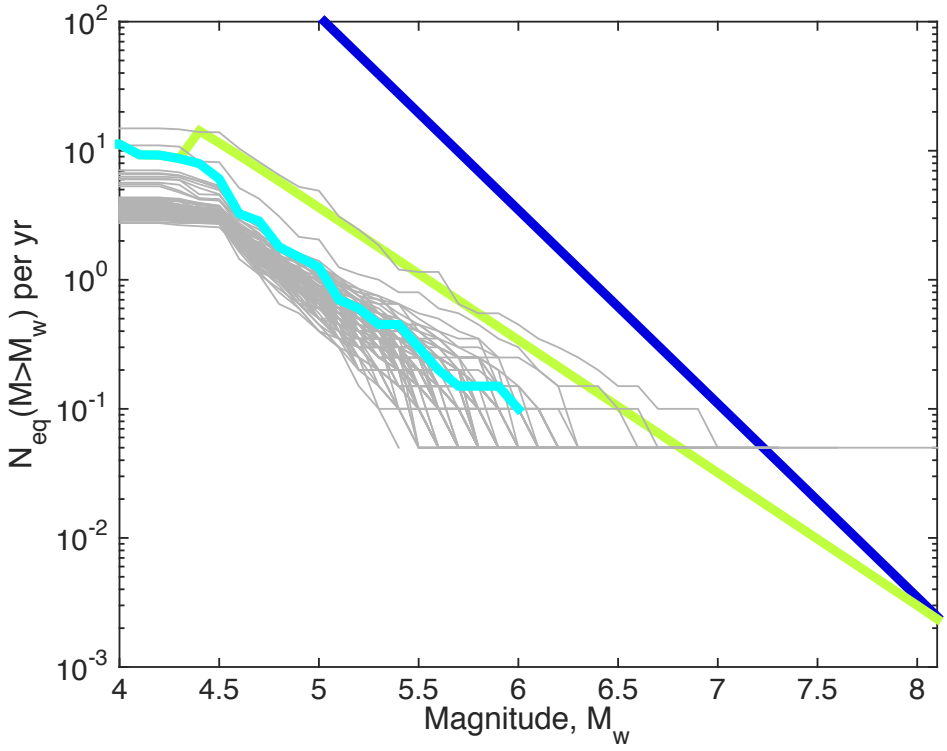

Figure 4.2: Comparing instrumental data of the light blue line with 100 realizations of 20 years of data with the same statistics as the mainshocks in the final average catalog test shown in gray. These different realizations have varying maximum sized earthquakes, from 5.3 to 8.2 in the cases shown here.

velocity on the fault of 30±5 mm/yr at the 1-σ level, though there is some variability in this rate depending on the location (Meade and Hager, 2005; Weldon and Sieh, 1985). The locking depth seems to fit the default value of 12.5±2.5 km (Meade and Hager, 2005; Smith-Konter, Sandwell, and Shearer, 2011) so we do not change this. This gives us an average moment build-up rate of 6.6±1.8x10^{18} Nm/yr. Though there are some variations, studies of b-values average around 1 in California for both the instrumental and historical record (Felzer, 2008; Wang, Jackson, and Kagan, 2009; Hutton, Woessner, and Hauksson, 2010). We compare the results with historical earthquakes (NGDC, 2016; Stover and Coffman, 1993) within 20 km of the fault trace, as shown in Figure 4.3.

With these assumptions we find the maximum magnitude earthquake would be M8±0.3 at the 1-σ confidence level, with a recurrence time of 270 years, with a lower estimate of 150 years and upper estimate of 700 years. The largest reliably

known earthquake is the Fort Tejon M 7.9 in 1857, which ruptured roughly 350 km of the SAF. Previous estimates of M_{max} are similar to that estimated here, from M_w8 (Field, Jackson, and Dolan (1999), using CE and conservation of moment) to 8.3±0.4 (Kijko (2004) using statistics of the earthquake catalog). Paleoseismic data recurrence intervals from different segments vary from 88±41 years for magnitudes 6.5-7.9 (Akçiz et al., 2010) in the Carizzo Plain, to roughly 70 years at the Wrightwood paleoseismic site with rough magnitudes of 6.8 to 7.9 (Scharer et al., 2010), whilst our model would predict an earthquake above 6.5 roughly once every 20 years for the entire length of the SAF. Field, Jackson, and Dolan (1999) predict an earthquake of magnitude > M_w7.8 every 334 years on average for Southern California.

North Anatolian Fault (NAF)

The NAF is 1200 km long, from the east to the north Aegean in the west. Slip rates vary from 20 mm/year in the east to 25 mm/year in the west (Şengör et al., 2005; Kozaci et al., 2007). We use a slip rate of 22±3 mm/yr and a seismogenic depth of 15±3 km (Bohnhoff et al., 2016) to calculate the seismic moment build-up. We remove the Izmit 1999 M_w7.6 earthquake and aftershocks from our catalog, and are left with 82 earthquakes above the cutoff magnitude, found to be M_w4.5. We compare the result with historical data from the past 2300 years, apparently complete to above M_w7.4 (Bohnhoff et al., 2016).

We predict $M_{max}$is 8±0.3 with a recurrence time of 275 years, lower estimate of 134 years and upper estimate of 650 years. The maximum historical earthquake with a reliable magnitude was M_w7.8 in 1939. Previous estimates of M_{max} are in the M_w7.9-8.1 range(Bohnhoff et al., 2016). Estimates of inter-event times for paleoseismic earthquakes vary widely from 210-280 years (Klinger et al., 2003) to 200-900 years (Hartleb et al., 2006). There seems to have been a cluster of earthquakes > M_w6.7 in the past century, and there are suggestions of similar sequences in the 17th-18th centuries, and 10th -12th centuries (Hartleb et al., 2006). This variable rate can be seen in Figure 4.3b, and shows the paleoseismic record over the past 2300 years and the same record just taking the most recent 100 years (Bohnhoff et al., 2016). The record in the past 100 years is probably higher than average due clustering, though the record over the past 2300 years may be lower due to missing events, which become harder to detect back in time, when also the magnitude is harder to estimate. For example, there are 5 earthquakes >7.5 recorded between

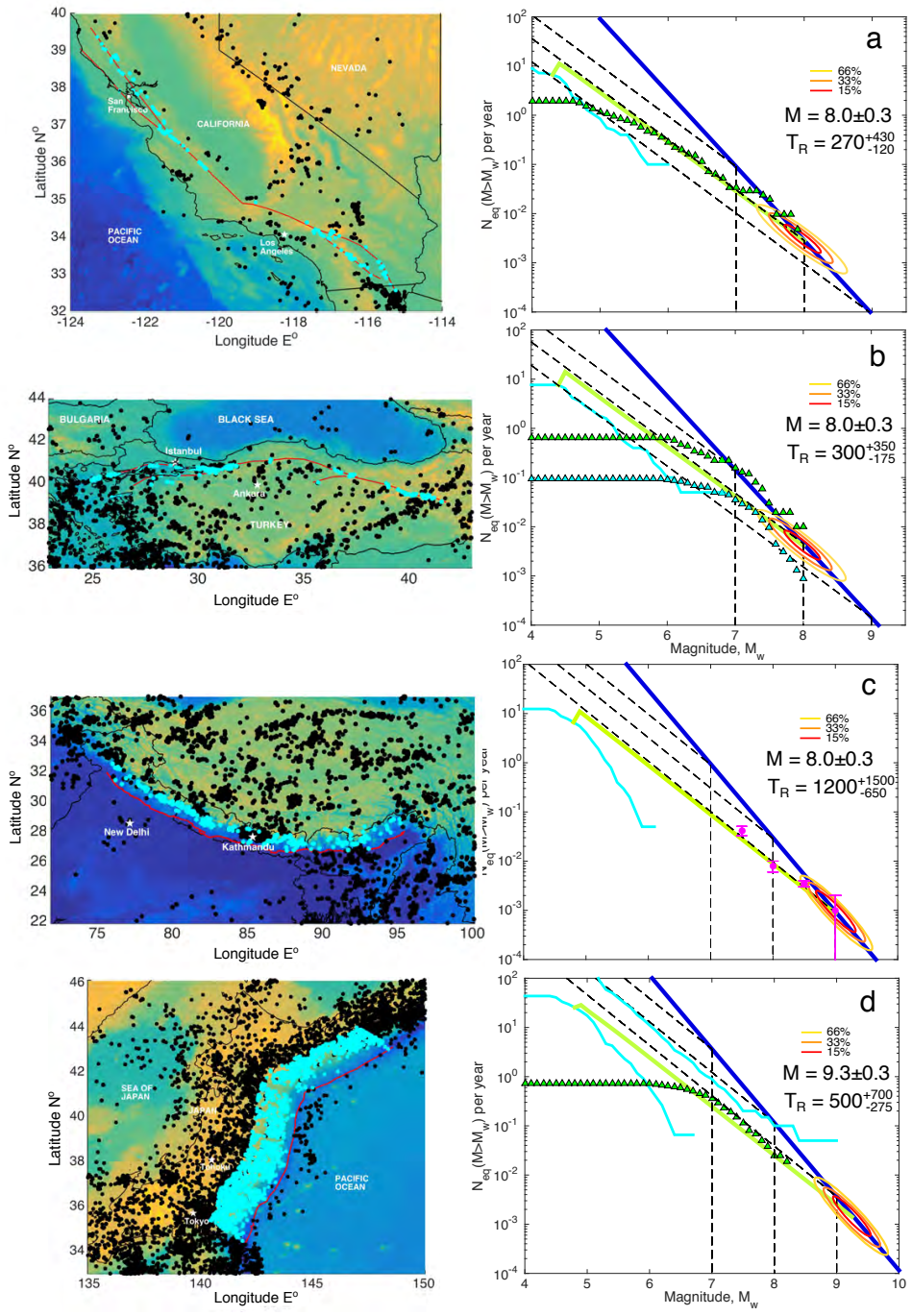

Figure 4.3: Results of the model. Here the yellow, orange, and red lines show the probability of being within the ovals, taking into account the uncertainties on the b-value, the moment build-up rate and the value of the largest aftershock. Here the straight green lines show the final averaged modeled catalog. Light blue lines show the instrumental catalog and the dark blue line is the moment conservation line. The left-hand panels show the fault in red with earthquakes as black dots, and earthquakes selected to use in the model as blue dots. a) The San Andreas Fault. Here green triangles show the historic data. b) The North Anatolian Fault. Green triangles show the historic data averaged over the past 100 years, whereas blue triangles are averaged over the past 2300 years. c) The Main Himalayan Thrust with pink dots and error bars showing the historical data. d) The Japan Trench, with green triangles showing the historic data.

300BC and 1000AD, but then 17 from 1000 to present, with at least 3 per 200 years, compared to periods of more than 200 years with no M_w >7.5 earthquakes further back in time. Noting the high temporal variability in the paleoseismic record, and potential for incompleteness, our model does not disagree with these data.

Main Himalayan Thrust (MHT)

The Main Himalayan Thrust is a very large continental thrust fault along which the Indian Plate is thrust beneath the Himalaya. It has produced large earthquakes in the past and poses a large threat to the numerous nearby population centers. Instead of the normal moment calculation, we use a moment build-up rate of $15.1 \pm 1 \times 10^{19}$ (Stevens and Avouac, 2015) and allow 33% of the moment to be released non-seismically (by afterslip), following Stevens and Avouac (2016). We take earthquakes within 150 km north perpendicular to the surface trace of the MFT, and exclude the Gorkha April 25th 2015 earthquake and its aftershocks. Figure 4.3c shows the results and a comparison with the historical/paleoseismic record for the past 1000 years, summarized by Stevens and Avouac (2016).

We get a mean M_{max} of 9 and an uncertainty of 0.2, lower than elsewhere because the moment build-up is more constrained. The mean recurrence time would be 1200 years, with a variation from 550 to 2700 years. There is a 66% chance that M_{max}has to be over M_w8.7 (the largest historical earthquake) and about a 95% chance that is has to be above M_w8.5 (and less than M_w9.5). It has been noted previously that there is a moment deficit in this area (Bilham, Gaur, and Molnar, 2001; Stevens and Avouac, 2016), and large paleoseismic events have been proposed in the past, potentially up to M9 (e.g. (Kumar et al., 2010; Lavé et al., 2005; Upreti et al., 2000). Stevens and Avouac (2016) find a 66% chance that M_{max} has to be 9 or over, higher than M_w8.7 here. This is partly because Stevens and Avouac (2016) used a higher b-value, and used historic/paleoseismic data. Uncertainties in the b-value lead to larger uncertainties the larger M_{max} is predicted to be, since the data has to be extrapolated further. Extrapolating from historical and paleoseismic earthquakes suffers less from b-value uncertainties, but the uncertainty in the rates is then much higher.

Japan Trench

The Japan Trench, off the NE coast of Japan, is a fast converging subduction zone, where the Pacific and Okhotsk plates collide, that has frequent large earthquakes of

M_w ~7.5, and infrequent giant earthquake such as the M_w9 Tohoku-Oki earthquake of 11th March 2011 and a corresponding high seismic hazard. We use a mean slip rate of 80±8 mm/yr (DeMets, Gordon, and Argus, 2010), an average dip of 13^o and a seismogenic depth of 35±5 km (Zhan et al., 2012) to calculated moment build-up. We select instrumental earthquakes on the down-dip side, within 250 km of the fault trace (about 50km further than used for the moment calculation). We only use the catalog before the Tohoku-Oki M_w9 earthquake, as this completely contaminates the catalog with aftershocks. We also remove the M_w8.3 Hokkaido event of 2003 and its aftershocks. With a dip of 13 and seismogenic depth of 35±5 the interface is coupled to within about 200 km of the trench, which agrees with the limits of the aftershock distribution after the Tohoku-Oki earthquake (Shinohara et al., 2013). As with other reverse faults, we initially take the coupling fraction to be 66%. We show the results and a comparison with the historical record since 1850 (Usami, 2002) in Figure 4.3d.

Our mean M_{max} is 9.3 with 1-sigma error of 0.3. The mean repeat time is 520 years, with a lower bound of 223 and upper bound of 1200 years. The largest earthquake we know of for the Japan trench is the 2011, M_w9 Tohoku-Oki event, so here we have a high lower bound for M_{max}. Previous estimates for M_{max} have varied from 9 (McCaffrey (2008), using scaling relations and fault segment lengths) to 10 if confidence limits are high (Zöller et al. (2014), using the tapered GR distribution, but not conservation of moment). Using the theory of extreme values, Pisarenko, Sornette, and Rodkin (2010) found the absolute M_{max} to be 9.57±0.86 for Japan. With the model and assumptions here, there is a 30% chance that ≤M_w9 could be M_{max}, but almost zero chance that it would be as large as M_w10.

Estimates of recurrence times suggested for the largest events are based on either conservation of moment, giving 532 years (McCaffrey, 2008) and 260-280 years (Uchida and Matsuzawa, 2011) or based on the historical record , giving 300-400 years (Kagan and Jackson, 2013), and 600 years for the Tohoku-Oku area (Satake, 2015). The last agreed upon event that had a magnitude similar to Tohoku-Oki us the 896 AD event (Minoura et al., 2001), identified by tsunami deposits. At least two more large tsunami deposits have been found in this area in the past 3000 years, suggesting a recurrence time of around 1000 years. Others, however, have suggested that other past earthquakes were also as large as Tohoku-Oki, such as

the 1611 Keicho earthquake. In the Kuril trench just NE of Japan, with a similar tectonic setting, tsunami-causing earthquakes have occurred in the past 2000-7000 years, with a rough recurrence time of 500 years (Nanayama et al., 2003). However, some recording of tsunamis may come from far-field events, like earthquakes in Chile (Ishimura and Miyauchi, 2015). This paleoseismic data does not disagree with M_{max} of 9.3 and repeat time of 520 years for the entire Japan Trench. The modeled catalog agrees quite well with the historical record, where recurrence times would be 3 years for $M_w > 7$, and 40 years for $M_w > 8$. In the results of my model, recurrence times would be 4 years for $M_w > 7$ and would also be 40 years for $M_w > 8$.

The ability of earthquake rates to change drastically can be seen by comparing the average instrumental catalog before the 2011 earthquake, and the average catalog including the 2011 earthquake and its aftershock. These two lines can be seen in Figure 4.3d. Including the full catalog, we have a repeat time for earthquakes > 8 of 10 years, as oppose to 40 years beforehand, and on average 250 earthquakes > 5 per year compared to only 20 > M_w5. This shows that the instrumental catalog we have could be a lot lower than average if we have not had any large events in it, which is quite likely.

Coupling is the largest unknown here, with variations along the Japan trench between almost 0 and 80% (Loveless and Meade, 2015; Uchida and Matsuzawa, 2011)) The average coupling is somewhere in between. We initially assume an average coupling of 66%, as we have done for the MFT, perhaps erring on the higher side. This unknown fraction of seismic build-up is a greater problem for subduction zones, which have very variable coupling, than for continental strike-slip faults where the coupling is generally much higher and more consistent along strike, though with some variations. If instead of fixing the fraction of coupling, we fix the largest magnitude at M_w9, we can work out the amount of aseismic release that would correspond to this. We have initially assumed that coupling is on average 66%, but we need coupling of 45% for magnitude 9 to be the average maximum magnitude, which would give a repeat time of 400 years.

Boconó Fault

This fault is a right-lateral strike-slip fault that stretches roughly 500 km from the Colombian-Venezuelan border in the SW to the Caribbean coast in the NE, through the Venezuelan Andes. Rates of 5-9 mm/yr have been suggested for this fault (Audemard et al., 1999; Audemard, 2005; Schubert and Sifontes, 1970), taking up most of the 10 mm/yr full plate motion. We take a rate of 7±2 mm/yr, at the upper end of suggested rates. Here we select earthquakes within 20 km of the fault trace to allow for larger errors in the location of the fault trace and earthquake epicenters here. Microseismicity has been found mainly between 0 and 15 km depth (Pérez, Sanz, and Lagos, 1997), with some microseismicity in the lower crust (Audemard et al., 2008), so we take the locking depth to be 15±2.5 km.

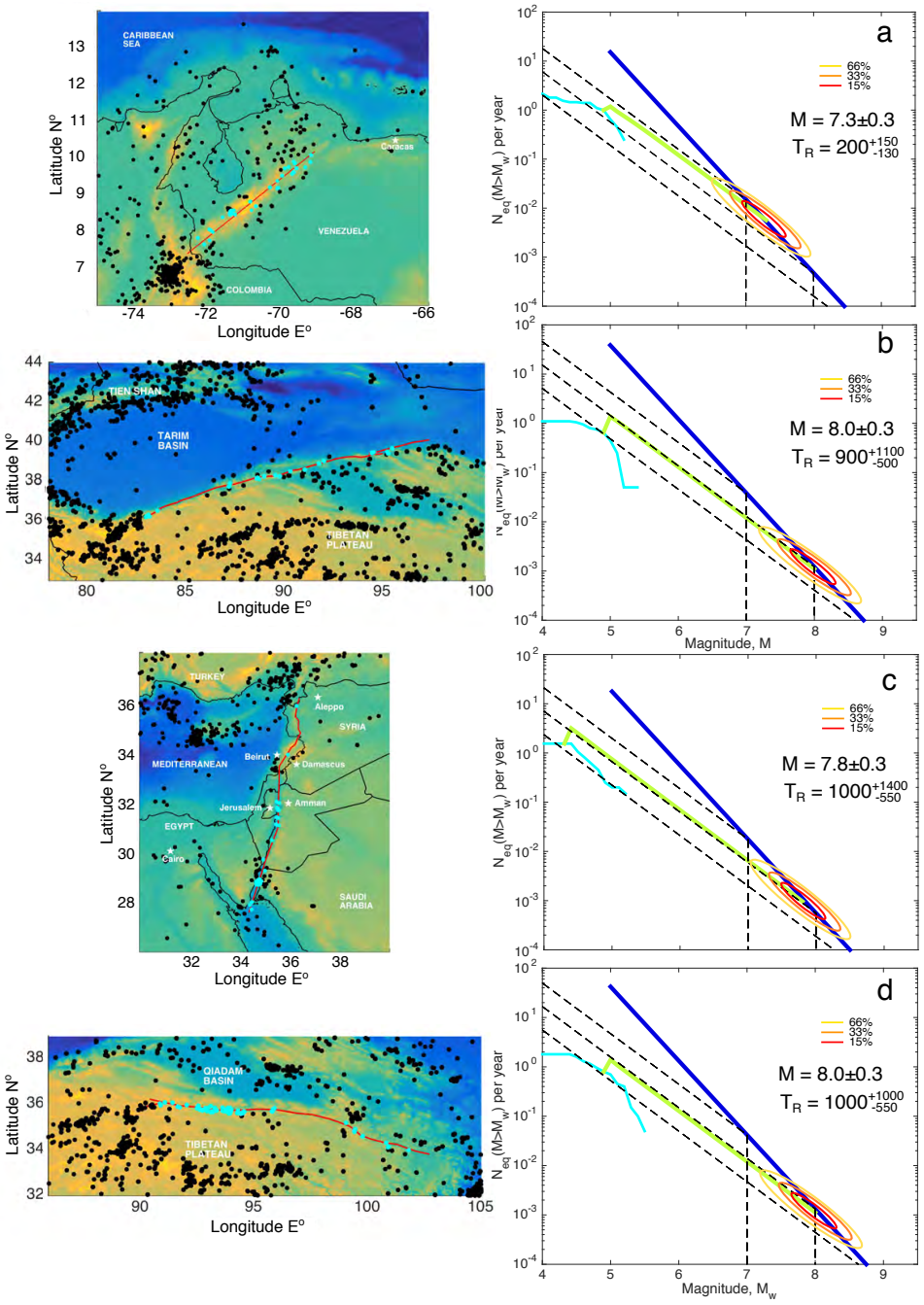

Figure 4.4: Results of the model for areas without long historic data catalogs. a) Boconó Fault. c) Altyn Tagh Fault. b) Dead Sea Transform. d) Kunlun Fault.

We find that the mean M_{max} is 7.3±0.3. The mean recurrence time would be 160 years, with an upper bound of 360 years, and a lower bound of 70 years. In more recent times, the largest earthquakes have been the magnitude 5.5 in 1975 and 5.6 in 1977; however, historical earthquakes in 1610 and 1894 may have had magnitudes of 7.1-7.3, found from trench excavations in the southern section (Audemard, 1997), with a suggested recurrence time of about 300 years in this area. In the central section, at least 15 earthquakes of M > 7 have been found during the past 20,000 years, with probably quite a few missing (Audemard et al., 2008). Recurrence intervals were found to be variable, from 400 years up to 1800 years. An event in 1812 caused a lot of damage, devastating the town of Mérida, and felt as far away as Caracas, with the Boconó fault a possible source (Altez, 2005; Audemard et al., 2008) though this has not been confirmed. From scaling relations of fault length, M_{max} has be suggested as between 7.2-7.9 (Schubert, 1982).

Altyn Tagh Fault

The Altyn Tagh is a large left-lateral strike-slip fault bordering the North-West side of the Tibetan Plateau. There have been no large earthquakes recorded instrumentally, though the fault has an offset of around 475 km since around 25 Ma and there is evidence of large ruptures in the past (Washburn et al., 2003). Slip rates on the Altyn Tagh are roughly 10 mm/yr (Cowgill et al., 2009; Elliott et al., 2008), with a locking depth of around 15 km (Elliott et al., 2008).

We find mean M_{max} of 8±0.3, with a recurrence time of 900 years, up to 2000 years and down to 400 years.There is evidence for 2 or 3 events in the central section of the Atyn Tagh during the past 2000 years, with a magnitude of roughly between 7 and 7.8 (Washburn et al., 2003). This is consistent with our model.

Dead Sea Transform (DST)

The DST is a 1000 km-long continental left-lateral north-south trending, strike-slip fault, with a long, though incomplete historical record and some paleoseismic data.The DST has an average slip rate of about 5 mm/yr (Garfunkel, Zak, and Freund, 1981; Le Beon et al., 2008; Reilinger et al., 2006; Wdowinski et al., 2004) and a locking depth of about 12-14 km (Le Beon et al., 2008; Salamon et al., 2003).

We find the mean M_{max} is 7.8±0.3, with a recurrence time of 1000 years, with a lower estimate of 450 years, and a higher estimate of 2400 years. The largest earthquake recorded is a potential magnitude 7.8 in 1157 AD (Ambraseys and Jackson,

1998)). More recently the largest event has been a magnitude 7.3 event in 1995 in the Gulf of Aqaba. Other estimates of M_{max} suggest up to M_w 7.8 in the southern section (Klinger, Le Béon, and Al-Qaryouti, 2015) and up to 7.4-7.7 in the Dead Sea Basin region (Begin et al., 2005). It has been noted that the seismicity on the DST has been very low this past century with the seismic moment release less than 40 % of that expected (Salamon et al., 2003), and 86 % of that coming from one earthquake, the Gulf of Aqaba M_w 7.3 event. Seismicity has also been low for the past 830 years (Meghraoui, 2014), with periods of quiescence and interspersed with higher rates (Klinger, Le Béon, and Al-Qaryouti, 2015; Marco and Agnon, 1995). In the Araba Valley segment (160 km of the almost 1000 km DST length), there have been at least 4 events of $M_w > 7$ in the past 1000 years (Klinger et al., 2000), giving a recurrence time of roughly 250 years. Our model suggests a $M_w > 7$ should occur roughly once every 115 years, so twice as often; however, our model is for the entire length of the DST, whereas the Araba Valley segment covers only around one fifth of the fault. The paleoseismic data do not disagree with our model, though the earthquake rate seems quite variable through time.

Kunlun Fault

The Kunlun fault is a large strike-slip fault in northern Tibet. It slips at a fairly constant rate of 11.7±1.5 mm/yr (Van Der Woerd et al., 2002), and we use the default seismogenic depth of 12.5±2.5 km.

We find M_{max} is 8±0.3 with a recurrence time of 1000 years, with lower bound 450 years and upper bound 2000 years. The largest earthquake we know of on the Kunlun fault happened recently, in 2001, M_w 7.8, with a 450 km land rupture. There have not been paleoseismic studies, though. From minimum terrace offsets and the average slip rate, Van Der Woerd et al. (2002) suggest that earthquakes around M_w 8 could occur on this fault once every 800-1000 years. The model here is consistent with that idea.

4.4 Discussion

We have shown that our model predicts the average seismic catalog well in cases where we have historic data. In these places, either historical catalog is complete, or we have not seen M_{max} yet. Errors in the historical catalog are hard to measure and quantify, and increase further back in time. Their magnitude is hard to measure accurately from shaking reports and scaling laws. Even if the magnitudes are well known, the recurrence times may not be, as they are variable and many data points

have to be found to get a good probability density function (Parsons, 2002). M_{max} has the longest recurrence time, so this is the most likely to be missed in the historical record.

In more global studies of M_{max}, M_{max} for continental strike-slip faults has been found to be $8.01^{+0.47}_{-0.21}$ and for subduction zones $9.58^{+0.48}_{-0.46}$ (Bird and Kagan, 2004). Other estimates for subduction zones include ≥ 9 in 10,000 years (Rong et al., 2014), 9-9.7 (Kagan and Jackson, 2013) and 9.6 (Bird and Kagan, 2004).

The main advantage of this model is that it can be used in areas with no historic data. The model also does not require artificial segmentation, it requires no prior knowledge of parameters, and uncertainties are simple to model. There is a trade off in the model between errors in the b-value and uncertainties of the average frequency of earthquakes. Smaller earthquakes are more likely to be accurate in terms of frequency, but since they are far from M_{max}, projecting using the b value from here will cause larger uncertainties. For larger earthquakes, the frequency is less well known, though uncertainty in the b-value will introduce fewer errors since it does not have to project so far.

One disadvantage of this model is that it assumes a double-truncated GR, which might not be applicable everywhere. It is possible to change this, though it would involve more parameters, which might not be known well, especially in places with no historical data. It also makes assumptions about the aftershock distributions, though this could be easily altered to a preferred aftershock distribution. For example, in models such as Reasenberg and Jones (1989) and Felzer, Abercrombie, and Ekström (2004), aftershocks can grow to any size, potentially larger than the mainshock, which is not allowed here. Uncertainties in the b value lead to large uncertainties in the results, especially for larger earthquakes. Choosing which earthquakes are on the fault itself, and the moment build-up rate and fraction of aseismic afterslip on the fault might be difficult, though other methods also suffer from this problem, and data will surely get better in the future, especially as more GPS are introduced. Another disadvantage of my technique is that it cannot incorporate historical data recurrence times, as they are often not on the same trend as the instrumental data. The historical data can however be used to validate the model, though perhaps this data is not as accurate as those with smaller magnitudes.

Afterslip is another unknown in the model and we have not taken it explicitly into account. For continental earthquakes this can be small (e.g. < 10 % for the Gorkha earthquake) but is sometimes very significant (≈ 56 % for the Kashmir earthquake (Jouanne et al., 2011)). Afterslip also varies in subduction zones from 20-30 % after the Chile M_w8.8 event (Lin et al., 2013) to 50-70 % for the Peruvian trench (Perfettini et al., 2010).

4.5 Conclusion

Where others have estimated M_{max} or there is paleoseismic data, in general our results agree. For areas without historical data, fewer people have attempted to find M_{max}. For these faults in particular, our model highlights the seismic risk where in the recent past maybe no large earthquakes have occurred. These areas are particularly vulnerable, as the earthquake hazard perception and preparedness is low.

Supporting Information for "Determination of the maximum plausible earthquake M_{max} from background seismicity and the moment budget balance"

Introduction

Here we show the supplementary methods and extra figures.

Supplementary Methods

To find the moment build-up rate we use

$$\dot{M}_\circ = \mu L W \bar{u} \tag{4.2}$$

where L is the length of the fault, W is the width of the fault (seismogenic depth times sin(dip)), μ is the rigidity and $\bar{u}$ is the average slip rate.
To find the moment-line that the earthquake GR distribution will intersect we use the following equations. The GR law (Gutenberg and Richter, 1944) states:

$$log10N(M_w) = a - bM_w \tag{4.3}$$

where N(M>M_w) is the number of earthquakes above M_w, a is the y-axis intercept, and can be thought of as the productivity, and b is the slope of the line. The conversion between M_w and $M_\circ$ is:

$$M_\circ = 10^{\alpha(M_w+\beta)} \tag{4.4}$$

where $\alpha = 2/3$ and $\beta = 10.7$. So here

$$M_w = \frac{2}{3} log10(M_\circ) - 10.7 \tag{4.5}$$

The number of total earthquakes below magnitude M_w is:

$$N_\circ = 10^{\alpha} - 10^{(a-bM_w)} \tag{4.6}$$

The total moment release is:

$$Moment = \int_{-\infty}^{M_w} M_\circ(M'_w) N_\circ(M'_w) dM'_w \tag{4.7}$$

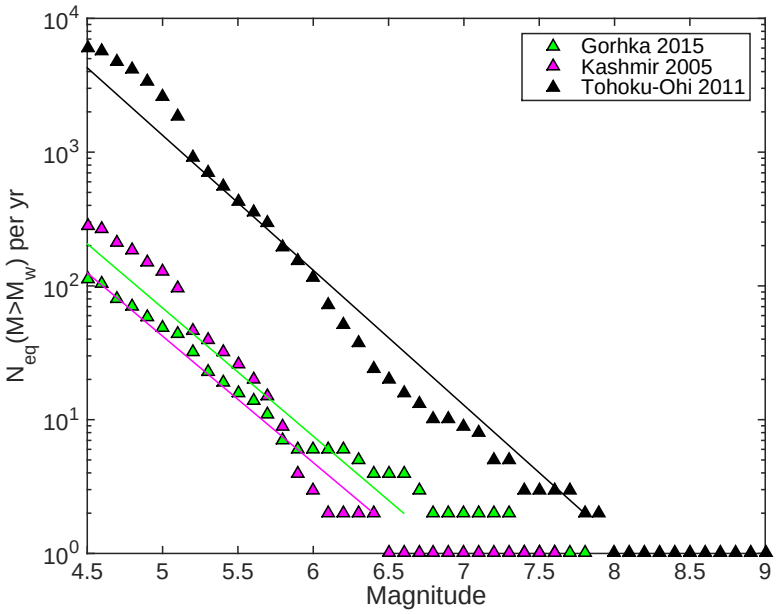

Figure 4.S1: Comparing the aftershock model (straight lines) with observations

BIBLIOGRAPHY

Ader, Thomas et al. (2012). "Convergence rate across the Nepal Himalaya and interseismic coupling on the Main Himalayan Thrust: Implications for seismic hazard". In: *J. Geophys. Res.* 117.B4. ISSN: 0148-0227. URL: http://dx.doi.org/10.1029/2011JB009071.

Ader, Thomas J. and Jean-Philippe Avouac (2013). "Detecting periodicities and declustering in earthquake catalogs using the Schuster spectrum, application to Himalayan seismicity". In: *Earth and Planetary Science Letters* 377-378, pp. 97–105. ISSN: 0012-821X. DOI: http://dx.doi.org/10.1016/j.epsl.2013.06.032. URL: http://www.sciencedirect.com/science/article/pii/S0012821X13003555.

Akçiz, Sinan O. et al. (2010). "Century-long average time intervals between earthquake ruptures of the San Andreas fault in the Carrizo Plain, California". In: *Geology* 38.9, pp. 787–790. DOI: 10.1130/G30995.1. eprint: http://geology.gsapubs.org/content/38/9/787.full.pdf+html. URL: http://geology.gsapubs.org/content/38/9/787.abstract.

Aki, K. (1965). "Maximum Likelihood estimate of b in the formula log N=a-bM and its Confidence Limits." In: *Bull. Earthquake Res Inst.,Tokyo Univ.* 43, pp. 237–239.

Altez, Rogelio (2005). "Los sismos del 26 de marzo de 1812 en Venezuela: nuevos aportes y evidencias sobre estos eventos". es. In: *Boletín Técnico* 43, pp. 11 –34. ISSN: 0376-723X. URL: http://www.scielo.org.ve/scielo.php?script=sci_arttext&pid=S0376-723X2005000200002&nrm=iso.

Ambraseys and Jackson (1998). "Faulting associated with historical and recent earthquakes in the Eastern Mediterranean region". In: *Geophysical Journal International* 133.2, pp. 390–406. ISSN: 1365-246X. DOI: 10.1046/j.1365-246X.1998.00508.x. URL: http://dx.doi.org/10.1046/j.1365-246X.1998.00508.x.

Ambraseys, N. N. and J. Douglas (2004). "Magnitude calibration of north Indian earthquakes". In: *Geophysical Journal International* 159.1, pp. 165–206. ISSN: 1365-246X. DOI: 10.1111/j.1365-246X.2004.02323.x. URL: http://dx.doi.org/10.1111/j.1365-246X.2004.02323.x.

Aster, Richard C., Brian Borchers, and Clifford H. Thurber (2013). *Parameter Estimation and Inverse Problems (Second Edition)*. Second Edition. Academic Press. ISBN: 978-0-12-385048-5. DOI: http://dx.doi.org/10.1016/B978-0-12-385048-5.00030-6. URL: http://www.sciencedirect.com/science/article/pii/B9780123850485000306.

Audemard, F. A. (2005). “Paleoseismology in Venezuela: Objectives, methods, applications, limitations and perspectives”. In: *Tectonophysics* 408.1-4. PaleoseismologyIntegrated study of the Quaternary geological record for earthquake deformation and faulting, pp. 29 –61. ISSN: 0040-1951. DOI: http://dx.doi.org/10.1016/j.tecto.2005.05.034. URL: http://www.sciencedirect.com/science/article/pii/S0040195105002751.

Audemard, Franck et al. (1999). “Trench investigation along the Mérida section of the Boconófault (central Venezuelan Andes), Venezuela”. In: *Tectonophysics* 308.1–2, pp. 1–21. DOI: http://dx.doi.org/10.1016/S0040-1951(99)00085-2. URL: http://www.sciencedirect.com/science/article/pii/S0040195199000852.

Audemard, Franck A. (1997). “Holocene and historical earthquakes on the Boconó fault system, southern Venezuelan Andes: Trench confirmation”. In: *Journal of Geodynamics* 24.1-4. Paleoseismology: Understanding Past Earthquakes Using Quaternary Geology, pp. 155 –167. ISSN: 0264-3707. DOI: http://dx.doi.org/10.1016/S0264-3707(96)00037-3. URL: http://www.sciencedirect.com/science/article/pii/S0264370796000373.

Audemard, Franck A. et al. (2008). “Trench investigation on the main strand of the Boconó fault in its central section, at Mesa del Caballo, Mérida Andes, Venezuela”. In: *Tectonophysics* 459.1??4. New Insights into Andean Evolution, pp. 38 –53. ISSN: 0040-1951. DOI: http://dx.doi.org/10.1016/j.tecto.2007.08.020. URL: http://www.sciencedirect.com/science/article/pii/S0040195108001443.

Avouac, J. P. (2003). “Mountain building, erosion and the seismic cycle in the Himalaya”. In: *Advances in geophysics*. Vol. 46. Elsevier. DOI: 10.1016/S0065-2687(03)46001-9.

Avouac, Jean-Philippe (2015). “From Geodetic Imaging of Seismic and Aseismic Fault Slip to Dynamic Modeling of the Seismic Cycle”. In: *Annual Review of Earth and Planetary Sciences* 43.1, null. DOI: 10.1146/annurev-earth-060614-105302. eprint: http://dx.doi.org/10.1146/annurev-earth-060614-105302. URL: http://dx.doi.org/10.1146/annurev-earth-060614-105302.

Avouac, Jean-Philippe et al. (2006). “The 2005, Mw 7.6 Kashmir earthquake: Sub-pixel correlation of ASTER images and seismic waveforms analysis.” In: *Earth and Planetary Science Letters* 249.3-4, pp. 514 –528. ISSN: 0012-821X. DOI: http://dx.doi.org/10.1016/j.epsl.2006.06.025. URL: http://www.sciencedirect.com/science/article/pii/S0012821X06004572.

Bakun, W. H. et al. (2005). “Implications for prediction and hazard assessment from the 2004 Parkfield earthquake”. In: *Nature* 437.7061, pp. 969–974. URL: http://dx.doi.org/10.1038/nature04067.

Bakun, William H. (1999). “Seismic activity of the San Francisco Bay region”. In: *Bulletin of the Seismological Society of America* 89.3, pp. 764–784. eprint: http://www.bssaonline.org/content/89/3/764.full.pdf+html. URL: http://www.bssaonline.org/content/89/3/764.abstract.

Banerjee, P. et al. (2008). “Intraplate deformation of the Indian subcontinent”. In: *Geophysical Research Letters* 35.18, n/a–n/a. ISSN: 1944-8007. DOI: 10.1029/2008GL035468. URL: http://dx.doi.org/10.1029/2008GL035468.

Båth, Markus (1965). “Lateral inhomogeneities of the upper mantle”. In: *Tectonophysics* 2.6, pp. 483 –514. ISSN: 0040-1951. DOI: http://dx.doi.org/10.1016/0040-1951(65)90003-X. URL: http://www.sciencedirect.com/science/article/pii/004019516590003X.

Begin, Z.B. et al. (2005). “A 40,000 year unchanging seismic regime in the Dead Sea rift”. In: *Geology* 33.4, pp. 257–260. DOI: 10.1130/G21115.1. eprint: http://geology.gsapubs.org/content/33/4/257.full.pdf+html. URL: http://geology.gsapubs.org/content/33/4/257.abstract.

Bennett, Richard A., Anke M. Friedrich, and Kevin P. Furlong (2004). “Codependent histories of the San Andreas and San Jacinto fault zones from inversion of fault displacement rates”. In: *Geology* 32.11, pp. 961–964. DOI: 10.1130/G20806.1. eprint: http://geology.gsapubs.org/content/32/11/961.full.pdf+html. URL: http://geology.gsapubs.org/content/32/11/961.abstract.

Berryman, Kelvin R. et al. (2012). “Major Earthquakes Occur Regularly on an Isolated Plate Boundary Fault”. In: *Science* 336.6089, pp. 1690–1693. ISSN: 0036-8075. DOI: 10.1126/science.1218959. eprint: http://science.sciencemag.org/content/336/6089/1690.full.pdf. URL: http://science.sciencemag.org/content/336/6089/1690.

Berthet, Théo et al. (2014). “Active tectonics of the eastern Himalaya: New constraints from the first tectonic geomorphology study in southern Bhutan”. In: *Geology* 42.5, pp. 427–430. DOI: 10.1130/G35162.1. eprint: http://geology.gsapubs.org/content/42/5/427.full.pdf+html. URL: http://geology.gsapubs.org/content/42/5/427.abstract.

Bettinelli, Pierre et al. (2006). “Plate Motion of India and Interseismic Strain in the Nepal Himalaya from GPS and DORIS Measurements”. English. In: *Journal of Geodesy* 80.8-11, pp. 567–589. ISSN: 0949-7714. DOI: 10.1007/s00190-006-0030-3. URL: http://dx.doi.org/10.1007/s00190-006-0030-3.

Bettinelli, Pierre et al. (2008). “Seasonal variations of seismicity and geodetic strain in the Himalaya induced by surface hydrology”. In: *Earth and Planetary Science Letters* 266.3-??4, pp. 332 –344. ISSN: 0012-821X. DOI: http://dx.doi.org/10.1016/j.epsl.2007.11.021. URL: http://www.sciencedirect.com/science/article/pii/S0012821X07007492.

Biasi, Glenn P. and Ray J. Weldon (2006). "Estimating Surface Rupture Length and Magnitude of Paleoearthquakes from Point Measurements of Rupture Displacement". In: *Bulletin of the Seismological Society of America* 96.5, pp. 1612–1623. DOI: 10.1785/0120040172. eprint: http://www.bssaonline.org/content/96/5/1612.full.pdf+html. URL: http://www.bssaonline.org/content/96/5/1612.abstract.

Bilham, R. (2004). "Earthquakes in India and the Himalaya: tectonics, geodesy and history". In: *Annals of Geophysics* 47.2-3. ISSN: 2037-416X. URL: http://www.annalsofgeophysics.eu/index.php/annals/article/view/3338.

Bilham, Roger, Vinod K. Gaur, and Peter Molnar (2001). "Himalayan Seismic Hazard". In: *Science* 293.5534, pp. 1442–1444. DOI: 10.1126/science.1062584. eprint: http://www.sciencemag.org/content/293/5534/1442.full.pdf. URL: http://www.sciencemag.org/content/293/5534/1442.short.

Bilham, Roger, Kristine Larson, and Jeffrey Freymueller (1997). "GPS measurements of present-day convergence across the Nepal Himalaya". In: *Nature* 386, pp. 61–64. URL: http://dx.doi.org/10.1038/386061a0.

Bird, P. et al. (2015). "GEAR1: A Global Earthquake Activity Rate Model Constructed from Geodetic Strain Rates and Smoothed Seismicity". In: *Bulletin of the Seismological Society of America* 105.5, pp. 2538–2554. DOI: 10.1785/0120150058. eprint: http://www.bssaonline.org/content/105/5/2538.full.pdf+html. URL: http://www.bssaonline.org/content/105/5/2538.abstract.

Bird, Peter (2009). "Long-term fault slip rates, distributed deformation rates, and forecast of seismicity in the western United States from joint fitting of community geologic, geodetic, and stress direction data sets". In: *Journal of Geophysical Research: Solid Earth* 114.B11. B11403. ISSN: 2156-2202. DOI: 10.1029/2009JB006317. URL: http://dx.doi.org/10.1029/2009JB006317.

Bird, Peter and Yan Y. Kagan (2004). "Plate-Tectonic Analysis of Shallow Seismicity: Apparent Boundary Width, Beta, Corner Magnitude, Coupled Lithosphere Thickness, and Coupling in Seven Tectonic Settings". In: *Bulletin of the Seismological Society of America* 94.6, pp. 2380–2399. DOI: 10.1785/0120030107. eprint: http://www.bssaonline.org/content/94/6/2380.full.pdf+html. URL: http://www.bssaonline.org/content/94/6/2380.abstract.

Blanpied, Michael L., David A. Lockner, and James D. Byerlee (1995). "Frictional slip of granite at hydrothermal conditions". In: *Journal of Geophysical Research: Solid Earth* 100.B7, pp. 13045–13064. ISSN: 2156-2202. DOI: 10.1029/95JB00862. URL: http://dx.doi.org/10.1029/95JB00862.

Bohnhoff, Marco et al. (2016). "Maximum earthquake magnitudes along different sections of the North Anatolian fault zone". In: *Tectonophysics* 674, pp. 147 – 165. ISSN: 0040-1951. DOI: http://dx.doi.org/10.1016/j.tecto.2016.

02.028. URL: http://www.sciencedirect.com/science/article/pii/S0040195116001256.

Bollinger, L. et al. (2004a). "Stress buildup in the Himalaya". In: *Journal of Geophysical Research: Solid Earth* 109.B11. B11405. ISSN: 2156-2202. DOI: 10.1029/2003JB002911. URL: http://dx.doi.org/10.1029/2003JB002911.

Bollinger, L. et al. (2004b). "Thermal structure and exhumation history of the Lesser Himalaya in central Nepal". In: *Tectonics* 23.5. ISSN: 1944-9194. DOI: 10.1029/2003TC001564.

Bollinger, L. et al. (2014). "Estimating the return times of great Himalayan earthquakes in eastern Nepal: Evidence from the Patu and Bardibas strands of the Main Frontal Thrust". In: *Journal of Geophysical Research: Solid Earth* 119.9, pp. 7123–7163. ISSN: 2169-9356. DOI: 10.1002/2014JB010970.

Brown, Erik T., Peter Molnar, and Didier L. Bourlès (2005). "Comment on Slip-Rate Measurements on the Karakorum Fault May Imply Secular Variations in Fault Motion". In: *Science* 309.5739, p. 1326. DOI: 10.1126/science.1112508.

Brune, James N. (1968). "Seismic moment, seismicity, and rate of slip along major fault zones". In: *Journal of Geophysical Research* 73.2, pp. 777–784. ISSN: 2156-2202. DOI: 10.1029/JB073i002p00777. URL: http://dx.doi.org/10.1029/JB073i002p00777.

Burgess, W. Paul et al. (2012). "Holocene shortening across the Main Frontal Thrust zone in the eastern Himalaya". In: *Earth and Planetary Science Letters* 357358.0, pp. 152 –167. ISSN: 0012-821X. DOI: http://dx.doi.org/10.1016/j.epsl.2012.09.040. URL: http://www.sciencedirect.com/science/article/pii/S0012821X12005365.

Calais, E. et al. (2006). "Continental deformation in Asia from a combined GPS solution". In: *Geophysical Research Letters* 33.24. ISSN: 1944-8007. DOI: 10.1029/2006GL028433. URL: http://dx.doi.org/10.1029/2006GL028433.

California Earthquake Probabilities, Working Group on (1995). "Seismic hazards in Southern California: Probable earthquakes, 1994 to 2024". In: *Bulletin of the Seismological Society of America* 85.2, pp. 379–439. eprint: http://www.bssaonline.org/content/85/2/379.full.pdf+html. URL: http://www.bssaonline.org/content/85/2/379.abstract.

Cattin, R. and J. P. Avouac (2000). "Modeling mountain building and the seismic cycle in the Himalaya of Nepal". In: *Journal of Geophysical Research: Solid Earth* 105.B6, pp. 13389–13407. ISSN: 2156-2202. DOI: 10.1029/2000JB900032.

Cheloni, D., N. D'Agostino, and G. Selvaggi (2014). "Interseismic coupling, seismic potential, and earthquake recurrence on the southern front of the Eastern Alps (NE Italy)". In: *Journal of Geophysical Research: Solid Earth* 119.5, pp. 4448–4468. ISSN: 2169-9356. DOI: 10.1002/2014JB010954. URL: http://dx.doi.org/10.1002/2014JB010954.

Chen, Wang-Ping and Peter Molnar (1977). "Seismic moments of major earthquakes and the average rate of slip in central Asia". In: *Journal of Geophysical Research* 82.20, pp. 2945–2969. ISSN: 2156-2202. DOI: 10.1029/JB082i020p02945. URL: http://dx.doi.org/10.1029/JB082i020p02945.

Chen, WP. and P. Molnar (1990). "Source parameters of earthquakes and intraplate deformation beneath the Shillong Plateau and the Northern Indoburman Ranges". In: *Journal of Geophysical Research: Solid Earth* 95.B8, pp. 12527–12552. ISSN: 2156-2202. DOI: 10.1029/JB095iB08p12527.

Chevalier, M.-L. et al. (2005). "Slip-Rate Measurements on the Karakorum Fault May Imply Secular Variations in Fault Motion". In: *Science* 307.5708, pp. 411–414. ISSN: 0036-8075. DOI: 10.1126/science.1105466. eprint: http://science.sciencemag.org/content/307/5708/411.full.pdf.

Chlieh, M. et al. (2008). "Heterogeneous coupling of the Sumatran megathrust constrained by geodetic and paleogeodetic measurements". In: *Journal of Geophysical Research: Solid Earth* 113.B5. ISSN: 2156-2202. DOI: 10.1029/2007JB004981. URL: http://dx.doi.org/10.1029/2007JB004981.

Chlieh, Mohamed et al. (2011). "Interseismic coupling and seismic potential along the Central Andes subduction zone". In: *Journal of Geophysical Research: Solid Earth* 116.B12. B12405. ISSN: 2156-2202. DOI: 10.1029/2010JB008166. URL: http://dx.doi.org/10.1029/2010JB008166.

Colchen, M (1999). "The ThakkholaMustang graben in Nepal and the late Cenozoic extension in the Higher Himalayas". In: *Journal of Asian Earth Sciences* 17.56, pp. 683 –702. ISSN: 1367-9120. DOI: http://dx.doi.org/10.1016/S1367-9120(99)00037-1. URL: http://www.sciencedirect.com/science/article/pii/S1367912099000371.

Console, Rodolfo et al. (2003). "Båth's Law and the self-similarity of earthquakes". In: *Journal of Geophysical Research: Solid Earth* 108.B2.

Cowgill, Eric (2007). "Impact of riser reconstructions on estimation of secular variation in rates of strikeslip faulting: Revisiting the Cherchen River site along the Altyn Tagh Fault, NW China". In: *Earth and Planetary Science Letters* 254.3-4, pp. 239 –255. ISSN: 0012-821X. DOI: 10.1016/j.epsl.2006.09.015. URL: http://www.sciencedirect.com/science/article/pii/S0012821X06006534.

Cowgill, Eric et al. (2009). "Low Quaternary slip rate reconciles geodetic and geologic rates along the Altyn Tagh fault, northwestern Tibet". In: *Geology* 37.7, pp. 647–650. DOI: 10.1130/G25623A.1. eprint: http://geology.gsapubs.org/content/37/7/647.full.pdf+html. URL: http://geology.gsapubs.org/content/37/7/647.abstract.

Delescluse, Matthias and Nicolas Chamot-Rooke (2007). "Instantaneous deformation and kinematics of the India-Australia Plate". In: *Geophysical Journal International* 168.2, pp. 818–842. DOI: 10.1111/j.1365-246X.2006.03181.x.

eprint: http://gji.oxfordjournals.org/content/168/2/818.full.pdf+html. URL: http://gji.oxfordjournals.org/content/168/2/818.abstract.

DeMets, Charles, Richard G. Gordon, and Donald F. Argus (2010). "Geologically current plate motions". In: *Geophysical Journal International* 181.1, pp. 1–80. DOI: 10.1111/j.1365-246X.2009.04491.x. eprint: http://gji.oxfordjournals.org/content/181/1/1.full.pdf+html. URL: http://gji.oxfordjournals.org/content/181/1/1.abstract.

Dolan, James F., David D. Bowman, and Charles G. Sammis (2007). "Long-range and long-term fault interactions in Southern California". In: *Geology* 35.9, pp. 855–858. DOI: 10.1130/G23789A.1.

Dziewonski, A. M., T.-A. Chou, and J. H. Woodhouse (1981). "Determination of earthquake source parameters from waveform data for studies of global and regional seismicity". In: *Journal of Geophysical Research: Solid Earth* 86.B4, pp. 2825–2852. ISSN: 2156-2202. DOI: 10.1029/JB086iB04p02825. URL: http://dx.doi.org/10.1029/JB086iB04p02825.

Ekström, G., M. Nettles, and A.M. Dziewoñski (2012). "The global CMT project 2004-2010: Centroid-moment tensors for 13,017 earthquakes". In: *Physics of the Earth and Planetary Interiors* 200-201, pp. 1 –9. ISSN: 0031-9201. DOI: http://dx.doi.org/10.1016/j.pepi.2012.04.002. URL: http://www.sciencedirect.com/science/article/pii/S0031920112000696.

Elliott, J. R. et al. (2008). "InSAR slip rate determination on the Altyn Tagh Fault, northern Tibet, in the presence of topographically correlated atmospheric delays". In: *Geophysical Research Letters* 35.12. L12309. ISSN: 1944-8007. DOI: 10.1029/2008GL033659. URL: http://dx.doi.org/10.1029/2008GL033659.

England, P. and P. Molnar (1997a). "Active Deformation of Asia: From Kinematics to Dynamics". In: *Science* 278.5338, pp. 647–650. DOI: 10.1126/science.278.5338.647. eprint: http://www.sciencemag.org/content/278/5338/647.full.pdf. URL: http://www.sciencemag.org/content/278/5338/647.abstract.

– (1997b). "The field of crustal velocity in Asia calculated from Quaternary rates of slip on faults". In: *Geophysical Journal International* 130.3, pp. 551–582. ISSN: 1365-246X. DOI: 10.1111/j.1365-246X.1997.tb01853.x.

England, Philip and Peter Molnar (2005). "Late Quaternary to decadal velocity fields in Asia". In: *J. Geophys. Res.* 110.B12, B12401–. ISSN: 0148-0227. URL: http://dx.doi.org/10.1029/2004JB003541.

Felzer, K. R. (2006). "Calculating the Gutenberg-Richter b value". In: *Eos Trans. AGU* 87(52).

Felzer, Karen R (2008). *Calculating California seismicity rates*. Tech. rep. Geological Survey (US).

Felzer, Karen R., Rachel E. Abercrombie, and Gran Ekström (2004). "A Common Origin for Aftershocks, Foreshocks, and Multiplets". In: *Bulletin of the Seismological Society of America* 94.1, pp. 88–98. DOI: 10.1785/0120030069. eprint: http://www.bssaonline.org/content/94/1/88.full.pdf+html. URL: http://www.bssaonline.org/content/94/1/88.abstract.

Felzer, Karen R. et al. (2002). "Triggering of the 1999 MW 7.1 Hector Mine earthquake by aftershocks of the 1992 MW 7.3 Landers earthquake". In: *Journal of Geophysical Research: Solid Earth* 107.B9. 2190, pp. 6–13. ISSN: 2156-2202. DOI: 10.1029/2001JB000911. URL: http://dx.doi.org/10.1029/2001JB000911.

Field, Edward H., David D. Jackson, and James F. Dolan (1999). "A mutually consistent seismic-hazard source model for southern California". In: *Bulletin of the Seismological Society of America* 89.3, pp. 559–578. eprint: http://www.bssaonline.org/content/89/3/559.full.pdf+html. URL: http://www.bssaonline.org/content/89/3/559.abstract.

Field, Edward H. and Morgan T. Page (2011). "Estimating Earthquake-Rupture Rates on a Fault or Fault System". In: *Bulletin of the Seismological Society of America* 101.1, pp. 79–92. DOI: 10.1785/0120100004. eprint: http://www.bssaonline.org/content/101/1/79.full.pdf+html. URL: http://www.bssaonline.org/content/101/1/79.abstract.

Field, Edward H. et al. (2014). "Uniform California Earthquake Rupture Forecast, Version 3 (UCERF3) - The Time-Independent Model". In: *Bulletin of the Seismological Society of America* 104.3, pp. 1122–1180. DOI: 10.1785/0120130164. eprint: http://www.bssaonline.org/content/104/3/1122.full.pdf+html. URL: http://www.bssaonline.org/content/104/3/1122.abstract.

Freed, Andrew M., Syed Tabrez Ali, and Roland Bürgmann (2007). "Evolution of stress in Southern California for the past 200 years from coseismic, postseismic and interseismic stress changes". In: *Geophysical Journal International* 169.3, pp. 1164–1179. DOI: 10.1111/j.1365-246X.2007.03391.x. eprint: http://gji.oxfordjournals.org/content/169/3/1164.full.pdf+html. URL: http://gji.oxfordjournals.org/content/169/3/1164.abstract.

Friedrich, A. M. et al. (2004). "Geologic context of geodetic data across a Basin and Range normal fault, Crescent Valley, Nevada". In: *Tectonics* 23.2. TC2015, n/a–n/a. ISSN: 1944-9194. DOI: 10.1029/2003TC001528. URL: http://dx.doi.org/10.1029/2003TC001528.

Gahalaut, Vineet K et al. (2013). "Aseismic plate boundary in the Indo-Burmese wedge, northwest Sunda Arc". In: *Geology*. DOI: 10.1130/G33771.1. eprint: http://geology.gsapubs.org/content/early/2013/01/04/G33771.1.full.pdf+html. URL: http://geology.gsapubs.org/content/early/2013/01/04/G33771.1.abstract.

Galetzka, J. et al. (2015). "Slip pulse and resonance of the Kathmandu basin during the 2015 Gorkha earthquake, Nepal". In: *Science* 349.6252, pp. 1091–1095. ISSN: 0036-8075. DOI: 10.1126/science.aac6383. eprint: http://science.sciencemag.org/content/349/6252/1091.full.pdf. URL: http://science.sciencemag.org/content/349/6252/1091.

Gan, Weijun et al. (2007). "Present-day crustal motion within the Tibetan Plateau inferred from GPS measurements". In: *J. Geophys. Res.* 112.B8, B08416–. ISSN: 0148-0227. URL: http://dx.doi.org/10.1029/2005JB004120.

Ganev, Plamen N. et al. (2012). "Constancy of geologic slip rate along the central Garlock fault: implications for strain accumulation and release in southern California". In: *Geophysical Journal International* 190.2, pp. 745–760. DOI: 10.1111/j.1365-246X.2012.05494.x. eprint: http://gji.oxfordjournals.org/content/190/2/745.full.pdf+html. URL: http://gji.oxfordjournals.org/content/190/2/745.abstract.

Garfunkel, Z., I. Zak, and R. Freund (1981). "The Dead Sea Rift Active faulting in the dead sea rift". In: *Tectonophysics* 80.1, pp. 1 –26. ISSN: 0040-1951. DOI: http://dx.doi.org/10.1016/0040-1951(81)90139-6. URL: http://www.sciencedirect.com/science/article/pii/0040195181901396.

Geller, Robert J., Francesco Mulargia, and Philip B. Stark (2015). "Why We Need a New Paradigm of Earthquake Occurrence". In: *Subduction Dynamics*. John Wiley & Sons, Inc, pp. 183–191. ISBN: 9781118888865. DOI: 10.1002/9781118888865.ch10. URL: http://dx.doi.org/10.1002/9781118888865.ch10.

Godano, C., E. Lippiello, and L. de Arcangelis (2014). "Variability of the b value in the Gutenberg-Richter distribution". In: *Geophysical Journal International* 199.3, pp. 1765–1771. DOI: 10.1093/gji/ggu359. eprint: http://gji.oxfordjournals.org/content/199/3/1765.full.pdf+html. URL: http://gji.oxfordjournals.org/content/199/3/1765.abstract.

Godard, V., J. Lavé, and R. Cattin (2006). "Numerical modelling of erosion processes in the Himalayas of Nepal: effects of spatial variations of rock strength and precipitation". In: *Geological Society, London, Special Publications* 253.1, pp. 341–358. DOI: 10.1144/GSL.SP.2006.253.01.18. eprint: http://sp.lyellcollection.org/content/253/1/341.full.pdf+html. URL: http://sp.lyellcollection.org/content/253/1/341.abstract.

Grandin, Raphaël et al. (2012). "Long-term growth of the Himalaya inferred from interseismic InSAR measurement". In: *Geology*. DOI: 10.1130/G33154.1. eprint: http://geology.gsapubs.org/content/early/2012/09/18/G33154.1.full.pdf+html. URL: http://geology.gsapubs.org/content/early/2012/09/18/G33154.1.abstract.

Grunewald, Elliot D. and Ross S. Stein (2006). "A new 1649-1884 catalog of destructive earthquakes near Tokyo and implications for the long-term seismic process". In: *Journal of Geophysical Research: Solid Earth* 111.B12. B12306. ISSN: 2156-2202. DOI: 10.1029/2005JB004059. URL: http://dx.doi.org/10.1029/2005JB004059.

Guo, Zhenqi and Yosihiko Ogata (1997). "Statistical relations between the parameters of aftershocks in time, space, and magnitude". In: *Journal of Geophysical Research: Solid Earth* 102.B2, pp. 2857–2873. ISSN: 2156-2202. DOI: 10.1029/96JB02946. URL: http://dx.doi.org/10.1029/96JB02946.

Gupta, Tanay Dutta et al. (2015). "Kinematics and strain rates of the Eastern Himalayan Syntaxis from new {GPS} campaigns in Northeast India". In: *Tectonophysics* 655, pp. 15 –26. ISSN: 0040-1951. DOI: http://dx.doi.org/10.1016/j.tecto.2015.04.017. URL: http://www.sciencedirect.com/science/article/pii/S0040195115002425.

Gutenberg, Beno and Charles F Richter (1944). "Frequency of earthquakes in California". In: *Bulletin of the Seismological Society of America* 34.4, pp. 185–188.

Haines, A. J. and W. E. Holt (1993). "A procedure for obtaining the complete horizontal motions within zones of distributed deformation from the inversion of strain rate data". In: *Journal of Geophysical Research: Solid Earth* 98.B7, pp. 12057–12082. ISSN: 2156-2202. DOI: 10.1029/93JB00892. URL: http://dx.doi.org/10.1029/93JB00892.

Hartleb, Ross D. et al. (2006). "A 2500-yr-long paleoseismologic record of large, infrequent earthquakes on the North Anatolian fault at Çukurçimen, Turkey". In: *Geological Society of America Bulletin* 118.7-8, pp. 823–840. DOI: 10.1130/B25838.1. eprint: http://gsabulletin.gsapubs.org/content/118/7-8/823.full.pdf+html. URL: http://gsabulletin.gsapubs.org/content/118/7-8/823.abstract.

Helmstetter, Agn, Yan Y. Kagan, and David D. Jackson (2005). "Importance of small earthquakes for stress transfers and earthquake triggering". In: *Journal of Geophysical Research: Solid Earth* 110.B5. ISSN: 2156-2202. DOI: 10.1029/2004JB003286. URL: http://dx.doi.org/10.1029/2004JB003286.

Herman, Frédéric et al. (2010). "Exhumation, crustal deformation, and thermal structure of the Nepal Himalaya derived from the inversion of thermochronological and thermobarometric data and modeling of the topography". In: *Journal of Geophysical Research: Solid Earth* 115.B6. B06407. ISSN: 2156-2202. DOI: 10.1029/2008JB006126. URL: http://dx.doi.org/10.1029/2008JB006126.

Herring, T. (2010). *Geodesy: treatise on geophysics*. Elsevier.

Holschneider, Matthias, Gert Zöller, and Sebastian Hainzl (2011). "Estimation of the Maximum Possible Magnitude in the Framework of a Doubly Truncated Gutenberg-Richter Model". In: *Bulletin of the Seismological Society of America* 101.4, pp. 1649–1659. DOI: 10.1785/0120100289. eprint: http://www.

bssaonline.org/content/101/4/1649.full.pdf+html. URL: http://www.bssaonline.org/content/101/4/1649.abstract.

Holt, W. E. et al. (2000). "Velocity field in Asia inferred from Quaternary fault slip rates and Global Positioning System observations". In: *J. Geophys. Res.* 105.B8, pp. 19185–19209. ISSN: 0148-0227. URL: http://dx.doi.org/10.1029/2000JB900045.

Holt, William E., Ming Li, and A. J. Haines (1995). "Earthquake strain rates and instantaneous relative motions within central and eastern Asia". In: *Geophysical Journal International* 122.2, pp. 569–593. DOI: 10.1111/j.1365-246X.1995.tb07014.x. eprint: http://gji.oxfordjournals.org/content/122/2/569.full.pdf+html. URL: http://gji.oxfordjournals.org/content/122/2/569.abstract.

Hsu, Ya-Ju et al. (2006). "Frictional Afterslip Following the 2005 Nias-Simeulue Earthquake, Sumatra". In: *Science* 312.5782, pp. 1921–1926. ISSN: 0036-8075. DOI: 10.1126/science.1126960. eprint: http://science.sciencemag.org/content/312/5782/1921.full.pdf. URL: http://science.sciencemag.org/content/312/5782/1921.

Hurtado, Jos., Kip V. Hodges, and Kelin X Whipple (2001). "Neotectonics of the Thakkhola graben and implications for recent activity on the South Tibetan fault system in the central Nepal Himalaya". In: *Geological Society of America Bulletin* 113.2, pp. 222 –240. DOI: 10.1130/0016-7606(2001)113<0222:NOTTGA>2.0.CO;2. eprint: http://gsabulletin.gsapubs.org/content/113/2/222.full.pdf+html. URL: http://gsabulletin.gsapubs.org/content/113/2/222.abstract.

Hutton, Kate, Jochen Woessner, and Egill Hauksson (2010). "Earthquake Monitoring in Southern California for Seventy-Seven Years (1932-2008)". In: *Bulletin of the Seismological Society of America* 100.2, pp. 423–446. DOI: 10.1785/0120090130. eprint: http://www.bssaonline.org/content/100/2/423.full.pdf+html. URL: http://www.bssaonline.org/content/100/2/423.abstract.

International Seismological Centre (2013). *On-line Bulletin*. http://www.isc.ac.uk. Int. Seis. Cent. Thatcham, United Kingdom.

Ischuk, Anatoli et al. (2013). "Kinematics of the Pamir and Hindu Kush regions from GPS geodesy". In: *Journal of Geophysical Research: Solid Earth* 118.5, pp. 2408–2416. ISSN: 2169-9356. DOI: 10.1002/jgrb.50185. URL: http://dx.doi.org/10.1002/jgrb.50185.

Ishibe, Takeo and Kunihiko Shimazaki (2012). "Characteristic Earthquake Model and Seismicity around Late Quaternary Active Faults in Japan". In: *Bulletin of the Seismological Society of America* 102.3, pp. 1041–1058. DOI: 10.1785/0120100250. eprint: http://www.bssaonline.org/content/102/3/

1041.full.pdf+html. URL: http://www.bssaonline.org/content/102/3/1041.abstract.

Ishimura, Daisuke and Takahiro Miyauchi (2015). "Historical and paleo-tsunami deposits during the last 4000 years and their correlations with historical tsunami events in Koyadori on the Sanriku Coast, northeastern Japan". In: *Progress in Earth and Planetary Science* 2.1, pp. 1–18. ISSN: 2197-4284. DOI: 10.1186/s40645-015-0047-4. URL: http://dx.doi.org/10.1186/s40645-015-0047-4.

Jackson, Michael and Roger Bilham (1994). "Constraints on Himalayan deformation inferred from vertical velocity fields in Nepal and Tibet". In: *Journal of Geophysical Research: Solid Earth* 99.B7, pp. 13897–13912. ISSN: 2156-2202. DOI: 10.1029/94JB00714. URL: http://dx.doi.org/10.1029/94JB00714.

Jade, Sridevi et al. (2007). "Estimates of interseismic deformation in Northeast India from GPS measurements". In: *Earth and Planetary Science Letters* 263.34, pp. 221 –234. ISSN: 0012-821X. DOI: http://dx.doi.org/10.1016/j.epsl.2007.08.031. URL: http://www.sciencedirect.com/science/article/pii/S0012821X0700550X.

Jade, Sridevi et al. (2011). "GPS-derived deformation rates in northwestern Himalaya and Ladakh". English. In: *International Journal of Earth Sciences* 100.6, pp. 1293–1301. ISSN: 1437-3254. DOI: 10.1007/s00531-010-0532-3. URL: http://dx.doi.org/10.1007/s00531-010-0532-3.

Jade, Sridevi et al. (2014). "Contemporary deformation in the KashmirHimachal, Garhwal and Kumaon Himalaya: significant insights from 19952008 GPS time series". English. In: *Journal of Geodesy* 88.6, pp. 539–557. ISSN: 0949-7714. DOI: 10.1007/s00190-014-0702-3. URL: http://dx.doi.org/10.1007/s00190-014-0702-3.

Jouanne, F. et al. (2004). "Current shortening across the Himalayas of Nepal". In: *Geophysical Journal International* 157.1, pp. 1–14. DOI: 10.1111/j.1365-246X.2004.02180.x. eprint: http://gji.oxfordjournals.org/content/157/1/1.full.pdf+html. URL: http://gji.oxfordjournals.org/content/157/1/1.abstract.

Jouanne, F. et al. (2011). "Postseismic deformation in Pakistan after the 8 October 2005 earthquake: Evidence of afterslip along a flat north of the Balakot-Bagh thrust". In: *Journal of Geophysical Research: Solid Earth* 116.B7. ISSN: 2156-2202. DOI: 10.1029/2010JB007903. URL: http://dx.doi.org/10.1029/2010JB007903.

Jouanne, F. et al. (2014). "Present-day deformation of northern Pakistan from Salt Ranges to Karakorum Ranges". In: *Journal of Geophysical Research: Solid Earth* 119.3, pp. 2487–2503. ISSN: 2169-9356. DOI: 10.1002/2013JB010776. URL: http://dx.doi.org/10.1002/2013JB010776.

Kagan, Y. Y. (1997). "Seismic moment-frequency relation for shallow earthquakes: Regional comparison". In: *Journal of Geophysical Research: Solid Earth* 102.B2, pp. 2835–2852. ISSN: 2156-2202. DOI: 10.1029/96JB03386. URL: http://dx.doi.org/10.1029/96JB03386.

– (1999). "Seismicity Patterns, their Statistical Significance and Physical Meaning". In: ed. by Max Wyss, Kunihiko Shimazaki, and Akihiko Ito. Basel: Birkhäuser Basel. Chap. Universality of the Seismic Moment-frequency Relation, pp. 537–573. ISBN: 978-3-0348-8677-2. URL: http://dx.doi.org/10.1007/978-3-0348-8677-2_16.

Kagan, Yan Y. (2002a). "Seismic moment distribution revisited: I. Statistical results". In: *Geophysical Journal International* 148.3, pp. 520–541. ISSN: 1365-246X. DOI: 10.1046/j.1365-246x.2002.01594.x. URL: http://dx.doi.org/10.1046/j.1365-246x.2002.01594.x.

– (2002b). "Seismic moment distribution revisited: II Moment conservation principle". In: *Geophysical Journal International* 149.3, pp. 731–754. ISSN: 1365-246X. DOI: 10.1046/j.1365-246X.2002.01671.x. URL: http://dx.doi.org/10.1046/j.1365-246X.2002.01671.x.

Kagan, Yan Y. and David D. Jackson (2012). "Whole Earth high-resolution earthquake forecasts". In: *Geophysical Journal International* 190.1, pp. 677–686. ISSN: 1365-246X. DOI: 10.1111/j.1365-246X.2012.05521.x. URL: http://dx.doi.org/10.1111/j.1365-246X.2012.05521.x.

– (2013). "Tohoku Earthquake: A Surprise?" In: *Bulletin of the Seismological Society of America* 103.2B, pp. 1181–1194. DOI: 10.1785/0120120110. eprint: http://www.bssaonline.org/content/103/2B/1181.full.pdf+html. URL: http://www.bssaonline.org/content/103/2B/1181.abstract.

Kagan, Y.Y. (1993). "Statistics of Characteristic Earthquakes". In: *Bulletin of the Seismological Society of America* 83, pp. 7–24.

Kanamori, Hiroo and Emily E Brodsky (2004). "The physics of earthquakes". In: *Reports on Progress in Physics* 67.8, p. 1429.

Kenner, Shelley J. and Mark Simons (2005). "Temporal clustering of major earthquakes along individual faults due to post-seismic reloading". In: *Geophysical Journal International* 160.1, pp. 179–194. DOI: 10.1111/j.1365-246X.2005.02460.x. eprint: http://gji.oxfordjournals.org/content/160/1/179.full.pdf+html. URL: http://gji.oxfordjournals.org/content/160/1/179.abstract.

Kijko, A. and G. Graham (1998). "Parametric-historic Procedure for Probabilistic Seismic Hazard Analysis Part I: Estimation of Maximum Regional Magnitude M_{max}". In: *pure and applied geophysics* 152.3, pp. 413–442. ISSN: 1420-9136. DOI: 10.1007/s000240050161. URL: http://dx.doi.org/10.1007/s000240050161.

Kijko, Andrzej (2004). "Estimation of the Maximum Earthquake Magnitude, M_max". In: *Pure and Applied Geophysics* 161.8, pp. 1655–1681. ISSN: 1420-9136. DOI: 10.1007/s00024-004-2531-4. URL: http://dx.doi.org/10.1007/s00024-004-2531-4.

Klinger, Y., M. Le Béon, and M. Al-Qaryouti (2015). "5000 yr of paleoseismicity along the southern Dead Sea fault". In: *Geophysical Journal International* 202.1, pp. 313–327. DOI: 10.1093/gji/ggv134. eprint: http://gji.oxfordjournals.org/content/202/1/313.full.pdf+html. URL: http://gji.oxfordjournals.org/content/202/1/313.abstract.

Klinger, Y. et al. (2000). "Slip rate on the Dead Sea transform fault in northern Araba valley (Jordan)". In: *Geophysical Journal International* 142.3, pp. 755–768. DOI: 10.1046/j.1365-246x.2000.00165.x. eprint: http://gji.oxfordjournals.org/content/142/3/755.full.pdf+html. URL: http://gji.oxfordjournals.org/content/142/3/755.abstract.

Klinger, Y. et al. (2003). "Paleoseismic Evidence of Characteristic Slip on the Western Segment of the North Anatolian Fault, Turkey". In: *Bulletin of the Seismological Society of America* 93.6, pp. 2317–2332. DOI: 10.1785/0120010270. eprint: http://www.bssaonline.org/content/93/6/2317.full.pdf+html. URL: http://www.bssaonline.org/content/93/6/2317.abstract.

Kohlstedt, D. L., Brian Evans, and S. J. Mackwell (1995). "Strength of the lithosphere: Constraints imposed by laboratory experiments". In: *Journal of Geophysical Research: Solid Earth* 100.B9, pp. 17587–17602. ISSN: 2156-2202. DOI: 10.1029/95JB01460. URL: http://dx.doi.org/10.1029/95JB01460.

Kostrov, V. (1974). "Seismic moment and energy of earthquakes, and seismic flow of rock". In: *Physics of the Solid Earth* 1, pp. 13 –21.

Kozaci, Özgür et al. (2007). "Late Holocene slip rate for the North Anatolian fault, Turkey, from cosmogenic 36Cl geochronology: Implications for the constancy of fault loading and strain release rates". In: *Geology* 35.10, pp. 867–870. DOI: 10.1130/G23187A.1. eprint: http://geology.gsapubs.org/content/35/10/867.full.pdf+html. URL: http://geology.gsapubs.org/content/35/10/867.abstract.

Kumar, Senthil et al. (2006). "Paleoseismic evidence of great surface rupture earthquakes along the Indian Himalaya". In: *Journal of Geophysical Research: Solid Earth* 111.B3. ISSN: 2156-2202. DOI: 10.1029/2004JB003309. URL: http://dx.doi.org/10.1029/2004JB003309.

Kumar, Senthil et al. (2010). "Paleoseismological evidence of surface faulting along the northeastern Himalayan front, India: Timing, size, and spatial extent of great earthquakes". In: *Journal of Geophysical Research: Solid Earth* 115.B12. B12422. ISSN: 2156-2202. DOI: 10.1029/2009JB006789. URL: http://dx.doi.org/10.1029/2009JB006789.

Kundu, Bhaskar et al. (2014). "Oblique convergence and slip partitioning in the NW Himalaya: Implications from GPS measurements". In: *Tectonics* 33.10, pp. 2013–2024. ISSN: 1944-9194. DOI: 10.1002/2014TC003633. URL: http://dx.doi.org/10.1002/2014TC003633.

Lapusta, Nadia and Yi Liu (2009). "Three-dimensional boundary integral modeling of spontaneous earthquake sequences and aseismic slip". In: *Journal of Geophysical Research: Solid Earth* 114.B9. ISSN: 2156-2202. DOI: 10.1029/2008JB005934. URL: http://dx.doi.org/10.1029/2008JB005934.

Lapusta, Nadia and James R. Rice (2003). "Nucleation and early seismic propagation of small and large events in a crustal earthquake model". In: *Journal of Geophysical Research: Solid Earth* 108.B4. 2205, n/a–n/a. ISSN: 2156-2202. DOI: 10.1029/2001JB000793. URL: http://dx.doi.org/10.1029/2001JB000793.

Larson, Kristine M. et al. (1999). "Kinematics of the India-Eurasia collision zone from GPS measurements". In: *Journal of Geophysical Research: Solid Earth* 104.B1, pp. 1077–1093. ISSN: 2156-2202. DOI: 10.1029/1998JB900043. URL: http://dx.doi.org/10.1029/1998JB900043.

Lavé, J. and J. P. Avouac (2000). "Active folding of fluvial terraces across the Siwaliks Hills, Himalayas of central Nepal". In: *Journal of Geophysical Research: Solid Earth* 105.B3, pp. 5735–5770. ISSN: 2156-2202. DOI: 10.1029/1999JB900292. URL: http://dx.doi.org/10.1029/1999JB900292.

– (2001). "Fluvial incision and tectonic uplift across the Himalayas of central Nepal". In: *J. Geophys. Res.* 106.B11, pp. 26561–26591. ISSN: 0148-0227. URL: http://dx.doi.org/10.1029/2001JB000359.

Lavé, J. et al. (2005). "Evidence for a Great Medieval Earthquake (~1100 A.D.) in the Central Himalayas, Nepal". In: *Science* 307.5713, pp. 1302–1305. DOI: 10.1126/science.1104804. eprint: http://www.sciencemag.org/content/307/5713/1302.full.pdf. URL: http://www.sciencemag.org/content/307/5713/1302.abstract.

Le Beon, Maryline et al. (2008). "Slip rate and locking depth from GPS profiles across the southern Dead Sea Transform". In: *Journal of Geophysical Research: Solid Earth* 113.B11. B11403. ISSN: 2156-2202. DOI: 10.1029/2007JB005280. URL: http://dx.doi.org/10.1029/2007JB005280.

Li, Shaoyang et al. (2015). "Revisiting viscoelastic effects on interseismic deformation and locking degree: A case study of the Peru-North Chile subduction zone". In: *Journal of Geophysical Research: Solid Earth* 120.6. 2015JB011903, pp. 4522–4538. ISSN: 2169-9356. DOI: 10.1002/2015JB011903. URL: http://dx.doi.org/10.1002/2015JB011903.

Liang, Shiming et al. (2013). "Three-dimensional velocity field of present-day crustal motion of the Tibetan Plateau derived from GPS measurements". In: *Journal of Geophysical Research: Solid Earth*. ISSN: 2169-9356. DOI: 10.1002/2013JB010503. URL: http://dx.doi.org/10.1002/2013JB010503.

Lin, Yu-nung Nina et al. (2013). "Coseismic and postseismic slip associated with the 2010 Maule Earthquake, Chile: Characterizing the Arauco Peninsula barrier effect". In: *Journal of Geophysical Research: Solid Earth* 118.6, pp. 3142–3159. ISSN: 2169-9356. DOI: 10.1002/jgrb.50207. URL: http://dx.doi.org/10.1002/jgrb.50207.

Liu, Zhen et al. (2010). "Estimation of interplate coupling in the Nankai trough, Japan using GPS data from 1996 to 2006". In: *Geophysical Journal International* 181.3, pp. 1313–1328. DOI: 10.1111/j.1365-246X.2010.04600.x. eprint: http://gji.oxfordjournals.org/content/181/3/1313.full.pdf+html. URL: http://gji.oxfordjournals.org/content/181/3/1313.abstract.

Loveless, John P. and Brendan J. Meade (2015). "Kinematic barrier constraints of the magnitudes of additional great earthquakes off the east coast of Japan". In: *Seismological Research Letters* 86.1.

Mahesh, P. et al. (2012). "Rigid Indian plate: Constraints from {GPS} measurements". In: *Gondwana Research* 22.34, pp. 1068 –1072. ISSN: 1342-937X. DOI: http://dx.doi.org/10.1016/j.gr.2012.01.011. URL: http://www.sciencedirect.com/science/article/pii/S1342937X12000421.

Mahesh, P. et al. (2013). "One?Dimensional Reference Velocity Model and Precise Locations of Earthquake Hypocenters in the KumaonGarhwal Himalaya". In: *Bulletin of the Seismological Society of America* 103.1, pp. 328–339. DOI: 10.1785/0120110328. eprint: http://www.bssaonline.org/content/103/1/328.full.pdf+html. URL: http://www.bssaonline.org/content/103/1/328.abstract.

Main, Ian G. et al. (2008). "Effect of the Sumatran mega-earthquake on the global magnitude cut-off and event rate". In: *Nature Geosci* 1.3, pp. 142–142. URL: http://dx.doi.org/10.1038/ngeo141.

Marco, Shmuel and Amotz Agnon (1995). "Prehistoric earthquake deformations near Masada, Dead Sea graben". In: *Geology* 23.8, pp. 695–698. eprint: http://geology.gsapubs.org/content/23/8/695.full.pdf+html. URL: http://geology.gsapubs.org/content/23/8/695.abstract.

Marsan, David and Olivier Lengliné (2008). "Extending Earthquakes' Reach Through Cascading". In: *Science* 319.5866, pp. 1076–1079. ISSN: 0036-8075. DOI: 10.1126/science.1148783. eprint: http://science.sciencemag.org/content/319/5866/1076.full.pdf. URL: http://science.sciencemag.org/content/319/5866/1076.

Maurin, Thomas et al. (2010). "First global positioning system results in northern Myanmar: Constant and localized slip rate along the Sagaing fault". In: *Geology* 38.7, pp. 591–594. DOI: 10.1130/G30872.1. eprint: http://geology.gsapubs.org/content/38/7/591.full.pdf+html. URL: http://geology.gsapubs.org/content/38/7/591.abstract.

McCaffrey, Robert (2008). "Global frequency of magnitude 9 earthquakes". In: *Geology* 36.3, pp. 263–266. DOI: 10.1130/G24402A.1. eprint: http://geology.gsapubs.org/content/36/3/263.full.pdf+html. URL: http://geology.gsapubs.org/content/36/3/263.abstract.

Meade, Brendan J. (2010). "The signature of an unbalanced earthquake cycle in Himalayan topography?" In: *Geology* 38.11, pp. 987–990. DOI: 10.1130/G31439.1. eprint: http://geology.gsapubs.org/content/38/11/987.full.pdf+html. URL: http://geology.gsapubs.org/content/38/11/987.abstract.

Meade, Brendan J. and Bradford H. Hager (2005). "Block models of crustal motion in southern California constrained by GPS measurements". In: *Journal of Geophysical Research: Solid Earth* 110.B3. B03403. ISSN: 2156-2202. DOI: 10.1029/2004JB003209. URL: http://dx.doi.org/10.1029/2004JB003209.

Meade, Brendan J., Yann Klinger, and Eric A. Hetland (2013). "Inference of Multiple Earthquake Cycle Relaxation Timescales from Irregular Geodetic Sampling of Interseismic Deformation". In: *Bulletin of the Seismological Society of America* 103.5, pp. 2824–2835. DOI: 10.1785/0120130006. eprint: http://www.bssaonline.org/content/103/5/2824.full.pdf+html. URL: http://www.bssaonline.org/content/103/5/2824.abstract.

Meghraoui, Mustapha (2014). "Encyclopedia of Earthquake Engineering". In: ed. by Michael Beer et al. Berlin, Heidelberg: Springer Berlin Heidelberg. Chap. Paleoseismic History of the Dead Sea Fault Zone, pp. 1–20. ISBN: 978-3-642-36197-5. DOI: 10.1007/978-3-642-36197-540-1. URL: http://dx.doi.org/10.1007/978-3-642-36197-540-1.

Mériaux, A.-S. et al. (2004). "Rapid slip along the central Altyn Tagh Fault: Morphochronologic evidence from Cherchen He and Sulamu Tagh". In: *Journal of Geophysical Research: Solid Earth* 109.B6. B06401. ISSN: 2156-2202. DOI: 10.1029/2003JB002558. URL: http://dx.doi.org/10.1029/2003JB002558.

Métois, M., A. Socquet, and C. Vigny (2012). "Interseismic coupling, segmentation and mechanical behavior of the central Chile subduction zone". In: *Journal of Geophysical Research: Solid Earth* 117.B3. B03406, n/a–n/a. ISSN: 2156-2202. DOI: 10.1029/2011JB008736. URL: http://dx.doi.org/10.1029/2011JB008736.

Michael, Andrew J. (2011). "Random variability explains apparent global clustering of large earthquakes". In: *Geophysical Research Letters* 38.21. L21301. ISSN: 1944-8007. DOI: 10.1029/2011GL049443. URL: http://dx.doi.org/10.1029/2011GL049443.

Minoura, K. et al. (2001). "The 869 Jogan tsunami deposit and recurrence interval of large-scale tsunami on the Pacific coast of northeast Japan". In: *Journal of Natural Disaster Science* 23.2, pp. 82–88.

Mohadjer, S. et al. (2010). "Partitioning of India-Eurasia convergence in the Pamir-Hindu Kush from GPS measurements". In: *Geophysical Research Letters* 37.4. ISSN: 1944-8007. DOI: 10.1029/2009GL041737. URL: http://dx.doi.org/10.1029/2009GL041737.

Molnar, P (1984). "Structure and Tectonics of the Himalaya: Constraints and Implications of Geophysical Data". In: *Annual Review of Earth and Planetary Sciences* 12.1, pp. 489–516. DOI: 10.1146/annurev.ea.12.050184.002421. eprint: http://dx.doi.org/10.1146/annurev.ea.12.050184.002421. URL: http://dx.doi.org/10.1146/annurev.ea.12.050184.002421.

Molnar, Peter (1979). "Earthquake recurrence intervals and plate tectonics". In: *Bulletin of the Seismological Society of America* 69.1, pp. 115–133. eprint: http://www.bssaonline.org/content/69/1/115.full.pdf+html. URL: http://www.bssaonline.org/content/69/1/115.abstract.

Moreno, M. et al. (2011). "Heterogeneous plate locking in the SouthCentral Chile subduction zone: Building up the next great earthquake". In: *Earth and Planetary Science Letters* 305.34, pp. 413 –424. ISSN: 0012-821X. DOI: http://dx.doi.org/10.1016/j.epsl.2011.03.025. URL: http://www.sciencedirect.com/science/article/pii/S0012821X11001695.

Mugnier, J. et al. (2003). "Episodicity and rates of thrust-sheet motion in the Himalayas (western Nepal)". In: *AAPG Mem.* 82, pp. 1–24.

Mugnier, J.-L. et al. (2013). "Structural interpretation of the great earthquakes of the last millennium in the central Himalaya". In: *Earth-Science Reviews* 127.0, pp. 30 –47. ISSN: 0012-8252. DOI: http://dx.doi.org/10.1016/j.earscirev.2013.09.003. URL: http://www.sciencedirect.com/science/article/pii/S0012825213001529.

Mugnier, J.L. et al. (2011). "Seismites in the Kathmandu basin and seismic hazard in central Himalaya". In: *Tectonophysics* 509.12, pp. 33 –49. ISSN: 0040-1951. DOI: http://dx.doi.org/10.1016/j.tecto.2011.05.012. URL: http://www.sciencedirect.com/science/article/pii/S0040195111002137.

Mukul, Malay et al. (2010). "Crustal shortening in convergent orogens: Insights from global positioning system (GPS) measurements in northeast India". English. In: *Journal of the Geological Society of India* 75.1, pp. 302–312. ISSN: 0016-7622. DOI: 10.1007/s12594-010-0017-9. URL: http://dx.doi.org/10.1007/s12594-010-0017-9.

Nanayama, Futoshi et al. (2003). "Unusually large earthquakes inferred from tsunami deposits along the Kuril trench". In: *Nature* 424.6949, pp. 660–663. URL: http://dx.doi.org/10.1038/nature01864.

Naylor, M., I. G. Main, and S. Touati (2009). "Quantifying uncertainty in mean earthquake interevent times for a finite sample". In: *Journal of Geophysical Research: Solid Earth* 114.B1. B01316. ISSN: 2156-2202. DOI: 10.1029/2008JB005870. URL: http://dx.doi.org/10.1029/2008JB005870.

NGDC (2016). "Significant Earthquake Database". In: *National Geophysical Data Center*. DOI: 10.7289/V5TD9V7K. URL: https://www.ngdc.noaa.gov/nndc/struts/form?t=101650&s=1&d=1.

Niemi, Nathan A. et al. (2004). "BARGEN continuous GPS data across the eastern Basin and Range province, and implications for fault system dynamics". In: *Geophysical Journal International* 159.3, pp. 842–862. ISSN: 1365-246X. DOI: 10.1111/j.1365-246X.2004.02454.x. URL: http://dx.doi.org/10.1111/j.1365-246X.2004.02454.x.

Ninis, Dee et al. (2013). "Slip Rate on the Wellington Fault, New Zealand, during the Late Quaternary: Evidence for Variable Slip during the Holocene". In: *Bulletin of the Seismological Society of America* 103.1, pp. 559–579. ISSN: 0037-1106. DOI: 10.1785/0120120162. eprint: http://bssa.geoscienceworld.org/content/103/1/559.full.pdf. URL: http://bssa.geoscienceworld.org/content/103/1/559.

Ogata, Yosihiko (1988). "Statistical Models for Earthquake Occurrences and Residual Analysis for Point Processes". In: *Journal of the American Statistical Association* 83.401, pp. 9–27. ISSN: 01621459. URL: http://www.jstor.org/stable/2288914.

Okada, Yoshimitsu (1985). "Surface deformation due to shear and tensile faults in a half-space". In: *Bulletin of the Seismological Society of America* 75.4, pp. 1135–1154. eprint: http://www.bssaonline.org/content/75/4/1135.full.pdf+html. URL: http://www.bssaonline.org/content/75/4/1135.abstract.

Omi, Takahiro et al. (2013). "Forecasting large aftershocks within one day after the main shock". In: *Scientific Reports* 3, 2218 EP –. URL: http://dx.doi.org/10.1038/srep02218.

Oskin, Michael et al. (2007). "Slip rate of the Calico fault: Implications for geologic versus geodetic rate discrepancy in the Eastern California Shear Zone". In: *Journal of Geophysical Research: Solid Earth* 112.B3. B03402. ISSN: 2156-2202. DOI: 10.1029/2006JB004451. URL: http://dx.doi.org/10.1029/2006JB004451.

Oskin, Michael et al. (2008). "Elevated shear zone loading rate during an earthquake cluster in eastern California". In: *Geology* 36.6, pp. 507–510. DOI: 10.1130/G24814A.1. eprint: http://geology.gsapubs.org/content/36/6/507.full.pdf+html. URL: http://geology.gsapubs.org/content/36/6/507.abstract.

Page, Morgan and Karen Felzer (2015). "Southern San Andreas Fault Seismicity is Consistent with the Gutenberg-Richter Magnitude-Frequency Distribution". In: *Bulletin of the Seismological Society of America* 105.4, pp. 2070–2080. DOI: 10.1785/0120140340. eprint: http://www.bssaonline.org/content/

105/4/2070.full.pdf+html. URL: http://www.bssaonline.org/content/105/4/2070.abstract.

Pandey, M. R. et al. (1995). "Interseismic strain accumulation on the Himalayan crustal ramp (Nepal)". In: *Geophysical Research Letters* 22.7, pp. 751–754. ISSN: 1944-8007. DOI: 10.1029/94GL02971. URL: http://dx.doi.org/10.1029/94GL02971.

Pandey, M.R et al. (1999). "Seismotectonics of the Nepal Himalaya from a local seismic network". In: *Journal of Asian Earth Sciences* 17.56, pp. 703 –712. ISSN: 1367-9120. DOI: http://dx.doi.org/10.1016/S1367-9120(99)00034-6. URL: http://www.sciencedirect.com/science/article/pii/S1367912099000346.

Pant, M. R. (2002). "A step toward a historical seismicity of Nepal". In: *Adarsa* 2, pp. 29–60.

Parkash, B. et al. (2011). "Convergence rates along the Himalayan Frontal Thrust inferred from terraces at Chandidevi Temple Hill, Hardwar, Northwestern Himalaya". In: *Curr Sci* 100, pp. 1426 –1432.

Parsons, Tom (2002). "Global Omori law decay of triggered earthquakes: Large aftershocks outside the classical aftershock zone". In: *Journal of Geophysical Research: Solid Earth* 107.B9, ESE 9–1–ESE 9–20. ISSN: 2156-2202. DOI: 10.1029/2001JB000646. URL: http://dx.doi.org/10.1029/2001JB000646.

– (2006). "Tectonic stressing in California modeled from GPS observations". In: *Journal of Geophysical Research: Solid Earth* 111.B3. B03407. ISSN: 2156-2202. DOI: 10.1029/2005JB003946. URL: http://dx.doi.org/10.1029/2005JB003946.

– (2008). "Monte Carlo method for determining earthquake recurrence parameters from short paleoseismic catalogs: Example calculations for California". In: *Journal of Geophysical Research: Solid Earth* 113.B3. B03302. ISSN: 2156-2202. DOI: 10.1029/2007JB004998. URL: http://dx.doi.org/10.1029/2007JB004998.

Parsons, Tom and Eric L. Geist (2009). "Is There a Basis for Preferring Characteristic Earthquakes over a GutenbergRichter Distribution in Probabilistic Earthquake Forecasting?" In: *Bulletin of the Seismological Society of America* 99.3, pp. 2012–2019. DOI: 10.1785/0120080069. eprint: http://www.bssaonline.org/content/99/3/2012.full.pdf+html. URL: http://www.bssaonline.org/content/99/3/2012.abstract.

Parsons, Tom et al. (2012). "Comparison of characteristic and Gutenberg-Richter models for time-dependent M 7.9 earthquake probability in the Nankai-Tokai subduction zone, Japan". In: *Geophysical Journal International* 190.3, pp. 1673–1688. ISSN: 1365-246X. DOI: 10.1111/j.1365-246X.2012.05595.x. URL: http://dx.doi.org/10.1111/j.1365-246X.2012.05595.x.

Peltzer, Gilles et al. (2001). "Transient strain accumulation and fault interaction in the Eastern California shear zone". In: *Geology* 29.11, pp. 975–978. eprint: http://geology.gsapubs.org/content/29/11/975.full.pdf+html. URL: http://geology.gsapubs.org/content/29/11/975.abstract.

Pérez, Omar J., Carlos Sanz, and Gabriela Lagos (1997). "Microseismicity, tectonics and seismic potential in southern Caribbean and northern Venezuela". In: *Journal of Seismology* 1.1, pp. 15–28. ISSN: 1573-157X. DOI: 10.1023/A:1009710122083. URL: http://dx.doi.org/10.1023/A:1009710122083.

Perfettini, H. and J.-P. Avouac (2004). "Postseismic relaxation driven by brittle creep: A possible mechanism to reconcile geodetic measurements and the decay rate of aftershocks, application to the Chi-Chi earthquake, Taiwan". In: *Journal of Geophysical Research: Solid Earth* 109.B2. ISSN: 2156-2202. DOI: 10.1029/2003JB002488. URL: http://dx.doi.org/10.1029/2003JB002488.

Perfettini, Hugo et al. (2010). "Seismic and aseismic slip on the Central Peru megathrust". In: *Nature* 465.7294, pp. 78–81. URL: http://dx.doi.org/10.1038/nature09062.

Pisarenko, V. F., D. Sornette, and M. V. Rodkin (2010). "Distribution of maximum earthquake magnitudes in future time intervals: application to the seismicity of Japan (1923–2007)". In: *Earth, Planets and Space* 62.7, pp. 567–578. ISSN: 1880-5981. DOI: 10.5047/eps.2010.06.003. URL: http://dx.doi.org/10.5047/eps.2010.06.003.

Pisarenko, V. F. et al. (2008). "New Approach to the Characterization of M max and of the Tail of the Distribution of Earthquake Magnitudes". In: *Pure and Applied Geophysics* 165.5, pp. 847–888. ISSN: 1420-9136. DOI: 10.1007/s00024-008-0341-9. URL: http://dx.doi.org/10.1007/s00024-008-0341-9.

Ponraj, M. et al. (2011). "Slip distribution beneath the Central and Western Himalaya inferred from GPS observations". In: *Geophysical Journal International* 185.2, pp. 724–736. ISSN: 1365-246X. DOI: 10.1111/j.1365-246X.2011.04958.x. URL: http://dx.doi.org/10.1111/j.1365-246X.2011.04958.x.

Radiguet, M. et al. (2012). "Slow slip events and strain accumulation in the Guerrero gap, Mexico". In: *Journal of Geophysical Research: Solid Earth* 117.B4. B04305. ISSN: 2156-2202. DOI: 10.1029/2011JB008801. URL: http://dx.doi.org/10.1029/2011JB008801.

Rajaure, S. et al. (2013). "Double difference relocation of local earthquakes in the Nepal Himalaya". In: *Journal of Nepal Geological Society*, pp. 133–142.

Rajendran, CP et al. (2013). "Archeological and historical database on the medieval earthquakes of the central Himalaya: Ambiguities and inferences". In: *Seismological Research Letters* 84.6, pp. 1098–1108.

Reasenberg, Paul (1985). "Second-order moment of central California seismicity, 19691982". In: *Journal of Geophysical Research: Solid Earth* 90.B7, pp. 5479–5495. ISSN: 2156-2202. DOI: 10.1029/JB090iB07p05479. URL: http://dx.doi.org/10.1029/JB090iB07p05479.

Reasenberg, Paul A., Thomas C. Hanks, and William H. Bakun (2003). "An Empirical Model for Earthquake Probabilities in the San Francisco Bay Region, California, 2002-2031". In: *Bulletin of the Seismological Society of America* 93.1, pp. 1–13. DOI: 10.1785/0120020014. eprint: http://www.bssaonline.org/content/93/1/1.full.pdf+html. URL: http://www.bssaonline.org/content/93/1/1.abstract.

Reasenberg, Paul A. and Lucile M. Jones (1989). "Earthquake Hazard After a Mainshock in California". In: *Science* 243.4895, pp. 1173–1176. ISSN: 0036-8075. DOI: 10.1126/science.243.4895.1173. eprint: http://science.sciencemag.org/content/243/4895/1173.full.pdf. URL: http://science.sciencemag.org/content/243/4895/1173.

Reilinger, Robert et al. (2006). "GPS constraints on continental deformation in the Africa-Arabia-Eurasia continental collision zone and implications for the dynamics of plate interactions". In: *Journal of Geophysical Research: Solid Earth* 111.B5. B05411. ISSN: 2156-2202. DOI: 10.1029/2005JB004051. URL: http://dx.doi.org/10.1029/2005JB004051.

Riguzzi, Federica et al. (2012). "Geodetic strain rate and earthquake size: New clues for seismic hazard studies". In: *Physics of the Earth and Planetary Interiors* 206-207, pp. 67 –75. ISSN: 0031-9201. DOI: http://dx.doi.org/10.1016/j.pepi.2012.07.005. URL: http://www.sciencedirect.com/science/article/pii/S0031920112001264.

Rong, Yufang et al. (2014). "Magnitude Limits of Subduction Zone Earthquakes". In: *Bulletin of the Seismological Society of America* 104.5, pp. 2359–2377. DOI: 10.1785/0120130287. eprint: http://www.bssaonline.org/content/104/5/2359.full.pdf+html. URL: http://www.bssaonline.org/content/104/5/2359.abstract.

Salamon, Amos et al. (2003). "Seismotectonics of the Sinai subplate - the eastern Mediterranean region". In: *Geophysical Journal International* 155.1, pp. 149–173. DOI: 10.1046/j.1365-246X.2003.02017.x. eprint: http://gji.oxfordjournals.org/content/155/1/149.full.pdf+html. URL: http://gji.oxfordjournals.org/content/155/1/149.abstract.

Sapkota, S N et al. (2013). "Primary surface ruptures of the great Himalayan earthquakes in 1934 and 1255". In: *Nature Geoscience* 6, pp. 71–76. ISSN: 1752-0894. URL: http://dx.doi.org/10.1038/ngeo1720.

Satake, Kenji (2015). "Geological and historical evidence of irregular recurrent earthquakes in Japan". In: *Philosophical Transactions of the Royal Society of London A: Mathematical, Physical and Engineering Sciences* 373.2053. ISSN:

1364-503X. DOI: 10.1098/rsta.2014.0375. eprint: http://rsta.royalsocietypublishing.org/content/373/2053/20140375.full.pdf. URL: http://rsta.royalsocietypublishing.org/content/373/2053/20140375.

Savage, J. C. (1983). "A Dislocation Model of Strain Accumulation and Release at a Subduction Zone". In: *J. Geophys. Res.* 88.B6, pp. 4984–4996. ISSN: 0148-0227. URL: http://dx.doi.org/10.1029/JB088iB06p04984.

Scharer, Katherine M. et al. (2010). "Quasi-periodic recurrence of large earthquakes on the southern San Andreas fault". In: *Geology* 38.6, pp. 555–558. DOI: 10.1130/G30746.1. eprint: http://geology.gsapubs.org/content/38/6/555.full.pdf+html. URL: http://geology.gsapubs.org/content/38/6/555.abstract.

Schiffman, Celia et al. (2013). "Seismic slip deficit in the Kashmir Himalaya from GPS observations". In: *Geophysical Research Letters*. ISSN: 1944-8007. DOI: 10.1002/2013GL057700. URL: http://dx.doi.org/10.1002/2013GL057700.

Schmalzle, Gina M., Robert McCaffrey, and Kenneth C. Creager (2014). "Central Cascadia subduction zone creep". In: *Geochemistry, Geophysics, Geosystems* 15.4, pp. 1515–1532. ISSN: 1525-2027. DOI: 10.1002/2013GC005172. URL: http://dx.doi.org/10.1002/2013GC005172.

Schubert, Carlos (1982). "Neotectonics of Boconó fault, Western Venezuela". In: *Tectonophysics* 85.3, pp. 205 –220. ISSN: 0040-1951. DOI: http://dx.doi.org/10.1016/0040-1951(82)90103-2. URL: http://www.sciencedirect.com/science/article/pii/0040195182901032.

Schubert, Carlos and Ramón S. Sifontes (1970). "Boconó Fault, Venezuelan Andes: Evidence of Postglacial Movement". In: *Science* 170.3953, pp. 66–69. ISSN: 0036-8075. DOI: 10.1126/science.170.3953.66. eprint: http://science.sciencemag.org/content/170/3953/66.full.pdf. URL: http://science.sciencemag.org/content/170/3953/66.

Schwanghart, Wolfgang et al. (2016). "Repeated catastrophic valley infill following medieval earthquakes in the Nepal Himalaya". In: *Science* 351.6269, pp. 147–150. ISSN: 0036-8075. DOI: 10.1126/science.aac9865. eprint: http://science.sciencemag.org/content/351/6269/147.full.pdf. URL: http://science.sciencemag.org/content/351/6269/147.

Schwartz, D.P. and K.J. Coppersmith (1984). "Fault behavior and characteristic earthquakes: examples from the Wasatch and San Andreas fault zones". In: *Journal of Geophysical Research* 89, pp. 5681–5698.

Scordilis, E.M. (2006). "Empirical Global Relations Converting M S and m b to Moment Magnitude". English. In: *Journal of Seismology* 10.2, pp. 225–236. ISSN: 1383-4649. DOI: 10.1007/s10950-006-9012-4. URL: http://dx.doi.org/10.1007/s10950-006-9012-4.

Şengör, A.M.C. et al. (2005). "THE NORTH ANATOLIAN FAULT: A NEW LOOK". In: *Annual Review of Earth and Planetary Sciences* 33.1, pp. 37–112. DOI: 10.1146/annurev.earth.32.101802.120415. eprint: http://dx.doi.org/10.1146/annurev.earth.32.101802.120415. URL: http://dx.doi.org/10.1146/annurev.earth.32.101802.120415.

Shearer, Peter M. and Philip B. Stark (2012). "Global risk of big earthquakes has not recently increased". In: *Proceedings of the National Academy of Sciences* 109.3, pp. 717–721. DOI: 10.1073/pnas.1118525109. eprint: http://www.pnas.org/content/109/3/717.full.pdf. URL: http://www.pnas.org/content/109/3/717.abstract.

Shen, Zheng-Kang, David D. Jackson, and Yan Y. Kagan (2007). "Implications of Geodetic Strain Rate for Future Earthquakes, with a Five-Year Forecast of M5 Earthquakes in Southern California". In: *Seismological Research Letters* 78.1, pp. 116–120. DOI: 10.1785/gssrl.78.1.116. eprint: http://srl.geoscienceworld.org/content/78/1/116.full.pdf+html. URL: http://srl.geoscienceworld.org/content/78/1/116.short.

Shinohara, Masanao et al. (2013). "Precise aftershock distribution of the 2011 off the Pacific coast of Tohoku Earthquake revealed by an ocean-bottom seismometer network". In: *Earth, Planets and Space* 64.12, pp. 1137–1148. ISSN: 1880-5981. DOI: 10.5047/eps.2012.09.003. URL: http://dx.doi.org/10.5047/eps.2012.09.003.

Sieh, Kerry et al. (2008). "Earthquake Supercycles Inferred from Sea-Level Changes Recorded in the Corals of West Sumatra". In: *Science* 322.5908, pp. 1674–1678. DOI: 10.1126/science.1163589. eprint: http://www.sciencemag.org/content/322/5908/1674.full.pdf. URL: http://www.sciencemag.org/content/322/5908/1674.abstract.

Smith-Konter, Bridget R., David T. Sandwell, and Peter Shearer (2011). "Locking depths estimated from geodesy and seismology along the San Andreas Fault System: Implications for seismic moment release". In: *Journal of Geophysical Research: Solid Earth* 116.B6. B06401. ISSN: 2156-2202. DOI: 10.1029/2010JB008117. URL: http://dx.doi.org/10.1029/2010JB008117.

Socquet, Anne et al. (2006). "Microblock rotations and fault coupling in SE Asia triple junction (Sulawesi, Indonesia) from GPS and earthquake slip vector data". In: *Journal of Geophysical Research: Solid Earth* 111.B8. ISSN: 2156-2202. DOI: 10.1029/2005JB003963. URL: http://dx.doi.org/10.1029/2005JB003963.

Sokolov, V. Y., Loh CH., and KL. Wen (2001). "Empirical Models for Site- and Region-Dependent Ground-Motion Parameters in the Taipei Area: A Unified Approach". In: *Earthquake Spectra* 17.2, pp. 313–331. DOI: 10.1193/1.1586177. eprint: http://dx.doi.org/10.1193/1.1586177. URL: http://dx.doi.org/10.1193/1.1586177.

Stein, Ross S., Aykut A. Barka, and James H. Dieterich (1997). "Progressive failure on the North Anatolian fault since 1939 by earthquake stress triggering". In: *Geophysical Journal International* 128.3, pp. 594–604. ISSN: 1365-246X. DOI: 10.1111/j.1365-246X.1997.tb05321.x. URL: http://dx.doi.org/10.1111/j.1365-246X.1997.tb05321.x.

Stevens, V. L. and J. P. Avouac (2015). "Interseismic coupling on the main Himalayan thrust". In: *Geophysical Research Letters* 42.14. 2015GL064845, pp. 5828–5837. ISSN: 1944-8007. DOI: 10.1002/2015GL064845. URL: http://dx.doi.org/10.1002/2015GL064845.

– (2016). "Millenary Mw>9.0 earthquakes required by geodetic strain in the Himalaya". In: *Geophysical Research Letters* 43.3. 2015GL067336, pp. 1118–1123. ISSN: 1944-8007. DOI: 10.1002/2015GL067336. URL: http://dx.doi.org/10.1002/2015GL067336.

Stirling, Mark W., Steven G. Wesnousky, and Kunihiko Shimazaki (1996). "Fault trace complexity, cumulative slip, and the shape of the magnitude-frequency distribution for strike-slip faults: a global survey". In: *Geophysical Journal International* 124.3, pp. 833–868. ISSN: 1365-246X. DOI: 10.1111/j.1365-246X.1996.tb05641.x. URL: http://dx.doi.org/10.1111/j.1365-246X.1996.tb05641.x.

Stover, C. W. and J. L. Coffman (1993). *Seismicity of the United States, 1568-1989 (revised)*. Tech. rep. URL: http://pubs.er.usgs.gov/publication/pp1527.

Styron, Richard, Michael Taylor, and Kelechi Okoronkwo (2010). "Database of Active Structures From the Indo-Asian Collision". In: *Eos, Transactions American Geophysical Union* 91.20, pp. 181–182. ISSN: 2324-9250. DOI: 10.1029/2010EO200001. URL: http://dx.doi.org/10.1029/2010EO200001.

Szeliga, Walter et al. (2012). "Interseismic strain accumulation along the western boundary of the Indian subcontinent". In: *Journal of Geophysical Research: Solid Earth* 117.B8. ISSN: 2156-2202. DOI: 10.1029/2011JB008822. URL: http://dx.doi.org/10.1029/2011JB008822.

Tahir, Mohammad and Jean Robert Grasso (2014). "Aftershock Patterns of Ms≥7 Earthquakes in the IndiaAsia Collision Belt: Anomalous Results from the Muzaffarabad Earthquake Sequence, Kashmir, 2005". In: *Bulletin of the Seismological Society of America* 104.1, pp. 1–23. DOI: 10.1785/0120120158. eprint: http://www.bssaonline.org/content/104/1/1.full.pdf+html. URL: http://www.bssaonline.org/content/104/1/1.abstract.

Tape, Carl et al. (2009). "Multiscale estimation of GPS velocity fields". In: *Geophysical Journal International* 179.2, pp. 945–971. ISSN: 1365-246X. DOI: 10.1111/j.1365-246X.2009.04337.x. URL: http://dx.doi.org/10.1111/j.1365-246X.2009.04337.x.

Thakur, V.C. et al. (2014). "Partitioning of convergence in Northwest Sub-Himalaya: estimation of late Quaternary uplift and convergence rates across the Kangra reentrant, North India". English. In: *International Journal of Earth Sciences* 103.4, pp. 1037–1056. ISSN: 1437-3254. DOI: 10.1007/s00531-014-1016-7. URL: http://dx.doi.org/10.1007/s00531-014-1016-7.

Toda, Shinji and Ross S. Stein (2013). "The 2011 M=9.0 Tohoku Oki earthquake more than doubled the probability of large shocks beneath Tokyo". In: *Geophysical Research Letters* 40.11, pp. 2562–2566. ISSN: 1944-8007. DOI: 10.1002/grl.50524. URL: http://dx.doi.org/10.1002/grl.50524.

Tormann, Thessa, Stefan Wiemer, and Egill Hauksson (2010). "Changes of Reporting Rates in the Southern California Earthquake Catalog, Introduced by a New Definition of ML". In: *Bulletin of the Seismological Society of America* 100.4, pp. 1733–1742. DOI: 10.1785/0120090124. eprint: http://www.bssaonline.org/content/100/4/1733.full.pdf+html. URL: http://www.bssaonline.org/content/100/4/1733.abstract.

Uchida, Naoki and Toru Matsuzawa (2011). "Coupling coefficient, hierarchical structure, and earthquake cycle for the source area of the 2011 off the Pacific coast of Tohoku earthquake inferred from small repeating earthquake data". In: *Earth, Planets and Space* 63.7, pp. 675–679. ISSN: 1880-5981. DOI: 10.5047/eps.2011.07.006. URL: http://dx.doi.org/10.5047/eps.2011.07.006.

Upreti, BN et al. (2000). "The latest active faulting in southeast Nepal". In: *Proceedings of the Hokudan International Symposium and School on Active Faulting*, pp. 17–26.

Usami, Tatsuo (2002). "48.4 Historical earthquakes in Japan". In: *International Handbook of Earthquake and Engineering Seismology*. Ed. by Paul C. Jennings William H.K. Lee Hiroo Kanamori and Carl Kisslinger. Vol. 81, Part A. International Geophysics. Academic Press, pp. 799 –802. DOI: http://dx.doi.org/10.1016/S0074-6142(02)80254-6. URL: http://www.sciencedirect.com/science/article/pii/S0074614202802546.

Utsu, T. (1965). "A method for determining the value of b in the formula log n = abM showing the magnitude-frequency relation for earthquakes". In: *Geophys. Bull. Hokkaido Univ. 13* 13, pp. 99–103.

Van Der Woerd, Jerome et al. (2002). "Uniform postglacial slip-rate along the central 600 km of the Kunlun Fault (Tibet), from 26Al, 10Be, and 14C dating of riser offsets, and climatic origin of the regional morphology". In: *Geophysical Journal International* 148.3, pp. 356–388. ISSN: 1365-246X. DOI: 10.1046/j.1365-246x.2002.01556.x. URL: http://dx.doi.org/10.1046/j.1365-246x.2002.01556.x.

Vergne, J., R. Cattin, and J. P. Avouac (2001). "On the use of dislocations to model interseismic strain and stress build-up at intracontinental thrust faults". In: *Geophysical Journal International* 147.1, pp. 155–162. ISSN: 1365-246X. DOI: 10.

1046/j.1365-246X.2001.00524.x. URL: http://dx.doi.org/10.1046/j.1365-246X.2001.00524.x.

Vernant, P. et al. (2014). "Clockwise rotation of the Brahmaputra Valley relative to India: Tectonic convergence in the eastern Himalaya, Naga Hills, and Shillong Plateau". In: *Journal of Geophysical Research: Solid Earth* 119.8, pp. 6558–6571. ISSN: 2169-9356. DOI: 10.1002/2014JB011196. URL: http://dx.doi.org/10.1002/2014JB011196.

Vidale, John E. and Peter M. Shearer (2006). "A survey of 71 earthquake bursts across southern California: Exploring the role of pore fluid pressure fluctuations and aseismic slip as drivers". In: *Journal of Geophysical Research: Solid Earth* 111.B5. B05312. ISSN: 2156-2202. DOI: 10.1029/2005JB004034. URL: http://dx.doi.org/10.1029/2005JB004034.

Wallace, Laura M. and John Beavan (2006). "A large slow slip event on the central Hikurangi subduction interface beneath the Manawatu region, North Island, New Zealand". In: *Geophysical Research Letters* 33.11. L11301, n/a–n/a. ISSN: 1944-8007. DOI: 10.1029/2006GL026009. URL: http://dx.doi.org/10.1029/2006GL026009.

Wang, Kelin, Yan Hu, and Jiangheng He (2012). "Deformation cycles of subduction earthquakes in a viscoelastic Earth". In: *Nature* 484.7394, pp. 327–332. URL: http://dx.doi.org/10.1038/nature11032.

Wang, Qi, David D. Jackson, and Yan Y. Kagan (2009). "California Earthquakes, 18002007: A Unified Catalog with Moment Magnitudes, Uncertainties, and Focal Mechanisms". In: *Seismological Research Letters* 80.3, pp. 446–457. DOI: 10.1785/gssrl.80.3.446. eprint: http://srl.geoscienceworld.org/content/80/3/446.full.pdf+html. URL: http://srl.geoscienceworld.org/content/80/3/446.short.

Wang, Yanzhao et al. (2014). "Coulomb Stress Change and Evolution Induced by the 2008 Wenchuan Earthquake and its Delayed Triggering of the 2013 Mw 6.6 Lushan Earthquake". In: *Seismological Research Letters* 85.1, pp. 52–59. DOI: 10.1785/0220130111. eprint: http://srl.geoscienceworld.org/content/85/1/52.full.pdf+html. URL: http://srl.geoscienceworld.org/content/85/1/52.short.

Wang, Yu et al. (2011). "Earthquakes and slip rate of the southern Sagaing fault: insights from an offset ancient fort wall, lower Burma (Myanmar)". In: *Geophysical Journal International* 185.1, pp. 49–64. ISSN: 1365-246X. DOI: 10.1111/j.1365-246X.2010.04918.x. URL: http://dx.doi.org/10.1111/j.1365-246X.2010.04918.x.

Washburn, Z. et al. (2003). "Paleoseismology of the Xorxol Segment of the Central Altyn Tagh Fault, Xinjiang, China". In: *Annals of Geophysics* 46.5. ISSN: 2037-416X. URL: http://www.annalsofgeophysics.eu/index.php/annals/article/view/3443.

Wdowinski, S. et al. (2004). “GPS measurements of current crustal movements along the Dead Sea Fault”. In: *Journal of Geophysical Research: Solid Earth* 109.B5. B05403. ISSN: 2156-2202. DOI: 10.1029/2003JB002640. URL: http://dx.doi.org/10.1029/2003JB002640.

Weldon, R. et al. (2004). “Wrightwood and the earthquake cycle: What a long recurrence record tells us about how faults work”. In: *GSA today* 14.9, pp. 4–10. URL: http://pubs.er.usgs.gov/publication/70026626.

Weldon, Ray J. and Kerry E. Sieh (1985). “Holocene rate of slip and tentative recurrence interval for large earthquakes on the San Andreas fault, Cajon Pass, southern California”. In: *Geological Society of America Bulletin* 96.6, pp. 793–812. eprint: http://gsabulletin.gsapubs.org/content/96/6/793.full.pdf+html. URL: http://gsabulletin.gsapubs.org/content/96/6/793.abstract.

Wells, Donald L. and Kevin J. Coppersmith (1994). “New empirical relationships among magnitude, rupture length, rupture width, rupture area, and surface displacement”. In: *Bulletin of the Seismological Society of America* 84.4, 974–1002,A1–A4,B1–B11,C1–C49. eprint: http://www.bssaonline.org/content/84/4/974.full.pdf+html. URL: http://www.bssaonline.org/content/84/4/974.abstract.

Wesnousky, Steven G. (1994). “The Gutenberg-Richter or characteristic earthquake distribution, which is it?” In: *Bulletin of the Seismological Society of America* 84.6, pp. 1940–1959. eprint: http://www.bssaonline.org/content/84/6/1940.full.pdf+html. URL: http://www.bssaonline.org/content/84/6/1940.abstract.

– (2008). “Displacement and Geometrical Characteristics of Earthquake Surface Ruptures: Issues and Implications for Seismic-Hazard Analysis and the Process of Earthquake Rupture”. In: *Bulletin of the Seismological Society of America* 98.4, pp. 1609–1632. DOI: 10.1785/0120070111. eprint: http://www.bssaonline.org/content/98/4/1609.full.pdf+html. URL: http://www.bssaonline.org/content/98/4/1609.abstract.

Wesnousky, Steven G. et al. (1999). “Uplift and convergence along the Himalayan Frontal Thrust of India”. In: *Tectonics* 18.6, pp. 967–976. ISSN: 1944-9194. DOI: 10.1029/1999TC900026. URL: http://dx.doi.org/10.1029/1999TC900026.

Wiemer, Stefan (2001). “A Software Package to Analyze Seismicity: ZMAP”. In: *Seismological Reseach Letters* 72.3, pp. 373–382. DOI: 10,1785/gssrl.72.3.373.

Wiemer, Stefan and Max Wyss (2002). “Mapping spatial variability of the frequency-magnitude distribution of earthquakes”. In: *Advances in geophysics* 45, pp. 259–302.

Wright, Tim J. et al. (2004). "InSAR Observations of Low Slip Rates on the Major Faults of Western Tibet". In: *Science* 305.5681, pp. 236–239. DOI: 10.1126/science.1096388. eprint: http://www.sciencemag.org/content/305/5681/236.full.pdf. URL: http://www.sciencemag.org/content/305/5681/236.abstract.

Yamagiwa, Shuji et al. (2015). "Afterslip and viscoelastic relaxation following the 2011 Tohoku-oki earthquake (Mw9.0) inferred from inland GPS and seafloor GPS/Acoustic data". In: *Geophysical Research Letters* 42.1. 2014GL061735, pp. 66–73. ISSN: 1944-8007. DOI: 10.1002/2014GL061735. URL: http://dx.doi.org/10.1002/2014GL061735.

Yang, ShaoMin, Jie Li, and Qi Wang (2008). "The deformation pattern and fault rate in the Tianshan Mountains inferred from GPS observations". English. In: *Science in China Series D: Earth Sciences* 51.8, pp. 1064–1080. ISSN: 1006-9313. DOI: 10.1007/s11430-008-0090-8. URL: http://dx.doi.org/10.1007/s11430-008-0090-8.

Zhan, Zhongwen et al. (2012). "Anomalously steep dips of earthquakes in the 2011 Tohoku-Oki source region and possible explanations". In: *Earth and Planetary Science Letters* 353354, pp. 121 –133. ISSN: 0012-821X. DOI: http://dx.doi.org/10.1016/j.epsl.2012.07.038. URL: http://www.sciencedirect.com/science/article/pii/S0012821X12004207.

Zöller, G., S. Hainzl, and M. Holschneider (2010). "Recurrence of Large Earthquakes: Bayesian Inference from Catalogs in the Presence of Magnitude Uncertainties". In: *Pure and Applied Geophysics* 167.6, pp. 845–853. ISSN: 1420-9136. DOI: 10.1007/s00024-010-0078-0. URL: http://dx.doi.org/10.1007/s00024-010-0078-0.

Zöller, Gert and Matthias Holschneider (2016). "The Earthquake History in a Fault Zone Tells Us Almost Nothing about mmax". In: *Seismological Research Letters* 87.1, pp. 132–137. DOI: 10.1785/0220150176. eprint: http://srl.geoscienceworld.org/content/87/1/132.full.pdf+html. URL: http://srl.geoscienceworld.org/content/87/1/132.abstract.

Zöller, Gert, Matthias Holschneider, and Sebastian Hainzl (2013). "The Maximum Earthquake Magnitude in a Time Horizon: Theory and Case Studies". In: *Bulletin of the Seismological Society of America* 103.2A, pp. 860–875. DOI: 10.1785/0120120013. eprint: http://www.bssaonline.org/content/103/2A/860.full.pdf+html. URL: http://www.bssaonline.org/content/103/2A/860.abstract.

Zöller, Gert et al. (2014). "The Largest Expected Earthquake Magnitudes in Japan: The Statistical Perspective". In: *Bulletin of the Seismological Society of America* 104.2, pp. 769–779. DOI: 10.1785/0120130103. eprint: http://www.bssaonline.org/content/104/2/769.full.pdf+html. URL: http://www.bssaonline.org/content/104/2/769.abstract.

Zubovich, Alexander V. et al. (2010). “GPS velocity field for the Tien Shan and surrounding regions”. In: *Tectonics* 29.6. ISSN: 1944-9194. DOI: 10.1029/2010TC002772. URL: http://dx.doi.org/10.1029/2010TC002772.